# GAS INJECTION FOR ENHANCED OIL RECOVERY IN ORGANIC RICH SHALE RESERVOIRS

A Dissertation

by

FRANCISCO DEOMAR TOVAR

Submitted to the Office of Graduate and Professional Studies of
Texas A&M University
in partial fulfillment of the requirements for the degree of

DOCTOR OF PHILOSOPHY

| | |
|---|---|
| Chair of Committee, | David S. Schechter |
| Co-chair of Committee, | Maria A. Barrufet |
| Committee Members, | I. Yucel Akkutlu |
| | Hadi Nasrabadi |
| Head of Department, | A. Daniel Hill |

December 2017

Major Subject: Petroleum Engineering

ABSTRACT

Oil production from organic rich shale has grown significantly in the last decade due to the combination of hydraulic fracturing and horizontal drilling. Yet, this primary recovery exploitation scheme exhibits fast production rate decline and low ultimate recovery. Gas injection, mainly $CO_2$ injection, has been successfully applied for EOR in conventional reservoirs, making it attractive for implementation in shales. However, organic rich shale exhibits poor fluid transport, and contains kerogen rich in micropores and mesopores. This causes fundamental differences in the storage, transport and phase behavior mechanisms. This work investigates how these differences affect the implementation of gas injection in shale reservoirs, and the benefits we can obtain from it, in terms of oil recovery.

Laboratory equipment simulating gas injection through a hydraulic fracture was designed, and coupled to a CT-scanner to track compositional changes with time. We performed 23 core-flooding experiments using shale sidewall cores that were either used as received, or re-saturated in the laboratory; and Berea sandstone. Continuous injection and huff-and-puff were compared at different pressures. The injection gases were $CO_2$ or nitrogen. We provide a comprehensive procedure for sample preparation involving the measurement of fluid and rock properties.

$CO_2$ injection in organic rich shale resulted in a maximum recovery factor of 40%. Most of the oil production occurred in the first 24 hours. The main production mechanism is a peripheral slow-kinetics vaporizing gas drive. Oil is not displaced, instead, it is vaporized by the gas contained in the fracture, and transported outside the reservoir where it is condensed. Vaporization occurs from the periphery of the matrix, where the injection gas is stored. Mass transfer is slow due to the poor transport through the shale matrix. Therefore, recovery depends on the fraction of hydrocarbon components the injection gas can vaporize at the prevailing conditions of pressure and temperature, the concentration of those hydrocarbons in the reservoir oil, and the time allowed for mass transfer. $CO_2$ was better than $N_2$. Increasing pressure beyond MMP continued to

increase recovery, and at a constant pressure, a huff-and-puff injection scheme was more effective than continuous gas injection.

# DEDICATION

To my parents, specially mom, who always disagrees with me, yet supports me.

To my sisters, specially Francys, who hates I am away, yet encourages me to go after my goals.

To my brother in law, Luis, who makes the “in law” feels so out of place.

To my nephews, who do not see me so often, yet they love me.

ACKNOWLEDGEMENTS

I would like to start by thanking two extraordinary persons; the chair and the co-chair of my committee. After six and a half years of working with them towards my Master of Science and Doctor of Philosophy degrees, the line between friendship and mentorship is quite blurry. Their guidance, support, patience, and confidence in me, made me a happy graduate student. Dr. Schechter somehow managed to believe more in my ideas than myself; he was without a doubt the one providing me with optimism and confidence. Dr. Barrufet always had a subtle way of pushing me without me noticing it. When she thought something needed improvement, she did not demand me to do so, she convinced me.

I would like to recognize the support of my committee members, Dr. Akkutlu and Dr. Nasralbadi, for the time they put into this project, and their guidance. They greatly contributed to this work by welcoming my inquiries, and sharing their knowledge, experience, and opinions with me.

I would also like to thank Mr. John Maldonado, our facilities coordinator. There is an abysmal difference between those that are just doing their job, and those that truly enjoy helping others. John always went above and beyond to help, and he is one of the most useful and resourceful people I have had the fortune to work with.

Special thanks to my friends, partners in crime, and fellow graduate students, Johannes Alvarez and Imad Adel. Spending countless hours in the laboratory was much more manageable when there were friendly faces smiling at you. They were, and still are, an important part of my support system. I would also like to thank the staff of the department, specially Betty Robbins, Stuart White, Eleanor Schuler, and John Winkler for making my life much easier.

The small but consistent contributions of the student workers that were involved at different stages, and in varying degrees in my research, provided a significant impact. I would like to thank Jared Clark, Nicole

Bhatnagar, Connor Thomas, Rodolfo Marquez, James Skinner, Travis Straub, Hieu Nguyen, Zunyan Yang, Brennan Gaber, and Jessica Schechter for everything they did.

Finally, I would like to recognize my undergraduate academic advisor, Gonzalo Rojas, my former supervisors Carlos Alvarez, Mery Dezio and Cruz Ruiz, and my co-worker Emil Valero, because they mentored me early in my career and helped me place the foundations over which I have built my more recent accomplishments.

# CONTRIBUTORS AND FUNDING SOURCES

## CONTRIBUTORS

### Faculty committee recognition

This work was supervised by a dissertation committee consisting of Associate Professor David Schechter [advisor, home department], Professor Maria Barrufet [co-advisor, home department, outside department], Associate Professor I. Yucel Akkutlu [home department] and Assistant Professor Hadi Nasrabadi [home department].

### Student and collaborators contributions

The development of an early version of the physical representation of a hydraulic fracture in the laboratory, and the first core-flooding performed with it, presented in Chapter III, was done in collaboration with Øyvind Eide from the University of Bergen, and was published in 2014.

The rest of the work in this dissertation was completed independently by the student.

## FUNDING SOURCES

This work was mainly funded by the Crisman Institute for Petroleum Research at Texas A&M University.

Partial funding was also obtained from a fellowship granted by ConocoPhillips through the Texas A&M Energy Institute at Texas A&M University.

A significant part of this investigation was performed in the Chaparral – Fischer $CO_2$ EOR Laboratory established by Chaparral Energy at the Harold Vance Department of Petroleum Engineering at Texas A&M University.

All the CT-scanning work was performed at the Chevron Petrophysical Imaging Laboratory established by Chevron at the Harold Vance Department of Petroleum Engineering at Texas A&M University.

The samples of organic rich shale used in this investigation were donated by Pioneer Natural Resources.

The gas chromatography analysis was kindly donated by GeoMark Research.

NOMENCLATURE

| | |
|---|---|
| A | First coefficient for the compressibility and grain volume calculation, psia |
| API | American Petroleum Institute |
| B | Second coefficient for the compressibility and grain volume calculation, psia |
| BET | Brunnauer – Emmet – Teller |
| BIB | Broad argon ion milling |
| BJH | Barrett – Joyner – Halenda |
| Bulk res vol $_{field}$ | Bulk reservoir volume in the field, $ft^3$ |
| Bulk res vol $_{lab}$ | Bulk reservoir volume in the laboratory, $cm^3$ |
| c | Constant compressibility coefficient, 1/psi |
| C | Third coefficient for the compressibility and grain volume calculation, $psia^2$ |
| c* | Coefficient of constant compressibility only valid between $p_{si}$ and $p_f$ of a particular experimental stage, 1/psi |
| $CO_2$ stored | Total $CO_2$ stored in the rock, Mscf |
| $CO_2$ vol $_{lab}$ | Volume of $CO_2$ injected in the laboratory, $cm^3$ |
| $CO_2$vol.$_{field}$ | Volume of $CO_2$ injected in the field, $ft^3$ |
| Core PV | Pore volume of the laboratory core sample, $cm^3$ |
| CT-scan | Computerized tomography scan, also known as CAT- scan |
| D – R | Dubinin – Radushkevich |
| D | Fourth coefficient for the determination of α and β, $psia_2$ |
| DFT | Density functional theory |
| Dissolved $CO_2$ | Volume of $CO_2$ stored dissolved in the crude oil at standard conditions, $cm^3$ |
| E | Fifth coefficient for the determination of β, psia |
| EDS | Energy dispersive spectroscopy |
| EIA | United States Energy Information Administration |

| | |
|---|---|
| EOR | Enhanced oil recovery |
| EOS | Equation of state |
| FE – SEM | Field emission – scanning electron microscopy |
| FIB | Focused ion milling |
| Frac vol $_{field}$ | Pore volume of the fracture in the field, $ft^3$ |
| Fracture $PV_{field}$ | Pore volume of the field fracture, $cm^3$ |
| Fracture $PV_{lab}$ | Pore volume of the laboratory fracture, $cm^3$ |
| Fracture surface $A_{field}$ | Surface area of the reservoir fracture, $cm^2$ |
| Fracture surface $A_{lab}$ | Surface area of the laboratory fracture in contact with the rock matrix, $cm^2$ |
| Free $CO_2$ | Volume of $CO_2$ stored in a free state within the rock matrix at standard conditions, $cm^3$ |
| $FVF_{oil}$ | Oil formation volume factor, dimensionless |
| GRI | Gas research institute |
| $G_S$ | Volume of sorbed gas per volume of rock, scf/ton |
| $G_{SL}$ | Langmuir volume, $cm^3/gr$ (32.037 $g/cm^3$ = 1 US $ton/ft^3$) |
| $IOIP_{core}$ | Volume of oil initially present in the core, $cm^3$ |
| IUPAC | International Union of Pure and Applied Chemistry |
| M | Molar mass, lb/lb.mol |
| $m_{ads\ max}$ | Mass of the sorbed phase, g |
| MICP | Mercury injection capillary pressure |
| MMP | Minimum miscibility pressure |
| NMR | Nuclear magnetic resonance |
| Np | Cumulative oil production, $cm^3$ |
| $n_{rf}$ | Moles of gas in the reference cell at the final or equilibrium pressure, moles |
| $n_{ri}$ | Moles of gas initially in the reservoir cell, moles |
| $n_{sf}$ | Moles of gas in the sample cell at the final or equilibrium pressure, moles |
| $n_{sf-f}$ | Free gas in the sample cell at the final equilibrium pressure, moles |

| | |
|---|---|
| $n_{sf\text{-}s}$ | Gas sorbed in the sample at the final sample cell pressure, moles |
| $n_{si}$ | Moles of gas initially in the sample cell, moles |
| $n_{si\text{-}f}$ | Free gas in the sample cell at the initial sample cell pressure, moles |
| $n_{si\text{-}s}$ | Gas sorbed in the sample at the initial sample cell pressure, moles |
| $n_{s\text{-}s\ max}$ | Maximum amount of gas that can be sorbed in the sample, moles |
| Number of $cycles_{field}$ | Number of huff and puff cycles performed in the field |
| Number of $cycles_{lab}$ | Number of huff and puff cycles performed in the laboratory |
| OOIP | Original oil in place |
| p | Pressure, psia |
| $p_f$ | Final or equilibrium pressure for both sample and reference cells, psia |
| $p_{f_1}$ | Final or equilibrium pressure for both sample and reference cells, first stage, psia |
| $p_{f_2}$ | Final or equilibrium pressure for both sample and reference cells, second stage, psia |
| $p_L$ | Langmuir pressure, psia |
| por | Rock porosity, fraction |
| $p_{ri}$ | Initial pressure in the reference cell, psia |
| $p_{ri_1}$ | Initial pressure in the reference cell for the first stage, psia |
| $p_{ri_2}$ | Initial pressure in the reference cell for the second stage, psia |
| $p_{si}$ | Initial pressure in the sample cell, psia |
| psig | Pound per square inches – gauge pressure |
| R | Gas constant = 303895.9 $cm^3$.psia/R/lbmol |
| SANS | Small angle neutron scattering |
| SEM | Scanning electron microscopy |
| Soaking $time_{field}$ | Soaking time in the field, hr |
| Soaking $time_{lab}$ | Soaking time in the laboratory, hr |
| Sorbed $CO_2$ | Volume of $CO_2$ sorbed in the rock and the bitumen at standard conditions, $cm^3$ |

| | |
|---|---|
| STB/D | Barrels per day measured at standard conditions |
| STEM | Scanning transmission electron microscopy |
| T | Temperature, R |
| TEM | Transmission electron microscopy |
| TOC | Total organic content |
| ULR | Unconventional liquid reservoirs |
| US | United States of America |
| USANS | ultra – small angle neutron scattering |
| USGS | United States Geological Survey |
| $V_{ads\ f}$ | Volume occupied by the sorbed phase at the final sample cell pressure, $cm^3$ |
| $V_{ads\ i}$ | Volume occupied by the sorbed phase at the initial sample cell pressure, $cm^3$ |
| $V_{ads\ max}$ | Volume occupied by the maximum amount of gas that can be sorbed in the sample, $cm^3$ |
| $V_{ads}$ | Volume occupied by the sorbed phase, $cm^3$ |
| $V_g$ | Grain or skeletal volume assuming rock compressibility is negligible, $cm^3$ |
| $V_{g0}$ | Grain or skeletal volume at room pressure ($p_0$ = 14.7 psia) |
| $V_{gf}$ | Grain or skeletal volume of the rock sample at the final or equilibrium sample cell pressure, $cm^3$ |
| $V_{gi}$ | Grain or skeletal volume of the rock sample at the initial sample cell pressure, psig, $cm^3$ |
| $V_r$ | Reference cell volume, $cm^3$ |
| $V_s$ | Sample cell volume, $cm^3$ |
| $V_{sf\text{-}f}$ | Volume available for free gas storage in the sample cell at the final equilibrium pressure, $cm^3$ |
| $V_{si\text{-}f}$ | Volume available for free gas storage in the sample cell at the initial sample cell pressure, $cm^3$ |
| w | Sample weight, g |
| XRD | X – ray powder diffraction analysis |
| $Z_f$ | Gas compressibility factor at the final or equilibrium pressure, dimensionless |

| | |
|---|---|
| $Z_{f_1}$ | Gas compressibility factor at the final or equilibrium pressure, first stage, dimensionless |
| $Z_{f_2}$ | Gas compressibility factor at the final or equilibrium pressure, second stage, dimensionless |
| $Z_{ri}$ | Gas compressibility factor at the initial reservoir cell pressure, dimensionless |
| $Z_{ri_1}$ | Gas compressibility factor at the initial reservoir cell pressure, first stage, dimensionless |
| $Z_{ri_2}$ | Gas compressibility factor at the initial reservoir cell pressure, second stage, dimensionless |
| $Z_{si}$ | Gas compressibility factor at the initial sample cell pressure, dimensionless |
| $Z_{si_1}$ | Gas compressibility factor at the initial sample cell pressure, first stage, dimensionless |
| $Z_{si_2}$ | Gas compressibility factor at the initial sample cell pressure, second stage, dimensionless |

Greek Letters

| | |
|---|---|
| $\alpha$ | First parameter for the determination of the local constant compressibility c* |
| $\beta$ | Second parameter for the determination of the local constant compressibility c* |
| $\gamma$ | Third parameter for the determination of the local constant compressibility c* |
| $\rho s$ | Density of the sorbed phase, lb /$cm^3$ |
| $\rho_{SC}$ | Density of the sorbed gas at standard conditions, g/$cm^3$ |
| $\rho_{CO_2 res}$ | $CO_2$ density at reservoir conditions, g/$cm^3$ |
| $\rho_{CO_2 std}$ | $CO_2$ density at standard conditions, g/$cm^3$ |
| $\rho_{rock\text{-}bulk}$ | Density of the bulk rock, g/$cm^3$ |
| $\rho_{oil\text{-}res}$ | Density of the crude oil at reservoir conditions, g/$cm^3$ |

TABLE OF CONTENTS

Page

LIST OF FIGURES

Page

LIST OF TABLES

Page

# CHAPTER I

# INTRODUCTION

There are significant fossil fuels resources trapped in unconventionally tight reservoirs rocks, such as shales. According to the US Geological Survey (USGS), the Wolfcamp shale in the Permian Basin of Texas contains about 20 billion barrels of undiscovered, technically recoverable resources. It is followed by other accumulations such as the Bakken field, Williston Basin of North Dakota with 7.4 billion, and the Eagle Ford formation in the Western Gulf Basin of Texas with 1.7 billion (Gaswirth 2017). Overall, the U.S. Energy Information Administration (EIA) estimates that the country has approximately 58 billion barrels of undiscovered, technically recoverable oil, and globally, estimates are close to 350 billion (EIA 2013). The estimates are subject to changes as more information about the oilfields is gathered and their characterization improved, but the order of magnitude of the volume of oil available is unlikely to change.

The United States of America (US) has been by far the pioneer in the exploitation and quantification of fossil fuels contained in tight formations. The oil industry has been aware of the existence of oil and gas within shale formations for several decades, but their exploitation was uneconomic in most cases. This was changed by improvements in horizontal drilling technology, and multiple stage hydraulic fracturing techniques, achieved in the last decades. The successful combination of those two procedures greatly increases the volume of the reservoir that can be accessed by each well, delivering economic production rates to the surface. The so called “shale revolution” started with shale gas and drastically changed the landscape of natural gas production in the US. Soon after, shale oil followed, reversing the trend of decreasing oil production in the US that had started more than three decades ago. The increase in production was driven by a growth in tight oil production from 0.5 million STB/D in 2010 to 4.3 million in 2015.

Shale oil reservoirs are being produced by primary mechanisms. The multiple stages of hydraulic fracture along the horizontal section of the wells greatly improve its communication with the reservoir, enabling the formation to expel the crude oil mainly by rock and fluid expansion. However, the poor fluid transport

through shale rock makes the movement of crude oil an energy intensive process, resulting in the rapid decline of the production rate. After five years of production, the oil rate is less than 20 % of the original production rate in most cases (Maugeri 2013, Hughes 2013). To compensate the decline and sustain production, or to increase it, operators must continuously drill and fracture new wells, resulting in the existence of tens of thousands of wells in the main unconventional plays in the US. Primary production in organic rich shale reservoirs also leads to low expected ultimate recovery. The estimates vary widely, ranging from less than 2 % to almost 16% of the original oil in place (OOIP), depending on the methods used, and whether the set of wells taken for the assessment were located inside of a sweet spot or not. In most cases, the expected recovery factor is approximately 8 % (Delaihdem 2013, Dechongkit and Prasad 2011, Bohrer et al. 2008, Clark 2009). This means that by the time oil production declines to a level at which it is no longer economical to maintain the well active, the reservoir will still contain more than 90 % of its OOIP. The presence of a large volume of remaining oil in developed oilfields with thousands of wells and existing infrastructure represents an opportunity for additional profit when complemented with the expected increase of 30% to 50% in the energy demand worldwide during the next two decades, driven by global population growth and the industrialization of countries with developing economies. Although renewables are projected to increase their share of the global energy market during that period, oil and gas are predicted to hold around 70% of the energy market and 60% of the total investment in energy, primarily supported by the limited alternatives for freight, air transportation, and by the petrochemical industry (EIA 2016, IEA 2016, BP 2016).

The oil industry is experienced in production beyond primary recovery in conventional reservoirs with good fluid transport properties. Several enhanced oil recovery (EOR) techniques, including chemical methods, thermal methods, and gas injection have been applied extensively worldwide to extend recovery beyond what is achieved by only the depletion of the reservoir energy. In the US, carbon dioxide ($CO_2$) injection is the most applied EOR technique, closely followed by steam injection (Kuuskraa and Wallace 2014). The latter is the most used thermal method for viscosity reduction in heavy oil; whereas $CO_2$ is the dominant

technique for conventional reservoirs. The industry injects 3.5 billion cubic feet per day of $CO_2$ to produce 300 thousand barrels of oil a day in about 136 active $CO_2$ projects, 77 of which are in West Texas.

$CO_2$ presents certain advantages that have helped secure its success in the EOR arena. It presents the lowest minimum miscibility pressure (MMP) with oil when compared to Nitrogen ($N_2$) and Methane ($CH_4$), causes oil swelling and viscosity reduction, has a high diffusivity, and exists in a supercritical state at the conditions of pressure and temperature found in most oil reservoirs; a high-density form that results in less conformance problems than observed with other injection gasses. These positive features outweigh its corrosive nature which is its main disadvantage.

Nevertheless, unconventional reservoirs such as shale are fundamentally different in many ways than conventional sandstone and carbonate reservoirs. The shale matrix is comprised of two components: an inorganic matrix that is equivalent to the conventional reservoir matrix, which contains large pores with diameters greater than 50 nm, known as macropores; and an organic matrix or kerogen that is characterized by the presence of smaller pores mainly ranging from 2 to 50 nm, known as mesopores. However, it can also contain an important number of micropores, with diameter below 2 nm. The size, distribution, orientation and degree of connectivity of the pores within the kerogen varies widely. Additionally, the distribution, size, prevalence, and shape of the kerogen within the inorganic matrix varies considerably (Loucks et al. 2009, Curtis, Ambrose, and Sondergeld 2010, Adesida et al. 2011, Bai et al. 2013, Chalmers, Bustin, and Power 2012, Clarkson et al. 2013).

The presence of kerogen or organic matter in shale reservoirs has been found to impact processes and mechanisms that govern reservoir performance such as fluids storage, transport, and phase behavior. Within the kerogen, gas is not only stored in a free state inside the pore space, but it is also sorbed in the organic matter (Santos and Akkutlu 2013, Sigal et al. 2013). In micropores, and small mesopores, due to the reduced space for fluid molecules to move, the flow cannot be described by the Darcy equation as other flow regimes, such as molecular diffusion, start to appear (Kang et al. 2011, Civan, Rai, and Sondergeld 2011, Krooss,

Schloemer, and Ehrlich 1998). Moreover, the fluid properties, including bubble point pressure and MMP, are affected by the attraction forces between the fluid molecules and the molecules that make up the pore walls (Charlaix and Ciccotti 2009, Jin and Firoozabadi 2016, Teklu et al. 2014). The models to accurately describe most of these phenomena are under development and significant research efforts are currently focused in these areas.

Such differences between conventional and unconventional reservoirs challenge the notion that the experience and understanding the oil industry possesses on the implementation of gas injection methods in conventional reservoirs can be translated into unconventional reservoirs. There is a lack of understanding on how the contrast in mechanisms at the pore scale can affect the implementation of a gas injection process, and the benefits of EOR in a larger scale. It is not known whether $CO_2$ or other gases can be injected into the shale matrix, or at which pressure the process should be operated. The ability of kerogen to sorb fluids introduces concerns regarding the utilization of the injected gas. More importantly, we ignore how much ultimate oil recovery would be, or if there would be any oil recovery at all. These questions are basic to define the technical and economic viability of a gas injection process.

We address such questions in this dissertation by concentrating on the problem at a larger scale. We take a step back from the pore scale and base our investigation in experimental observations made in core plugs. We show the development of a core-holder configuration that enables the physical simulation of the injection of gas through a hydraulic fracture in the laboratory. Then, we use this configuration to perform core-flooding experiments at the same pressure and temperature conditions of the reservoir, in a displacement equipment that was integrated with a CT-scanner (computed tomography scanner) that enables the observation of the changes in oil composition as the experiment progresses. In the first stage of our work, presented in chapter III, we use preserved sidewall cores as received to demonstrate that $CO_2$ can be employed to extract a significant volume of the crude oil naturally occurring in the rock plugs. We also show that the changes in saturation start occurring a few hours after $CO_2$ is injected. In the second stage of our work, documented in chapter IV, we focus on the preparation of the core plugs to facilitate the measurement

of recovery factors by the knowledge of their initial oil saturation, which was unknown in the first stage when preserved sidewall cores were used as received. We describe the cleaning process, the measurement of the porosity and $CO_2$ sorption, and the re-saturation of the core plugs with reservoir crude oil. We also present the measurement of $CO_2$ – oil MMP for the two crude oils used in the experiments. In the last stage, detailed in chapter V, we use the re-saturated core plugs in core-flooding experiments to measure accurate recovery factors. We explore in this stage the effect of pressure and soaking times to understand how operating conditions affect recovery.

In chapter VI, we dive into the mechanisms of production. We contrast experiments performed in organic rich shale core plugs with experiments using high permeability Berea sandstone. We compare $CO_2$ and nitrogen as injection gases. We examine oil compositions, and analyze the data obtained from the CT-scanning process. The differences between the recovery mechanisms encountered in this investigation, and the ones known for conventional reservoirs are illustrated using ternary diagrams. We postulate a recovery mechanism responsible for recovery, and make recommendations to increase recovery based on our findings.

We examine our laboratory results from a field perspective and address $CO_2$ utilization in Chapter VII. We do this by comparing the scale of the laboratory experiments with the field scale, and addressing the possible effects of their differences in the interpretation of our laboratory results. We also make calculations of $CO_2$ utilization with the data from our experiments. Finally, we close this work by summarizing our most important findings and highlighting our contributions in Chapter VIII.

# CHAPTER II

# ORGANIC RICH SHALE RESERVOIRS

Organic rich shales are unconventional reservoir rocks with very poor transport properties, resulting in insignificant fluid injection and production without the use of hydraulic fracturing. In such reservoirs, the equivalent permeability in Darcy terms is in the order of microdarcies or nanodarcies. The low transport of fluids through shale rock caused them to be perceived as seals rock in the petroleum industry with no production potential until about a decade ago. However, some carbonate and sandstone reservoirs also exhibit poor permeability that prevents their economic production without the use of hydraulic fracturing. The complex pore structure and composition of shale rock separates it from other rocks with poor transport, or more commonly referred as "tight rocks", mainly due to the presence of organic matter or kerogen. Nevertheless, such differences are not obvious from a production performance perspective. Unequivocally differentiating tight sandstones and carbonates from organic rich shales requires the collection and analysis of rock samples.

We devote this chapter to the description of organic rich shales. The presence of kerogen or organic matter, a nanoporous material, further complicates the pore structure of these rocks resulting in fundamental differences in their storage and transport mechanisms, and in the phase behavior of the fluids they contain; when compared to conventional high-permeability rocks. Other unconventional tight rocks can be considered a simplification of the problems and challenges associated with organic rich shales, and therefore, by covering the latter we are providing the reader with a complete collection of the characteristics and challenges of all tight rocks.

In the following discussion, we address in several instances pore size, so at this point it is useful to introduce the IUPAC classification of pores according to their size, which we use as reference in this work. It defines the pores with widths exceeding 50 nm as macropores , the ones with widths between 2 and 50 nm as mesopores, and the ones with widths below 2 nm as micropores (Thommes et al. 2015).

PORE STRUCTURE

## Investigation techniques

The study of the pore structure of organic rich shales is complicated by its multiscale nature. The existence of micro-fractures in a millimeter scale, coexisting with organic pores in a nanometer scale, require the use of different instruments for their visualization, and specialized techniques for sample preparation. We describe in this section unique characterization methods for shale reservoirs, since conventional methods fail to describe the phenomena at different scale levels.

Conventional sample preparation for petrographic analysis is not suitable for the observation of pores of a few nanometers. Thin sections impregnated with blue dye and blue fluorescent dye, 30 microns thick and with a polished surface finish with 0.5 mm diamond grit were found unsuitable to observe pores within the kerogen using a petrographic microscope equipped with a mercury lamp ultraviolet light. Polished thin sections of microprobe quality, prepared for scanning electron microscopy (SEM) using standard grinding and polishing methods, using fine grit and power, produced irregularities on the surface that exceeded the size of the pores in organic black shales from various fields. The observation of sample chips, or broken surface in general, using SEM or other imaging techniques suffer from artifacts due to the rough texture resulting from sample breakage that have been misinterpreted as pores (Loucks et al. 2009, Curtis, Ambrose, and Sondergeld 2010).

The preferred sample preparation techniques for visualization are broad argon ion milling (BIB) and focused ion milling (FIB). Broad argon ion milling can mill large areas of the sample at once but produces artifacts such as curtaining. FIB offers advantages over the more traditional lapping and polishing, and the argon ion milling technique such as high output, less preferential thinning, and site precise milling for specific features. Yet, the high energy $Ga^+$ beam can cause damage to the samples in both the subsurface and the side walls. Experimenters have developed various techniques to lessen the limitations of these preparation methods and

have obtained viable samples for observation using electron microscopy. (Loucks et al. 2009, Curtis, Ambrose, and Sondergeld 2010, Sasaki et al. 2004).

Scanning electron microscopy (SEM), field emission-scanning electron microscopy (FE-SEM), transmission electron microscopy (TEM) and scanning transmission electron microscopy (STEM), have been used extensively to explore the structure of organic shales and other materials with features in the nano-scale. SEM uses a focused beam of electrons to scan the surface of the sample, whereas in TEM a focused beam of electrons is transmitted through the sample. FE-SEM produces clearer, less electronically distorted images than the conventional SEM, and eliminates the need for placing conductive coating on non-conducting samples. STEM combines the principles of both SEM and TEM. Sample preparation is much simpler for SEM because this technique is not limited by the sample size and thickness. TEM, and STEM require very thin samples, around 100 nm to 500 nm. FE-SEM gives a good impression of the three-dimensional pore structure, but its resolution is nearly ten times below that of TEM. The information gained from the individual cross sections can be combined to produce three dimensional models of the shale samples; although, this requires the sequential preparation and imaging of several hundred of cross sections to capture only a portion of the shale rock of a few nanometers of side length. This task has been simplified by the introduction of dual beam devices capable of integrating ion-milling sample preparation with SEM imaging, which are capable of progressively milling and image a sample. The post processing, or image analysis involves the use of software to measure pore sizes individually, and to characterize their aspect ratio (Grabar et al. 1997, Ziel, Haus, and Tulke 2008, Curtis, Ambrose, and Sondergeld 2010, Loucks et al. 2009, Bai et al. 2013, Sondergeld, Ambrose, et al. 2010).

Direct imaging techniques are vital in the understanding of organic rich shales because they enable the visualization of the pore structure. However, due to the small sample size, a few millimeters at most, and the lack of confinement pressure, direct imaging techniques are of little use for field characterization. Indirect techniques such as low-pressure gas adsorption and high-pressure mercury injection capillary pressure (MICP) are also used for the characterization of the organic rich shale pore structure. They can

provide useful information regarding the pore size distribution in bigger samples. The samples for MICP are regularly crushed to sizes from 0.5 to 4 mm, oven dried, and degassed. The incremental injection of mercury up to 60,000 psig is then used to characterize the pore size distribution with an equation such as the one proposed by Washburn. MICP can provide information to a pore diameter as low as 1.8 nm, limiting this technique to the characterization of mesopores and macropores. It has been argued that below 3 nm, compressibility effects may cause some distortion in the pore structure, potential particle breakdown, and opening of otherwise closed pores. Also, fabric alteration and shrinkage of soft shales with a high clay content can occur during the drying process (Loucks et al. 2009, Curtis, Ambrose, and Sondergeld 2010, Chalmers, Bustin, and Power 2012, Clarkson et al. 2013, Bustin et al. 2008).

Micropores can be characterized with indirect techniques like with low pressure nitrogen and carbon dioxide adsorption experiments. The tests are typically performed in oven dried, degassed samples, crushed to less than 250 – 500 μm. The experimental data from low gas adsorption tests is interpreted to calculate surface area and pore size distribution. Carbon dioxide and nitrogen adsorption analysis are tied together since the analytical temperature for $N_2$ adsorption analysis of - 320 ˚F (-196 ˚C) is too low, resulting in the nitrogen molecules lacking the kinetic energy required to access the smallest micropores. In the case of $CO_2$, this temperature is 32 ˚F (0 ˚C), which provides sufficient kinetic energy. Pore size distribution from 0.35 to 300 nm have been measured with this technique. $CO_2$ adsorption is used for characterizing the microporosity (< 2nm) and $N_2$ for the meso and macroporosity (2 – 300 nm). Interpretation methods include the use of the Dubinin-Radushkevich (D-R) equation, the Dubinin-Astakhov differential pore volume plot, the Barrett-Joyner-Halenda (BJH) plot, the Brunnauer- Emmet- Teller (BET) theory, the t-plot De Boer method, and the density functional theory (DFT). The pore size distribution beyond 300 nm cannot be obtained from these techniques, and a different method such as MICP needs to be used. Also, the samples need to be pre-dried since a high vacuum is required, which can impact the pore structure in shales with high clay and moisture content (Adesida et al. 2011, Chalmers, Bustin, and Power 2012, Clarkson et al. 2013, Bustin et al. 2008).

Small angle neutron scattering (SANS) coupled with ultra-small angle neutron scattering (USANS) enable the investigation of a wide pore size distribution; it can be performed at high pressure and temperature, and is a non-destructive method. This method is not based on fluid invasion as low-pressure gas adsorption and MICP are, and therefore, is not affected by any rock-fluid interactions. The samples are previously dried under vacuum. Total porosity and pore size distribution can be extracted from SANS/USANS experiments (Clarkson et al. 2013).

Due to the wide variety of features present in organic rich shales on different scales, their characterization frequently involves the use of more than one of the described techniques. To cover the complete range of interest for pore size distribution characterization, MICP is commonly used for the meso and macropores, while low pressure gas adsorption provides the data in the meso and micropore regions. The techniques overlap for a significant range of pore sizes and some researchers have found consistent results between them, whereas others have not. Both methods are affected by interpretation techniques and assumptions, and MICP provides information about the pore throat sizes, whereas low gas adsorption is interpreted for the size of the actual pores. The data obtained from fluid invasion and indirect techniques still need to be complemented with direct observations methods based on electron microscopy to fully understand the mechanisms of fluid flow and storage by visualizing of the pore structure.

**Pore structure and morphology**

Storage, transport, and phase behavior of a reservoir rock are heavily controlled by the structure of the porous media, making its characterization a cornerstone for reservoir engineering. In organic rich shales, the presence of kerogen, a nanoporous material, complicates such characterization, as its visualization requires the use of special techniques and instruments, some of which were described in the previous section. In the following paragraphs, we collect observations from different investigations in samples from different fields, to qualitatively describe the structure of organic rich shales with the goal of providing awareness regarding their complexity.

Due to the scale at which some of the features of these rocks exist, direct visualization techniques can only cover dimensions of a few micrometers. Therefore, the observations made in one sample or group of samples from a particular field, should not be generalized throughout the entire field. For that reason, we deemphasize the origin on the samples in our discussion and focus on describing the different features that have been reported. For the most part, we do this when detailing characteristics that are common to several fields. In the cases where elements are detected in only one field or investigation, we will include the origin of the sample. Our references cover investigations in the Barnett, Marcellus, Woodford, Haynesville, Muskwa, Duvernay, Fayetteville and Eagle Ford shales in the US; and the Doig/Monterrey formations in Canada.

Organic matter contributes heavily to the porosity in organic rich shale. Most pores within the kerogen are rounded and their diameter goes from a few nanometers to a few tens of nanometers, but some go up to a few hundred nanometers. The number of small pores is usually way higher than the number of large pores. Moreover, smaller pores have been detected covering the walls of larger pores. Kerogen is highly porous; porosity of approximately 50% has been reported. Some organic matter zones with significantly high porosity, can exist adjacent to other zones with low porosity, or no porosity at all. Some rock samples show homogeneous pore size within the kerogen, between 10 to 50 nm, whereas other can display a wider size distribution. The pores can show no orientation, or they can be aligned to the laminae of the shale. Multiple crack-like pores have been observed as well. Mesopore networks have been noted to be connected to larger macropores within the kerogen. It has been proposed that the paths connecting the organic pores could be smaller than the pores, and may be below the resolution of some of the investigation techniques (Curtis, Ambrose, and Sondergeld 2010, Loucks et al. 2009, Adesida et al. 2011, Chalmers, Bustin, and Power 2012, Sondergeld, Ambrose, et al. 2010).

The amount of organic matter and its distribution varies widely from a sample to another, from a field to another, and within the same field. In some cases, these variations seem related to the presence of laminations within the rock, some of which are organic rich, and others are not. Size and shape of the organic

matter also varies. The diameters of the grains have been observed to vary from less than ten nanometers to tens of microns. A few large kerogen regions, together with multiple smaller regions are commonly present in the same sample, or the organic matter can be finely disseminated within the inorganic matrix. Kerogen can also be found filling the spaces between inorganic grains, mixed in with small quartz grains and clay. The shape of the kerogen can be rounded, non-rounded, platy, completely irregular, or angular. Some kerogen pockets have elongated shapes parallel to the bedding planes. 3D image reconstructions of small volumes of organic rich shales has suggested good connectivity of organic matter (Loucks et al. 2009, Curtis, Ambrose, and Sondergeld 2010, Chalmers, Bustin, and Power 2012).

Kerogen type have been observed in some Barnett shale samples to be predominantly type II, and TOC varies from 0.4 to 10.6%, with an average of 4% (Loucks et al. 2009, Kale, Rai, and Sondergeld 2010). Whereas in the Fayetteville, Kerogen IV has been found and TOC is around 4.04% (Bai et al. 2013). TOC for de Devonian gas shales ranges between 0.29 to 5.9%, with an average of 3.05 wt.%. TOC measured in samples from one well in the gas condensate window in the Eagle Ford ranged from 2 to 6% (Mullen 2010). Porosity in the organic matter is believed to increase with maturity as a consequence of hydrocarbon generation (Chalmers, Ross, and Bustin 2012). Samples of low thermal maturity show poor development of porous structures in their kerogen (Loucks et al. 2009).

Organic porosity can also be connected to pyrite. Pyrite framboids have been observed to contain porous organic matter between the pyrite crystals. They can also contain clay or pore space. The porosity associated to pyrite framboids seems to be much lower than that associated with organic matter. Only pyrite associated with framboids seems to contribute to porosity (Chalmers, Bustin, and Power 2012, Curtis, Ambrose, and Sondergeld 2010, Loucks et al. 2009, Sondergeld, Ambrose, et al. 2010).

Even when the kerogen is frequently the main contributor to the pore volume of organic rich shales, the inorganic matrix porosity is also significant. Some samples can have most of their porosity attributed to it. The distribution of the pores between the organic and the inorganic matrix is relevant as it determines the

wettability of the rock. The porosity in the inorganic matrix is comprised by different types of macropores. Linear and triangular phyllosilicate porosity has been noted. The linear or slit shaped pores commonly have their longer dimension parallel to the bedding planes, which suggest transport in these pores can be stress dependent. Apatite has been found to contain porosity with most pores presenting an irregular shape with apparent good connectivity. Significant porosity has been observed between clay particles and along grain boundaries between quartz and clay grains. Carbonate dissolution and re-precipitation can also lead to the existence of channels and vuggy macropores with orientations that can be horizontal, parallel to the laminae, or sub-horizontal. It can also create inter-granular porosity around quartz grains, clay and kerogen. Quartz, clay and pyrite grains as small as 15 nm have been observed (Curtis, Ambrose, and Sondergeld 2010, Chalmers, Bustin, and Power 2012).

Organic rich shales can also present other features such as crack like pores, or fractures cutting through both organic and inorganic matrices (Curtis, Ambrose, and Sondergeld 2010, Chalmers, Bustin, and Power 2012). A sample from Fayetteville contained a vuggy area of 2 x 8 μm, with a cluster of natural fractures with widths ranging from 25 – 50 nm (Bai et al. 2013). Two sets of fractures were identified in a sample from the Woodford shale, one of them was oriented horizontally and the other one near vertically (Chalmers, Bustin, and Power 2012). In samples from the Barnett shale, only one naturally occurring microfracture was identified. Cemented microfractures and fractures are present, mostly in carbonate-rich samples (Loucks et al. 2009).

**Pore size distribution**

The combination of mercury injection capillary pressure (MICP) and low gas adsorption has been widely used to examine the pore structure of organic rich shales. The two techniques complement each other because MICP is useful to detect pore throat sizes of more than 3 nm, and low gas adsorption is used from 0.35 to 300 nm. Moreover, low gas adsorption couples $CO_2$ gas adsorption for micropores from 0.35 nm to

2 nm, and $N_2$ adsorption for mesopores and macropores from 2 nm to 300 nm. The lower limit of 0.35 nm for $CO_2$ adsorption is imposed by the kinetic diameter of the molecule.

Kerogen is a highly porous material, and most shales have most of its porosity associated to the organic matter. Porosity is in organics, between grains, in pyrite framboids, fossils, within minerals and microcracks. Higher porosity samples are generally rich in mesopores and macropores (Table 1). In most cases, as the porosity decreases, so does the share of mesopores, whereas the shares of micropores or macropores increases. In a few cases, however, the inorganic matrix provides most of the pore space. Organic rich shales contain a significant amount of pores between 10 and 100 μm, though, most of their pore volume comes from pores with diameters between 3 and 50 nm. Surface area increases with decreasing pore diameter, and thus most of the surface area is provided by the micropores (Curtis, Ambrose, and Sondergeld 2010, Adesida et al. 2011, Bai et al. 2013, Chalmers, Bustin, and Power 2012, Chalmers, Ross, and Bustin 2012, Sondergeld, Ambrose, et al. 2010).

| Sample origin | Depth (m) | Porosity (%) | Mesopore/Macropore Volume ($cm^3$/100g) | Micropore Volume ($cm^3$/100g) | Median Pore Diameter (nm) |
|---|---|---|---|---|---|
| Haynesville | 4,000 | 60.2 | 2.6 | 0.1 | 4.9 |
| Doig Siltstone | 2,728 | 6.6 | 2.6 | 0.2 | 55 |
| Woodford | 3,721 | 4.7 | 1.9 | 0.6 | 5.5 |
| Marcellus | 2,583 | 3.7 | 1.4 | 0.8 | 3.9 |
| Barnett | 1,957 | 3 | 1.3 | 0.4 | 4 |
| Doig phosphate | 2,793 | 2.5 | 1 | 0.7 | 15.5 |

Table 1 – Pore size distribution for different gas shale pore systems (Chalmers, Bustin, and Power 2012)

Analysis of MICP tests showed that significant pore volume is associated to macropores. Pore size distributions can be unimodal or multimodal. Most of the mercury intrusion occurs above 10,000 psig, corresponding to pore throat size of 18 nm. The incremental mercury intrusion profiles can or cannot show a peak. When present, the peak is usually between 14,000 and 50,000 psig, corresponding to pore throat

sizes from 8 to 2 nm. Mercury intrusion only reaches a portion of the pore volume measured with helium, from 50 to 75%. This is attributed to the existence of pores and connection paths below 2 nm, and to the aperture of previously isolated pore volume by crushing the samples before helium pycnometry. MICP measurements suggest that the connection paths between pores are smaller than the pores themselves (Sondergeld, Ambrose, et al. 2010, Kale, Rai, and Sondergeld 2010, Clarkson et al. 2013).

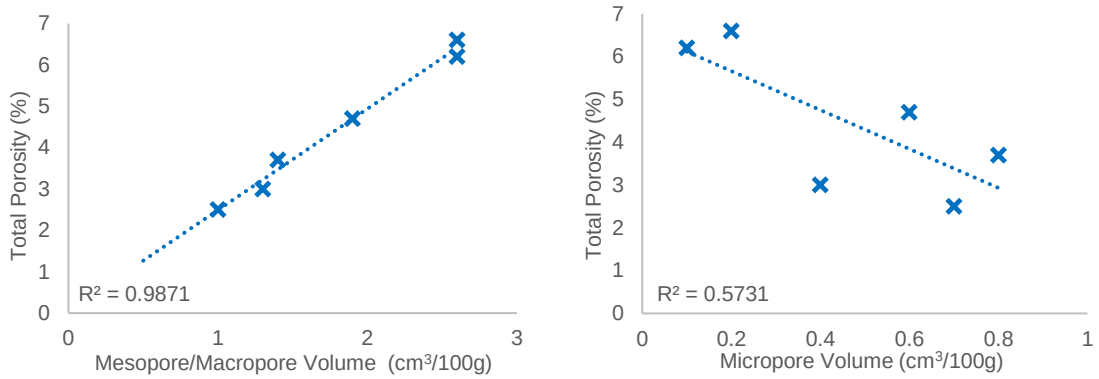


Figure 1 – Left: Porosity as a function of macropore/mesopore volume. Right: porosity as a function of micropore volume. Data from Chalmers, Bustin, and Power (2012).

According to the analysis of low pressure gas adsorption experiments, most samples present the greater pore volumes contribution from pores between 17 to 100 nm. However, in some samples, pores from 6 to 17 nm are the main contributors to pore volume. Similarly, to what has been seen in MICP tests, the pore structure can be unimodal or multimodal. Samples from the Barnett shale have shown bimodal behavior with peaks at 1 and 100 nm. Additionally, the use of SANS/USANS analysis suggested the presence of inaccessible pore volume. (Clarkson et al. 2013). In several samples from the Devonian gas shales, the micropores made out from 48 to 55% of the total pore volume, mesopores from 16 to 26% and macropores from 26 to 30%. Still, one of the samples contained 34% micropores, 40% mesopores, and 40% macropores (Chalmers, Ross, and Bustin 2012).

**Mineralogy**

Shale mineralogy controls the mechanical properties of the rock. Quartz rich samples are more brittle than clay rich ones, which is relevant for hydraulic fracturing (Bai et al. 2013). However, its influence on pore size distribution is not well established yet; and knowledge of the mineralogy is of little help to anticipate porosity. For instance, according to Bustin et al. (2008), the content of silica, carbonate, and clays have been correlated with porosity because of their influence in the amount of micropores, mesopores and macropores. In several samples, an increase in silica content, and a decrease in clay content, has been related to a decline in porosity because of a reduction in the amount of mesopores and micropores. However, the opposite has been noted for other samples where the silica is present as detrital quartz. Shales rich in detrital quartz have higher porosity and permeability than shales rich in biogenic quartz. Also, the increment in carbonate content correlates with a decrease in porosity in mitritic carbonate rich shales.

Some of these observations are consistent with remarks made about the Devonian gas shales of Canada. The samples with the highest carbonate contents showed the lowest porosity, and a positive relationship was established between porosity and quartz content. However, these trends present significant scattering (Figure 2). The increase in porosity is believed to be related to the increment in TOC with quartz content increase. Samples with less than 20% quartz have the lowest porosity and the higher share of macropores (Chalmers, Ross, and Bustin 2012).

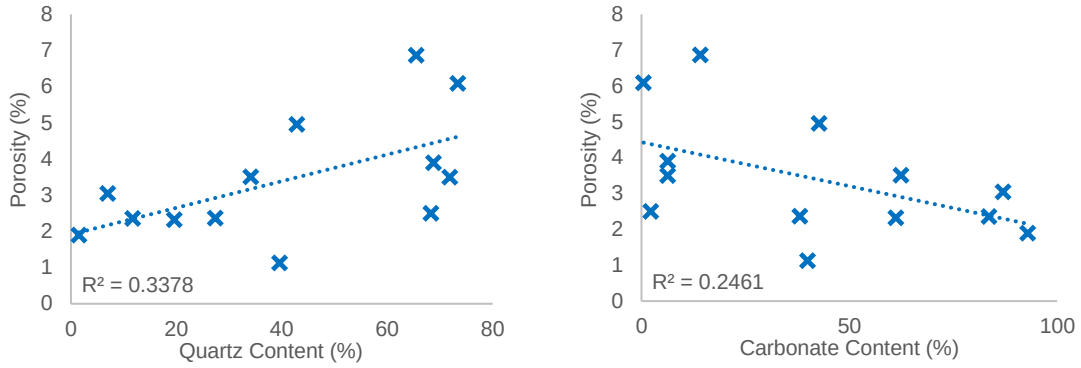


Figure 2 – Left: porosity as a function of quartz content. Right: porosity as a function of carbonate content. Data from the Canadian Devonian shales published by Chalmers, Ross, and Bustin (2012)

Kale, Rai, and Sondergeld (2010) identified three petrofacies in the Barnett shale relating mineralogy to reservoir quality. The petrofacies 1, was high in clay, TOC and quartz, and lean in calcite; and constitutes the best reservoir in the field, with high porosity, brittle and easy to fracture. Petrofacies 2, has high porosity with lower TOC than petrofacies 1, and moderate calcite content. Whereas petrofacies 3, which is rich in calcite, has the lowest porosity and TOC; and represent the worst rock in terms of productivity in the field.

In the Barnett shale, energy dispersive spectroscopy (EDS) analyses presented by Curtis, Ambrose, and Sondergeld (2010) showed the rock is composed of predominately quartz, clays, kerogen, carbonate, and pyrite in varying amounts. Also, Kale, Rai, and Sondergeld (2010) observed a wide variation in the content of carbonate and clay in a dataset of 796 samples. 64% of the carbonate was calcite, 70% of the clay was Illite, 19% of the clays where mixed clays, and the content of smectite was below 1%. Apatite and pyrite were observed in most of the samples. Porosity and TOC decreased as calcite content increased.

X-ray powder diffraction analysis (XRD) have shown that quartz, calcilte, muscovite, and illite, are the predominant minerals across several shale plays (Clarkson et al. 2013). The Fayetteville shale is predominantly quartz and illite, with small percentage of chlorite, calcite and dolomite (Bai et al. 2013). EDS analysis of the kerogen aggregates from a sample from the Haynesville showed it was composed of

carbon, aluminum, calcium, and silicon elements indicating the kerogen contains carbonates and clay. The Doig phosphate contain carbon, aluminum, silicon, calcium, oxygen and potassium (Chalmers, Bustin, and Power 2012). The Devonian gas shales of the Evie, Muskwa, Otter Park, and the Besa River formation have clay content below 35%, and are either predominantly quartz or carbonate. The clay content is mostly illite, with minor contribution of chlorite and kaolinite. There is presence of albite and pyrite as well, and a very small amount of apatite (Chalmers, Ross, and Bustin 2012). Table 2 presents the mineralogy in several samples from various fields.

| | | | Mineralogy (wt. %) | | | | | | |
|---|---|---|---|---|---|---|---|---|---|
| Source | Origin | Sample | Quartz | Carbonates | Feldspar | Pyrite | Apatite | Other | Clays |
| Chalmers, Bustin, and Power (2012) | Haynesville | | 24.39 | 21.15 | 6.68 | 2.53 | 0.00 | 0.00 | 45.24 |
| | Doig siltstone | | 58.44 | 19.08 | 15.18 | 0.60 | 1.20 | 0.00 | 5.49 |
| | Woodford | | 32.07 | 10.09 | 8.99 | 3.10 | 0.00 | 0.00 | 45.75 |
| | Marcellus | | 28.67 | 6.49 | 21.28 | 0.60 | 0.00 | 0.00 | 42.96 |
| | Barnett | | 46.65 | 7.79 | 3.80 | 3.00 | 1.50 | 1.00 | 36.26 |
| | Doig phosphate | | 20.36 | 44.91 | 18.26 | 2.10 | 3.89 | 0.00 | 10.48 |
| (Bai et al. 2013) | Fayetteville | | 45-50 | 10-20 | | | | | 20-30 |
| Chalmers, Ross, and Bustin (2012) | Devonian shales - Canada | Evie 1 | 39.56 | 39.96 | - | - | - | - | 20.48 |
| | | Evie 2 | 11.70 | 83.60 | - | - | - | - | 4.70 |
| | | Evie 3 | 34.10 | 62.40 | - | - | - | - | 3.50 |
| | | Evie 4 | 42.84 | 42.74 | - | - | - | - | 14.41 |
| | | Evie 5 | 1.50 | 92.90 | - | - | - | - | 5.60 |
| | | Evie 6 | 19.60 | 61.20 | - | - | - | - | 19.20 |
| | | Muskwa 1 | 68.30 | 2.20 | - | - | - | - | 29.50 |
| | | Muskwa 2 | 71.87 | 6.31 | - | - | - | - | 21.82 |
| | | Muskwa 3 | 68.80 | 6.30 | - | - | - | - | 24.90 |
| | | Muskwa 4 | 65.50 | 14.20 | - | - | - | - | 20.30 |
| | | Muskwa 5 | 7.00 | 87.00 | - | - | - | - | 6.00 |
| | | Otter Park | 27.40 | 38.10 | - | - | - | - | 34.50 |
| | | Besa Rvr 1 | 73.40 | 0.50 | - | - | - | - | 26.10 |
| Diaz-Perez, Cortés-Monroy, and Roegiers (2007) | Mexico | I | 18.80 | 1.20 | 6.40 | | | 7.00 | 66.60 |
| | | II | 23.40 | 14.80 | 13.70 | | | 8.40 | 39.70 |
| | | III | 23.00 | 15.10 | 8.00 | | | 10.00 | 43.90 |
| | | IV | 38.60 | 8.80 | 9.20 | | | 8.50 | 34.90 |
| | | V | 25.50 | 22.00 | 18.10 | | | 17.60 | 16.80 |
| | Brazil | VI | 21.10 | 34.80 | 5.50 | | | 9.30 | 29.30 |
| | | VII | 18.70 | 47.80 | 10.80 | | | 5.50 | 17.20 |
| Mullen (2010) | Eagle Ford | | 15.15 | 55.56 | | 5.05 | | 4.04 | 20.20 |
| | | | 21.00 | 61.00 | | 3.00 | | 4.00 | 11.00 |

Table 2 – Mineralogy of various shale reservoir rocks

The following table (Table 3) breaks down the clay content in various reservoir rocks.

| | | | Clay Content (Wt. %) | | | | | |
|---|---|---|---|---|---|---|---|---|
| Source | Origin | Sample | Illite | Kaolinite | Chlorite | Smectite | Other clays | Total Clays |
| Chalmers, Bustin, and Power (2012) | Haynesville | | 43.2 | 0.9 | 0.6 | | | 44.7 |
| | Doig siltstone | | 5.5 | 0 | 0 | | | 5.5 |
| | Woodford | | 41 | 1.4 | 3.4 | | | 45.8 |
| | Marcellus | | 33.6 | 3.4 | 6 | | | 43 |
| | Barnett | | 31.4 | 3.8 | 1.1 | | | 36.3 |
| | Doig phosphate | | 10.5 | 0 | 0 | | | 10.5 |
| (Bai et al. 2013) | Fayetteville | | 45-50 | 10-20 | | | | 20-30 |
| Diaz-Perez, Cortés-Monroy, and Roegiers (2007) | Mexico | I | 2.6 | 5.5 | | 53.8 | 4.7 | 66.6 |
| | | II | 2.9 | 4 | | 30 | 2.8 | 39.7 |
| | | III | 4.2 | 13.3 | | 19.8 | 6.6 | 43.9 |
| | | IV | 7.3 | 8.9 | | 18 | 0.7 | 34.9 |
| | | V | 2 | 4.9 | | 7.7 | 2.2 | 16.8 |
| | Brazil | VI | 6.1 | 5.1 | | 17 | 1.1 | 29.3 |
| | | VII | 2.9 | 2.1 | | 9.2 | 3 | 17.2 |

Table 3 – Clay content of various shale reservoir rocks

Similarly, in Table 4 we include the carbonate content of various shale reservoirs

| | | | Carbonate Content (Wt. %) | | | |
|---|---|---|---|---|---|---|
| Source | Origin | Sample | Calcite | Dolomite | Siderite | Total Carbonates |
| Chalmers, Bustin, and Power (2012) | Haynesville | | 18.12 | 0.00 | 3.04 | 21.15 |
| | Doig siltstone | | 1.80 | 0.00 | 17.28 | 19.08 |
| | Woodford | | 6.19 | 0.00 | 3.90 | 10.09 |
| | Marcellus | | 3.50 | 3.00 | 0.00 | 6.49 |
| | Barnett | | 5.69 | 0.90 | 1.20 | 7.79 |
| | Doig phosphate | | 22.36 | 0.00 | 22.55 | 44.91 |
| (Bai et al. 2013) | Fayetteville | | 5-10 | 5-10 | | 20-30 |
| Mullen (2010) | Brazil | VI | 55.56 | 0.00 | | 55.56 |
| | | VII | 59.00 | 2.00 | | 61.00 |

Table 4 – Carbonate content of various shale reservoir rocks

## STORAGE CAPACITY

We have focused the discussion in the complex pore structure of the organic rich shale, specially the kerogen, the component that differentiates these rocks from the conventional reservoir rocks. The kerogen or organic matter has an important sorption capacity that enable them to store fluids in a sorbed state. This introduces additional complexity to the estimation of the storage capacity of organic rich shale reservoirs. Sorption, is a general term that involves adsorption and absorption. Adsorption occurs on the surface of the kerogen, whereas absorption refers to the fluids taken on by the bitumen. Bitumen is not always present in organic rich shales. Both bitumen and kerogen are organic matter. The first is dissolved by organic solvents such as toluene and xylene, whereas the latter is not.

Because of the sorption capacity of the organic matter, there are two separate phases in the porous media. A free phase that occupies the center of the pores in the organic matter and the totality of the inorganic pores, and a phase that is sorbed in the organic matter, mainly on the walls of the inorganic pores. This has important implications for gas storage and reservoir exploitation. Gas storage is enhanced by the presence of the denser sorbed phase in the porous media. This denser phase is released as the pressure of the reservoir is depleted. At constant temperature, sorption generally increases with pressure. Meaning that as the pressure is reduced the sorbed fluids are released and they incorporate to the free phase, from where they can flow to the producing wells. This section discusses the techniques for the measurement of porosity and sorption in organic rich shales.

### Porosity

Pore volume accounts for an important portion of the storage capacity of organic rich shales. The organic matter is rich in micropores (pore diameter < 2nm), and mesopores (pore diameter between 2 and 50 nm), which are important contributors to pore volume. Chalmers and Bustin (2007) found a linear relation between the organic matter content of shale, measured as TOC, and their micropore volume. Pore volume

can be obtained from the pore size distribution determination techniques described in the previous section. However, those specialized techniques are not commonly applied to a wide range of samples because they required sophisticated equipment, are time consuming, and expensive. Instead, porosity for organic rich shales is commonly measured using a helium porosimeter, a technique widely used for conventional reservoirs.

The helium porosimeter or gas pycnometer consists of two cells of known volume; a reference cell and a sample cell; which are separated by a valve. The sample is placed inside the sample cell, and the equipment is vacuumed, and saturated with the gas selected for the measurements. The initial equilibrated pressure throughout the equipment is recorded, and then the cells are isolated by closing the valve. Pressure is either increased or decreased in the reference cell, and its stabilized magnitude is recorded. Finally, the valve is opened and the cells are communicated again. This final equilibrated pressure is also recorded. The pressures recorded during the experiments, and the volume of the cells which is known, are used in a mass balance to calculate the volume of the grains of rock inside the sample cell, also known as the skeletal volume. The pore volume is calculated as the difference between the bulk volume of the sample, and the volume of the rock grains. The bulk volume of the rock sample is typically calculated by mercury immersion. The number of experimental stages required depends on how the mass balance is stated and solved. An equation of state (EOS) is employed to account for the volume of gas at the different pressures and temperatures. A description of the equipment, the experimental procedure, and the calculation methods is detailed by API (1998).

Because of the fundamental differences in structure between organic rich shales and conventional reservoirs, there are some important aspects to consider regarding porosity measurements. The first one is that due to the poor transport of fluids through the shale matrix, porosity measurements made in core plugs are extremely slow. For a sidewall core of 1 in of diameter and around 1.5 in of length, one stage of measurement takes around one week to reach stabilization. Depending on the number of stages required by the mass balance adopted, and the extra stages that may be included for quality control, obtaining porosity can take

two weeks, a month, or even more. At least two experimental stages are required. The duration of the measurements forces an important change in the equipment. Helium porosimetry is normally performed at room conditions for conventional reservoir rocks. Yet, for organic rich shale, temperature control is required because small fluctuations in the room temperature affect the pressure in the cells, and obscures the identification of its stabilization. Also, maintaining a constant temperature simplifies the mass balance. We present in chapter IV a description of our equipment, experimental protocol, and techniques to measure porosity in organic rich shale core plugs. We incorporate the change in the volume of the grains as a function of pressure in the form of rock compressibility.

To reduce the experimental time, some researchers and most commercial laboratories have adopted the technique documented by Luffel and Guidry (1992), commonly known as the Gas Research Institute (GRI) protocol; in which porosity is measured using crushed rock material. The measurement proceeds as described previously, but the sample cell is packed with crushed rock sample that has been sieved to a certain grain size. This procedure, while widely adopted, has its flaws. Since the GRI publication does not constitute a detailed experimental protocol, small variations in the experimental procedure among laboratories have been reported to cause significant differences in the resulting porosity for similar samples. These variations in procedure include, but are not limited to, the use of different sieve sizes, different volume of rock sample, and filling the sample cell to different degrees. Also, the question of whether the crushed material is representative of the rock is an issue. Comparisons between porosity measured in core plugs and crushed rock in Devonian shale samples yielded slightly higher porosity for the crushed samples (Table 5). However, such comparison was made in a small set of samples. Due to the complexity of shale rock structure, a comparison made in a few small set of samples from the same origin, may not hold for samples from other plays, fields, or even other formations within the same field. We will present evidence in Chapter IV that samples from the same well can have significant differences. Therefore, the possibility of connecting previously isolated pores during the crushing process could result in higher porosity values and remains a valid concern.

| | Porosity (%) | | |
|---|---|---|---|
| Sample | Whole Core | Crushed Sample | Difference |
| 1 | 4.79 | 4.97 | 0.18 |
| 2 | 6.96 | 7.03 | 0.07 |
| 3 | 6.19 | 6.27 | 0.08 |
| 4 | 7.83 | 7.97 | 0.14 |
| 5 | 6.01 | 6.21 | 0.2 |

Table 5 – Porosity results on whole core and crushed shale samples (Luffel and Guidry 1992).

The crushing process also eliminates fractures and micro-fractures present in the rock samples. This can be good or bad depending on how such fractures and microfractures were generated. It is a good thing for fractures and micro-fractures created during the process of retrieving the core plug from the reservoir, or during subsequent processes as sample storage, or vacuum drying. As we mentioned when we discussed the mineralogy of organic rich shales, rocks with high content of quartz and silicates are more brittle and easily fractured. Also, samples that are not stored at controlled conditions of temperature and humidity lose moisture and this can result in the formation of micro-cracks that can artificially increase the sample porosity. In any of these situations, crushing the sample yields a porosity that is more representative of the reservoir porosity.

On the other hand, samples that are of brittle nature are also susceptible to fracturing at reservoir conditions. There is significant consensus towards the notion that natural fractures, and micro-fractures, are common features in organic rich sale reservoirs. In samples that originally contained fractures, the crushing process results in a porosity that is inferior to the real reservoir porosity, and therefore, the porosity measured in a core plug would be more representative. However, the distinction between samples that were already fractured in the reservoir, and samples that were fractured during the extraction process is not trivial, and commonly require sophisticated visualization techniques to examine the fracture surfaces for evidence of weathering, indicating the surface has not been freshly exposed.

Porosity can be measured under confinement by making additional modifications to the gas pycnometer. The principle of the measurement and the experimental protocol remains unchanged. But, by substituting

the sample cell for a core-holder, where overburden pressure can be applied, confinement can be incorporated. The advantage of this is evident. Reservoir conditions are more closely mirrored, and therefore the porosity will be closer to its in-situ value. For the measurement of fluid transport, the use of confinement is almost a requirement because the potential presence of slit pores with apertures that are sensitive to stress can significantly alter fluid transport. This is not the case for porosity. The use of confinement is certainly desirable, but there is no evidence that suggest that porosity is significantly sensitive to confinement, beyond the rock compressibility effect. The mass balance equations to solve for porosity that we present in Chapter IV account for the change in volume caused by the compressibility of the rock. We did not evaluate the effect of confinement in compressibility values.

The substitution of the sample cell by a core-holder to measure porosity and compressibility under confinement has also some negative implications. The first one is that it makes the experimental procedure more tedious, because loading and unloading the sample from a core-holder adds significant time and effort to the experiment, than when the regular sample cell is used. The second disadvantage is that most of the core plug surface will be covered by the core-holder sleeve, leaving only the plug faces available for fluid transport. This increases stabilization time even further than the already long periods mentioned earlier. Also, the combination of the multiple pieces that conform the core-holder, with the small diameter of the helium molecule makes the set-up susceptible to leakage. Indeed, the helium molecule will probably be able to diffuse through most materials of which the core-holder sleeve could be constructed. When leakage occurs, the pressure needs to be recorded for an additional time to quantify such leak; increasing even more the experimental time. In other words, after helium has saturated the totality of the volume available in the sample and pressure is close to equilibrium, the change of pressure as a function of time will be nearly constant. The quantification of that constant enables the correction of the data set for leakage. A last disadvantage is that only core plugs can be used with this method in conventional core-holders. Core plugs are not always available and several researchers have used drill cuttings for their investigations.

The nanoporous nature of the organic matter was discussed already. The pore structure can be as complicated, as to have mesopores with walls covered with micropores. The walls of these micropores could be covered by even smaller pores below the resolution of the current observation techniques. Measurements of the pore volume of such an intricate structure yields different results depending on the size of the molecules of the fluid used for the experiment. This is because a fluid of smaller molecular diameter will be able to reach smaller pores than a fluid of larger molecular diameter. The porous media acts as a molecular sieve. For instance, measuring pore volume with helium, with a kinetic molecular diameter of 0.265 nm, will result in a larger pore volume than if nitrogen is used, which has a kinetic molecular diameter of 0.315 nm. Additionally, the gas used for the experiments could be sorbed by the organic matter in the sample, and additional corrections should be made for this reason. We will address sorption in the next section. Due to its weak sorption on the organics, helium is preferred for porosity measurement (Mohammad et al. 2009, Chareonsuppanimit et al. 2012).

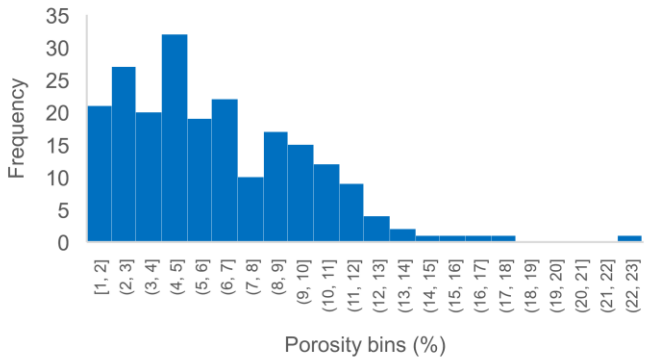


Figure 3 – Porosity distribution for 215 samples from Alberta. Data from Chalmers and Bustin (2008)

Porosity in organic rich shale is usually below 10%, but shales are of heterogeneous nature and porosity in the range of 20% have been reported for few samples (Chalmers and Bustin 2007). Kale, Rai, and Sondergeld (2010) measured helium porosity on 796 samples from the Barnett shale and obtained an average

porosity of 5.7% with a deviation of 2.1 %; the variation in porosity was from 2 to 10 percent. Chalmers and Bustin (2008) reported porosity from 215 samples from British Columbia in Alberta, Canada. They found an average porosity of 5.99% with a standard deviation of 3.57%; the porosity ranged from 0.84 to 22.16 %. Figure 3 shows a distribution of their results.

**Sorption**

The gas pycnometer is the preferred tool to measure sorption. Nuttall et al. (2005), Ross and Bustin (2009), Weniger et al. (2010), Heller and Zoback (2014), Kang et al. (2011) and Santos and Akkutlu (2013) are some of the authors that used a gas pycnometer for sorption measurement. The experimental protocol is similar to the one described for porosity measurements, however, the experiments must be run at reservoir temperature. When we discussed porosity measurements, we argued that a stable temperature was required because of the length of the experiment, and the fluctuations that the changes in room temperature cause in the pressure. However, that stable temperature does not have to match the reservoir temperature, and the resulting porosity will be similar regardless of the temperature value. Conversely, for sorption measurements, the experimental temperature must match the reservoir temperature. Sorption is a function of temperature, therefore, running the experiment at a temperature other than reservoir temperature results in a sorption capacity that differs from the sorption capacity at reservoir conditions.

As in the case of porosity, the gas pycnometer needs to be inside an environmental chamber to maintain a stable temperature throughout the measurement, and the experiment can be performed using crushed rock material, or core plugs. Also, confinement can be used if the sample cell is substituted by a core-holder. The same considerations discussed for the porosity measurements apply in the case of sorption measurements, however, the stabilization times may be even longer when measuring sorption, as the measuring gas molecules not only have to travel through the porous media to fill all the pore space, but they also must occupy all the available sorption places.

Working with crushed samples is the fastest and most popular approach for sorption measurements. Yet, there are concerns about how crushing the sample can modify its fabric, and therefore, its sorption capacity. There is also lack of uniformity in the experimental procedure. For instance, Chalmers and Bustin (2007) used a 60 mesh (250 μm) sieve for both porosity and sorption measurements; Bustin et al. (2008) reported the use of samples crushed to 20 to 35 mesh (700 μm); Kale, Rai, and Sondergeld (2010) crushed their samples to mean particle sizes varying from 300 to 600 μm, with an average of 400 μm; Weniger et al. (2010) crushed their samples to below 200 μm and Heller and Zoback (2014) reported their measurements were performed on samples crushed to particle size between 50 and 150 μm. We have observed a similar pattern with many other aspects of sample preparation. In some cases, samples are used as received. When they are cleaned and dried; there are variations in the solvents used, cleaning and drying times and temperatures, whether vacuum is applied or not, and for how long. Also, moisture equilibration is in some cases applied. These are examples of differences in experimental protocols that complicate the comparisons of results reported by different actors, and that hinder the interpretation and understanding of the true sorption capacity of organic rich shales.

For the interpretation of the experimental data, sorption needs to be accounted for in the mass balance. Fluid storage happens in the pore volume, on the surface of the organic matter, and if bitumen is present, within the bitumen. The free fluid stored in the pore volume is considered using an EOS, like in the case of porosity. The sorbed fluid is included by incorporating a sorption isotherm. The Langmuir (1917) isotherm has been widely used in the petroleum industry to model the sorption behavior of organic rich shale, some examples are the work presented by Nuttall et al. (2005), Ross and Bustin (2009), Weniger et al. (2010), Heller and Zoback (2014), Ambrose et al. (2012), Kang et al. (2011) and Santos and Akkutlu (2013). This Type I isotherm considers mono-layer adsorption; which hardly represents reality strictly. However, its simple mathematical form, rewritten as a straight line by Mavor, Owen, and Pratt (1990), and its ability to fit experimental data has driven its popularity. Alternatives to the Langmuir isotherm can be also found in literature; Chareonsuppanimit et al. (2012) reported the successful use of a simplified local-density

adsorption model instead based on the van der Walls EOS that was developed by Rangarajan, Lira, and Subramanian (1995)

Sorption, porosity, and compressibility, can be measured simultaneously. The solution of the resulting mass balance in this case requires the non-linear regression of several unknowns, which may lead to non-unique solutions (Kang et al. 2011). Instead, the general approach is to measure porosity and compressibility first using a gas with negligible sorption such as helium, then later measure sorption with the gas of interest, such as $CO_2$ or methane (Weniger et al. 2010, Chareonsuppanimit et al. 2012, Heller and Zoback 2014). Porosity and compressibility can be solved explicitly by direct substitution of the experimental data. Mathematical expressions to do so are presented in Chapter V. When the porosity experimental protocol is followed with a sorbent gas instead of helium, the outcome is the gas stored in the sample, both sorbed and free. Then, the porosity and compressibility measured previously are used to deduct the volume of gas stored in the pore volume, resulting in the excess sorption or Gibbs surface excess quantity.

Nevertheless, the molecules of fluid that are sorbed on the sample, occupy a volume that reduces the pore space calculated with helium. Such volume is relevant because of the significant amount of micropores present in organic rich shales, with diameters below 2 nm. With knowledge of its density, the volume occupied by the sorbed layer of gas can be accounted for in the mass balance to for the sorption. A common approach for approximating the density of the sorbed phase was proposed by Dubinin (1960) and uses the b constant of the Van Der Walls EOS, which accounts for the volume of the molecules. Other methods include approximating the density of the adsorbate to that of the liquified gas right below its boiling point, or to that of the solidified gas (Heller and Zoback 2014) . Chapter IV presents details of our approach to measure porosity, compressibility and $CO_2$ sorption. Another aspect to note, is that by using the pore volume calculated with helium to account for the pore space during sorption measurements with other gases of larger molecular diameter, results in the underestimation of the sorption capacity. This is because helium can reach smaller pores and occupy a larger pore volume than $CO_2$ or methane. This error is likely to be small.

The recognition of the relevance of the volume occupied for the sorbed phase, and the reduction that it causes in the volume available for free gas storage implies that gas in place calculations needs to be corrected. If not, the gas in place is overestimated. Ambrose et al. (2012) proposed a correction using the density of the sorbed phase to account for its volume. They used molecular modeling and simulation they estimate the density of the sorbed phase is typically around 0.34 g/cm$^3$ for methane. They also found such density was susceptible to changes in temperature, pressure and pore size. The gas in place calculation was later expanded to multicomponent gas mixtures by Ambrose, Hartman, and Akkutlu (2011).

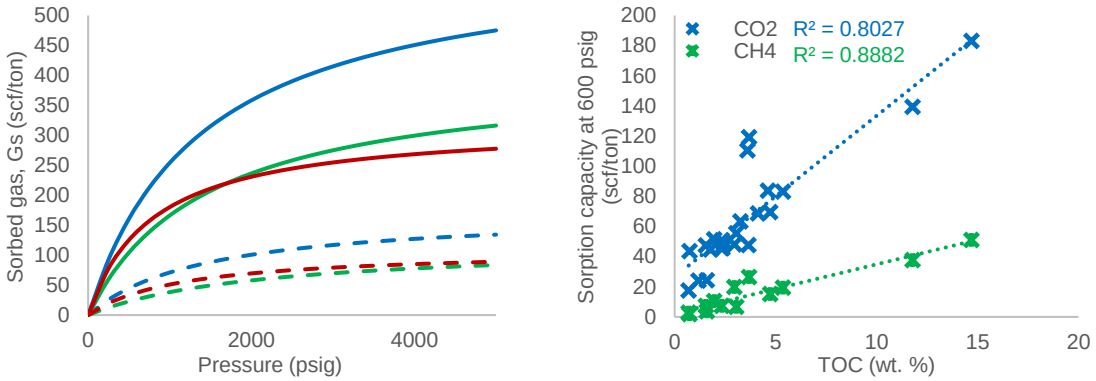


Figure 4 – Left: sorption isotherms showing higher sorption capacity for $CO_2$ than for methane. Each color represents a different sample, the solid lines are the $CO_2$ isotherms and the dotted lines are the methane isotherms. Right: Linear relationship of sorption with TOC for $CO_2$ and methane. Note that this plot also shows higher sorption capacity for $CO_2$. Data from Nuttall et al. (2005)

The sorption capacity for methane, ethane, $CO_2$, and other gases are different, and experimental measurements should be made with all the gases to determine the adsorption capacities for each one of them. Sorption capacity for $CO_2$ is significantly larger than for methane (Figure 4). Also, there is preferential sorption to $CO_2$, meaning that the organic rich shale will desorb methane to uptake $CO_2$. This is the basis for the use of $CO_2$ for enhanced gas recovery and simultaneous carbon sequestration in methane bearing organic rich shale reservoirs. For gas mixtures, the adsorption of the mixture is approximated by a weighted average using the gas composition of the independent sorption capacities of the gases involved in the mixture. This ignores possible interactions that may exist when more than one gas or substance is present.

However, if such interactions exist they would be difficult to consider in experimental measurements, since the molar fraction of each component in the sorbed phase and the free phase inside the sample cell would be difficult to establish.

Since sorption occurs within the organic matter, a positive linear relation between the sorption capacity of organic rich shales and their TOC have been reported by Nuttall et al. (2005), Chalmers and Bustin (2007), Chalmers and Bustin (2008), Ross and Bustin (2009), Weniger et al. (2010). An example of this is shown in Figure 4. Total organic carbon (TOC) is the most common measure of kerogen content in organic rich shales. The analysis consists in heating the rock in an environment saturated with oxygen until the carbon compounds are oxidized into $CO_2$, and the sulfur compounds to sulfur dioxide ($SO_2$). The combustion gases are then analyzed and the carbon content is back calculated.

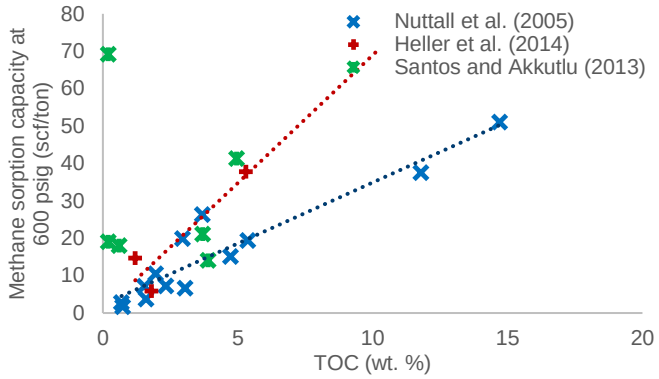


Figure 5 – Methane sorption capacity at 600 psig as a function of TOC from three different sources. Note that the data from Nuttall et al. (2005) and Heller et al (2014) follow different trends, whereas the data from Santos and Akkutlu (2013) does not show a good correlation between sorption and TOC.

TOC is the main control on sorption capacity, but the type of macerals comprising the organic matter and their maturity also influence it. Additionally, moisture content, clay content, and mineral composition have been found to have an effect on sorption capacity (Chalmers and Bustin 2007, 2008, Ross and Bustin 2009, Weniger et al. 2010, Chareonsuppanimit et al. 2012, Heller and Zoback 2014). The additional impact of

these factors is complex, and there is lack of consensus in published literature on their effect. Yet, their influence could explain why for some set of samples the linear correlation between sorption capacity and TOC is somehow poor. This can be particularly true when samples from different formations that are likely to have different mineral and maceral compositions are compared. Nevertheless, the non-uniformity of the experimental protocols needs to be considered when comparing results from different authors (Figure 5).

Table 6 shows some of the data reported in literature of $CO_2$ sorption capacity measured in organic rich shales samples, and their TOC.

| | | | | Langmuir Coefficients for $CO_2$ | | |
|---|---|---|---|---|---|---|
| Source | Origin | Sample | Formation | Volume, $G_{SL}$ (scf/ton) | Pressure, $p_L$ (psig) | TOC |
| Nuttall et al. (2005) | Kentucky-Devonian | 107928-1 | Upper Ohio | 37.5 | 681.1 | 0.69 |
| | | 107928-2 | Lower Huron | 67.6 | 243.7 | 2.95 |
| | | 107928-3 | Lower Ohio | 34.6 | 253.1 | 1.6 |
| | | 121774-1 | Ohio Shale | 126.5 | 989.8 | 3.66 |
| | | 124789-1 | Upper Ohio | 740.8 | 6,419.1 | 3.26 |
| | | 124789-2 | Lower Huron | 2,077.6 | 14,283.5 | 4.62 |
| | | 124789-3 | Lower Ohio | 116.2 | 957.9 | 1.78 |
| | | 123486-1 | Upper Ohio | 228.9 | 2,230.4 | 2.44 |
| | | 123486-2 | Lower Ohio | 309.3 | 2,106 | 4.13 |
| | | 121162-1 | Ohio Shale | 164.2 | 1,561.3 | 2.37 |
| | | 121464-1 | Upper Ohio | 52.6 | 708.9 | 1.18 |
| | | 121464-2 | Lower Huron | 248.7 | 751.2 | 3.6 |
| | | 121464-3 | Lower Ohio | 108.0 | 819 | 2.31 |
| | | 107310-1 | Selmier Shale | 607.3 | 1,390.3 | 14.7 |
| | | 107310-2 | Blocher Shale | 408.5 | 1,456.5 | 3.69 |
| | | 119139-1 | Selmier Shale | 321.0 | 781.5 | 11.79 |
| | | 119139-2 | Blocher Shale | 283.0 | 1,444.1 | 5.37 |
| | | 123957-1 | Upper Ohio | 218.7 | 1,977.5 | 2.34 |
| | | 123957-2 | Lower Huron | 271 | 1,742.0 | 4.73 |
| | | 125651-1 | Upper Ohio | 90.7 | 455.4 | 1.96 |
| | | 125651-2 | Lower Huron | 146.1 | 978.5 | 3.05 |
| | | 125651-3 | Lower Ohio | 79.5 | 493.4 | 0.73 |
| | | AEP#1-1 | Lower Huron | 111.7 | 810.0 | 1.54 |
| | | 128253-C2 | Lower Huron | 174.8 | 993.9 | - |
| Heller and Zoback (2014) | Barnett | Barnett 31 | | 147.4 | 475.1 | 5.3 |
| | Eg. Ford | Eagle Ford 127 | | 33.1 | 409.6 | 1.8 |
| | Marcellus | Marcellus | | 63.7 | 263.2 | 1.2 |

Table 6 – Some Langmuir coefficients and TOC reported in literature for organic rich shale samples

Table 7 shows some of the data reported in literature for methane sorption capacity measured in organic rich shale samples.

| | | | | Langmuir Coefficients for $CH_4$ | | |
|---|---|---|---|---|---|---|
| Source | Origin | Sample | Formation | Volume, $G_{SL}$ (scf/ton) | Pressure, $p_L$ (psig) | TOC |
| Nuttall et al. (2005) | Kentucky-Devonian | 107928-1 | Upper Ohio | 4.6 | 377.8 | 0.69 |
| | | 107928-2 | Lower Huron | 34.6 | 443.2 | 2.95 |
| | | 107928-3 | Lower Ohio | 4.9 | 176.2 | 1.6 |
| | | 107310-1 | Selmier Shale | 172.6 | 1,428.1 | 14.7 |
| | | 107310-2 | Blocher Shale | 118.7 | 2,097.6 | 3.69 |
| | | 119139-1 | Selmier Shale | 109.5 | 1,148.7 | 11.79 |
| | | 119139-2 | Blocher Shale | 68.4 | 1,513.2 | 5.37 |
| | | 123957-1 | Upper Ohio | 33.5 | 2,170.8 | 2.34 |
| | | 123957-2 | Lower Huron | 43.7 | 1,126.7 | 4.73 |
| | | 125651-1 | Upper Ohio | 36.7 | 1,497.9 | 1.96 |
| | | 125651-2 | Lower Huron | 22.7 | 1,445.3 | 3.05 |
| | | 125651-3 | Lower Ohio | 4.5 | 936.4 | 0.73 |
| | | AEP#1-1 | Lower Huron | 26 | 1,566.7 | 1.54 |
| Heller and Zoback (2014) | Barnett | Barnett 31 | | 74.4 | 580.5 | 5.3 |
| | Eagle Ford | Eagle Ford 127 | | 12.7 | 694.7 | 1.8 |
| | Marcellus | Marcellus | | 28.3 | 556.2 | 1.2 |
| Santos and Akkutlu (2013) | | S1 | | 94 | 3,394 | 3.9 |
| | | S2 | | 75 | 1,526 | 3.7 |
| | | S3 | | 78 | 533 | 4.95 |
| | | S4 | | 176 | 926 | 0.2 |
| | | S5 | | 125 | 3,334 | 0.2 |
| | | S6 | | 60 | 1,390 | 0.6 |

Table 7 – Some Langmuir coefficients and TOC reported in literature for methane sorption

## GAS INJECTION FOR EOR IN UNCONVENTIONAL RESERVOIRS

Even when gas injection is an attractive EOR alternative for organic rich shale, the difficulty in conducting experimental research on shales due to their poor transport properties have resulted in only a few laboratory investigations on the topic. All of them including significant simplifications that facilitated the experimental work, but that also limits their reliability. Sorensen et al. (2013) exposed samples from the Bakken field to $CO_2$ extraction at 5,000 psig and 230°F. The rock was cut to different sizes, with sides from a few millimeters

to a few centimeters, and in different geometries. To calculate recovery factors, they crushed the rock sample after the experiments, and extracted the residual crude oil with acetone and methylene chloride, aided by sonication. In the experiments, $CO_2$ was kept mostly static for 96 hours, with flow only to recover hydrocarbons at different intervals throughout the test. The resulting recovery factor was from 60% to 80%. A second set of tests were performed under dynamic conditions. In these tests, $CO_2$ was continuously flown during the first 7 hours, then it was kept static from 7 to 24 hours, and after that it was flown for one hour to collect the crude oil extracted. Recovery from the bigger samples in these tests reached around 40%. They observed the higher recovery factors, nearly 100%, in the samples of a few millimeters. They concluded $CO_2$ can extract oil from unconventional reservoir rocks and that higher surface areas enhance the rate of recovery.

Gamadi et al. (2014) saturated two samples of 1.5 in of length and 2 in in diameter with synthetic oil composed of a mixture of isoalkanes; from decane to tridecane. One of the samples was from the Mancos shale and the other from the Eagle Ford. They performed experiments simulating a huff-and-puff process at 95°F, and at pressures of 1,500; 2,500; and 3,500 psig. The soaking times were 6, 12, 24 and 48 hours. They reported the use of a core-holder for their experiments, but the packing and injection protocol is not clear. If the samples are representative of shale reservoirs, their permeability prohibits direct injection through the matrix. They obtained recovery factors up to 95%. They concluded miscibility had a significant impact on recovery, and that injecting at a pressure higher than the MMP does not result in additional recovery. They also found recovery factor increases with pressure and soaking time.

The same year, we published the results of our first two experiments of $CO_2$ injection using cores from the Barnett shale (Tovar et al. 2014). We used preserved sidewall cores as received. A novel configuration, detailed in Chapter III, was developed for packing our samples into a core holder to simulate injection through a hydraulic fracture, closely mirroring reservoir conditions. The experiments were performed under a huff-and-puff injection scheme, at reservoir conditions of temperature and at two different pressures, 1,600 psig, and 3,000 psig. Recovery factor was estimated to fall between 18 to 51%, based on ranges of rock

properties and saturations. We coupled our core-flooding equipment with a CT-scanner, and showed that the changes in density can be tracked as a function of time to illustrate how $CO_2$ penetrates the rock matrix. We concluded that $CO_2$ can be used to extract a significant fraction of the naturally occurring oil in organic rich shale reservoirs, that medical CT-scanning technology had enough resolution to capture the compositional changes caused by $CO_2$ injection, and we attributed recovery to an oil vaporization process.

Jin et al. (2016) exposed core plugs from the Bakken to $CO_2$ for 24 hours at 5,000 psig and 230°F. The samples were used as received, and were not re-saturated. Produced hydrocarbons were collected in intervals throughout the experiment. The residual oil in the sample after the test was measured by crushing the rock and performing methylene chloride extraction with the aid of sonication. The recovery factor ranged between 29% and 99% in 21 experiments performed. They concluded that $CO_2$ can extract oil from unconventional core samples through diffusion, and found recovery to be correlated to TOC and pore-throat size.

The experimental research so far, though encouraging, suffers from serious limitations. The use of synthetic oil, poorly described experimental procedures, limited knowledge of rock properties, experimental configurations that do not resemble reality, and the use of extremely small samples are some of them. Also, there is still significant lack of understanding of the mechanisms of recovery under gas injection for enhanced recovery in organic rich shales. In this investigation, we try to address the shortcomings of the previous experimental work.

On the other hand, numerical simulation is easier to perform and significantly less expensive than experimental research. This has prompted the publication of numerous investigations about gas injection for EOR in shale reservoirs. Some examples are Hoffman (2012), Sun, Zou, and Schechter (2016), Shoaib and Hoffman (2009), Hoffman and Shoaib (2014), Mohanty, Chen, and Balhoff (2013), Dong and Hoffman (2013), Liu et al. (2014), Yu, Al-Shalabi, and Sepehrnoori (2014), Yu, Lashgari, and Sepehrnoori (2014). We do not discuss the findings of these investigations because their relevance is questionable. This is

because as we have shown, the pore structure and composition of organic rich shale reservoirs are significantly different than conventional reservoirs, causing fundamental differences in the mechanisms of storage, transport and phase behavior. The current understanding of storage mechanisms is advanced. But that is not the case for transport and phase behavior. There is significant consensus that fluid transport through organic shale matrix cannot be solely modeled by Darcy flow, and that Knudsen, diffusion based transport mechanisms, play an important role. Various equations have been proposed, but we lack a universal model to represent transport in organic rich shale (Civan, Rai, and Sondergeld 2011, Cui, Bustin, and Bustin 2009, Akkutlu and Fathi 2012). Additionally, there is research that shows that in mesopores and micropores, the interaction among the pore wall molecules and the fluid molecules contained inside them disrupts the critical properties of the bulk fluids, altering phase behavior (Stimpson and Barrufet 2016, Teklu et al. 2014). These interactions are expected to be more complex in the case of compositional changes caused by $CO_2$ injection.

Commercial simulation is currently unable to capture any of these phenomena. This obscures the relevance of numerical simulation in the investigation of gas injection with EOR purposes in organic rich shale or unconventional reservoirs, and the results of such work should be considered with caution.

# CHAPTER III

# PROOF OF CONCEPT[1]

Preserved sidewall cores were used in the first efforts towards extracting crude oil from shale reservoirs using $CO_2$. The cores were used as received, and they had been subjected to different preservation techniques. In this chapter, we present experiments performed in core plugs from four major oil producing unconventional fields in the US: the Barnett shale, the Eagle Ford shale, the Bakken shale, and the Wolfcamp shale. The core plugs from the Barnett shale, and the Wolfcamp shale, were received preserved with aluminum foil and a plastic wrap, whereas the cores from the Eagle Ford shale, and the Bakken shale, were received preserved with aluminum foil and a wax coating.

This chapter starts with a discussion about the injectivity of gases in the organic rich shale matrix, and then will move on towards the development of our experimental technique, which resembles the injection through a hydraulic fracture. Following that, we will address the design and operation of our core-flooding device, which is integrated into a computerized tomography scan (CT-scanner ); we will close the chapter showing the experimental results that provided the grounds for the rest of our investigation.

## GAS INJECTIVITY IN ORGANIC RICH SHALE MATRIX

A core-flooding equipment was used to inject carbon dioxide, and a mixture of methane and ethane through a preserved sidewall core from the Bakken field. The back-pressure regulator of the equipment was set at 4,000 psig. The core was 1 in of diameter, and it was placed inside a core-holder, and submitted to an overburden pressure of 6,500 psig. The experiment was performed at the reservoir temperature of 240 ˚F.

[1] Part of the contents presented in this chapter have been reprinted from "Experimental Investigation of Enhanced Recovery in Unconventional Liquid Reservoirs using $CO_2$: A Look Ahead to the Future of Unconventional EOR" by Francisco D. Tovar, Maria A. Barrufet and David S. Schechter. SPE paper 169022-MS. Copyright 2014 by Society of Petroleum Engineers. Reproduced with permission of SPE. Further reproduction prohibited without permission.

Gas injection was attempted at a rate of 0.01 $cm^3$/min and the pressure difference between the inlet and the outlet of the core was recorded as a function of time (Figure 6).

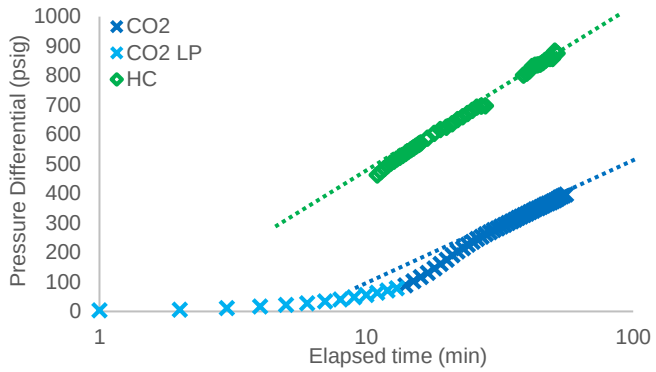


Figure 6 – Hydrocarbon gas and carbon dioxide injection in a preserved sidewall core from the Bakken shale

The continuous increment of the pressure differential shows the permeability of the organic rich shale plug matrix is extremely poor. If we assume steady state flow of the mixture of methane and ethane at the maximum differential pressure reached during the experiment of 875 psig, we obtain a permeability of 0.0652 md. However, the experimental data shows that steady state was not reached. Therefore, the flow under steady state conditions of a 0.01 $cm^3$/min of the gas mixture would require a higher differential pressure indicating that the sample permeability is lower.

The experimental results support what we already knew about the shale matrix. That it is not possible to inject any significant amount of fluids in a reasonable timeframe through it, even if that fluid is a gas with a very low viscosity. As we discussed during the introduction, there are already tens of thousands of wells with several hydraulic fracture stages along their horizontal section in all major unconventional plays in the US. We can and should visualize the application of gas injection as a process that follows the primary

production of the well and takes advantage of the existing infrastructure. For doing so, we developed a technique to simulate this in the laboratory, which is described in the following section.

## EXPERIMENTAL EQUIPMENT AND PROCEDURE FOR THE ASSESSMENT OF EOR POTENTIAL

### Physical representation of a hydraulic fracture

In a hydraulic fractured well, a high permeability medium provided by the proppant is in direct contact with a low permeability matrix rock. We reproduced this situation in the laboratory by surrounding the organic rich shale core plug by a high permeability medium created by using glass beads of 1 mm of diameter (Figure 7). The glass beads are held together using a Teflon tubing that shrinks when exposed to heat, and by filters placed on each end to prevent them from flowing through the injection and production lines. On top of the Teflon tubing, a Viton sleeve is placed which separates the system hydraulic fracture – reservoir, comprised by the glass beads and the organic rich shale core plug, from the water used for confinement. This set up is placed inside an aluminum core-holder with a carbon composite cover that enables the penetration of X-rays, and by extension, CT-scanning.

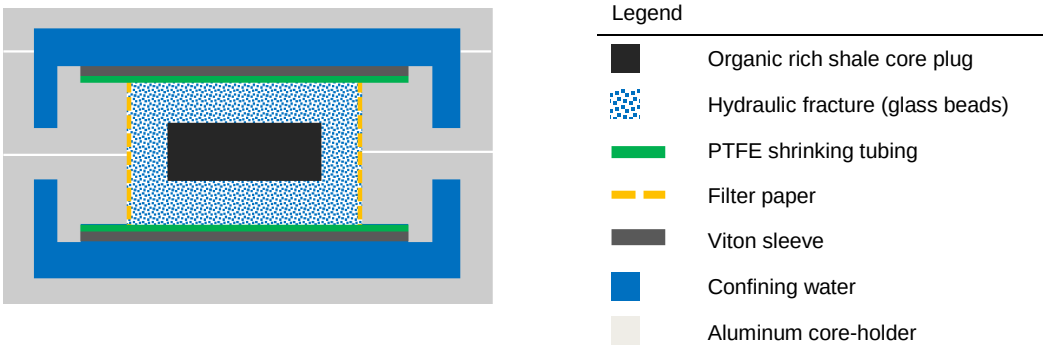


Figure 7 – Schematic of the experimental representation of a hydraulic fracture well in an organic rich shale reservoir

**Imaging capable core-flooding equipment**

The core-holder, packing the core plug surrounded by glass beads and under confinement is placed in the core-flooding equipment depicted in Figure 8. The equipment has the capability to heat and circulate the water used for confinement to maintain the core-holder at reservoir temperature, while a dome loaded back pressure regulator provides for accurate control of reservoir pressure. Injection gas is stored at high pressure in floating piston accumulators and injected at the desired rates using a syringe pump. The injection line is also heated to reduce temperature contrasts at the entrance of the core-holder.

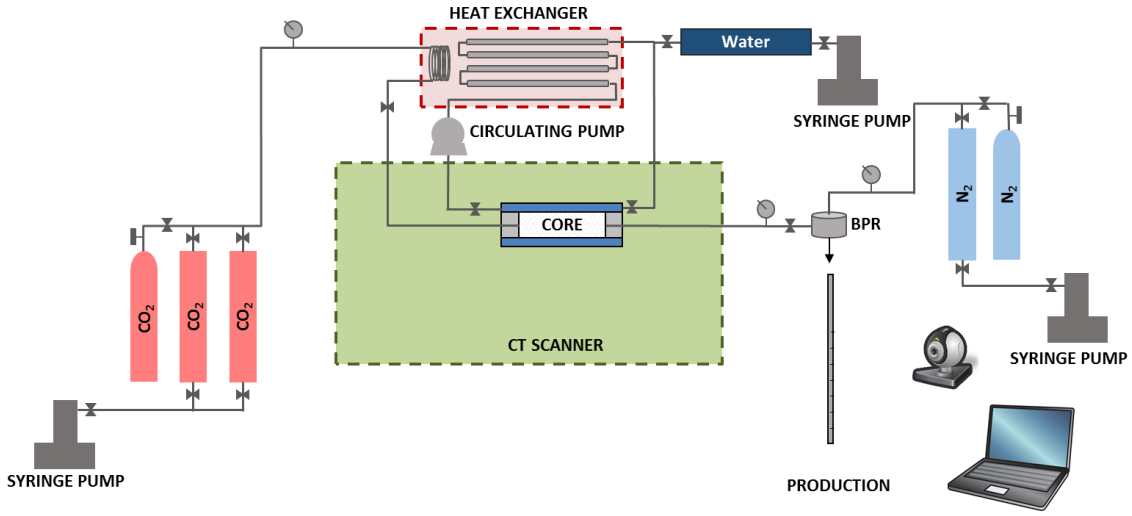


Figure 8 – Schematic representation of the core-flooding device capable of capturing images of the interior of the core-holder by the use of CT-scanning

Digital pressure gauges, thermocouples, and a recording device are connected to a computer to monitor experimental pressure, temperature, and to measure the produced oil. The entire system is built on a medical CT-scanner with an isotropic resolution of 350 micron. The CT-scanner makes it possible to monitor the interior of the core-holder throughout the experiment and track the changes that happen due to the injection of fluids and production of hydrocarbons.

**Experimental protocol**

The injection of gas for EOR in organic rich shale is commonly visualized as a huff-and-puff process. Poor transport properties of organic rich shale prevent the flow of gas from an injector to a producer in a reasonable time frame without the presence of fractures. However, the presence of fractures as a requirement for well-to-well communication, also implies the existence of a direct path from injector to producer for gas recirculation, which is linked to a loss in efficiency, or poor gas utilization. In the laboratory, however, we simulate both huff-and-puff and continuous injection. Contrasting these two schemes provides for better understanding of the importance of soaking time in the process, as it will become clear in the following chapters.

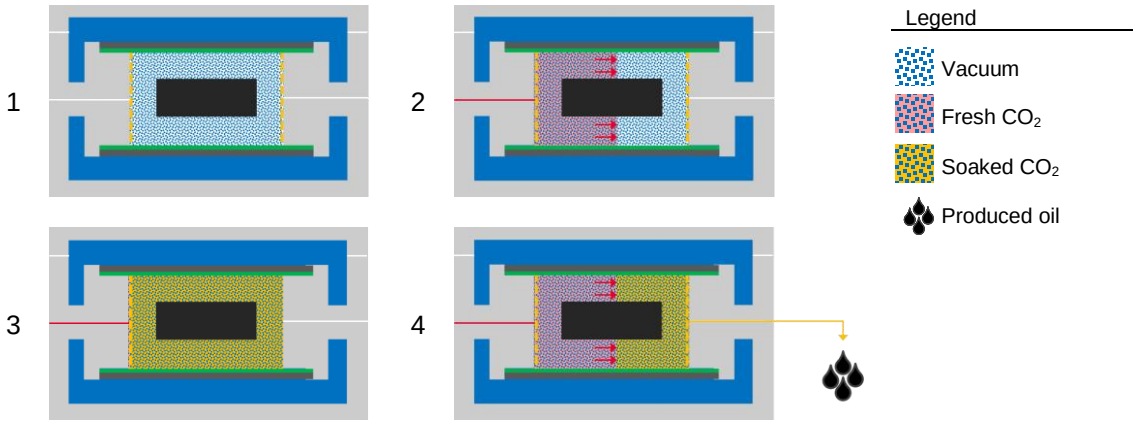


Figure 9 – Stages of the injection process. (1) Air is extracted and the core-holder is under vacuum. (2) $CO_2$ is injected from the accumulators. (3) Soaking is allowed. (4) The $CO_2$ that has been soaking the core is replaced by fresh $CO_2$

The stages of the experiment are depicted in Figure 9. Every test begins by extracting the air from the core-holder, and all other components of the core-flooding equipment with a vacuum pump. This step of the process is conducted for approximately 30 minutes. After that, $CO_2$ is injected from the floating piston accumulators until the desired experimental pressure is reached. The core is then soaked in $CO_2$ for a number of hours that vary from one experiment to another. During soaking, the core is scanned multiple times using

the CT-scanner to track the changes in saturation. When the soaking period has ended, the $CO_2$ inside the core-holder is displaced by injecting fresh $CO_2$. The effluents produced while the $CO_2$ is displaced are collected and measured. The described procedure constitutes one experimental cycle; during each run, several cycles are performed until the core ceases to produce oil.

A huff-and-puff process implies that the pressure is depleted during the "puff" stage, and increased during the "huff" stage. In that regard, we contrast the traditional huff-and-puff because the pressure in our experiments remained constant. In the field, increasing and decreasing the pressure is necessary to inject and produce from the same well. However, this can be avoided in the laboratory since we can inject and produce through different ports in the core-holder. Moreover, increasing and decreasing the pressure would hinder the interpretation of the effect of pressure in recovery. Soaking time was usually from 8 to 22 hours; however, we did perform several tests with zero soaking times representing the case of continuous injection.

**Experimental matrix**

Nine experiments were performed in this stage using cores from the Barnett, Wolfcamp, Bakken and Eagle Ford shales (Figure 10). The pressure was varied from 1,500 psig to 4,000 psig, and the soaking time from zero, which are the cases of continuous flooding, to ten hours. All the experiments were carried out at temperatures between 150 and 170˚F, and the core plugs were used as received. The huff-and-puff cycles were continued until no additional oil production was observed. For the experiments that did not show any oil production, at least four huff-and-puff cycles were performed.

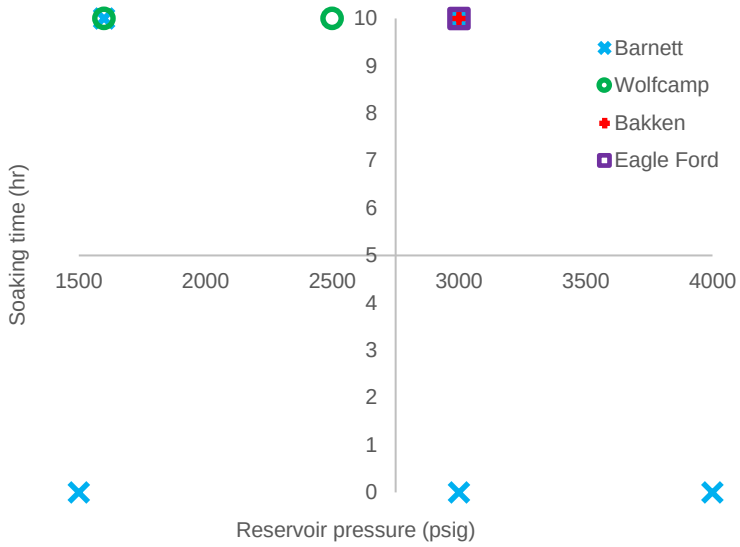


Figure 10 – Experimental matrix for the core-flooding experiments performed on preserved sidewall cores

## RESULTS AND DISCUSSIONS

Out of the nine experiments performed, only three yielded a measurable amount of oil recovery (Figure 11). All the core plugs were used as received and we did not have information about their porosity and oil saturation. To estimate how successful these experiments were, we defined two scenarios. The low end or pessimistic scenario assumes a porosity of 6% and an oil saturation of 100%. This scenario maximizes the initial volume of oil in the core, and therefore, minimizes the recovery using $CO_2$ injection. The high end or optimistic scenario assumes 3% porosity and an oil saturation of 70%. This scenario minimizes the volume of oil in the core, and maximizes the recovery during the experiments. Our current knowledge of the properties of organic rich shales would probably lead us to define the scenarios somehow different. However, we decided not to update our original assumptions to provide the reader with a clearer vision of what our line of thought was at this stage of the project.

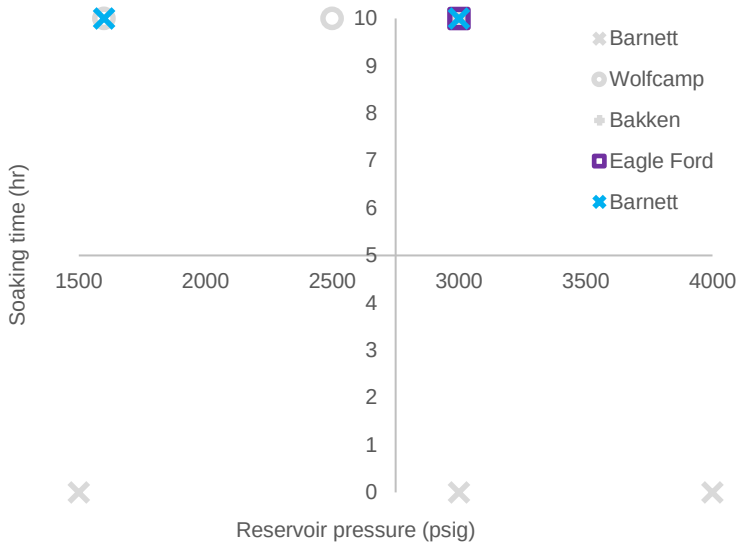


Figure 11 – Experimental matrix for the core-flooding tests performed in preserved sidewall cores. The experiments in gray did not have measurable oil recovery.

Following the assumptions made for porosity and oil saturation of the samples, the recovery factor was estimated to be between 18 and 62% in all tests. These results, even when linked to a high level of uncertainty, demonstrate indisputably that $CO_2$ can be used to extract the naturally occurring oil in organic rich shale reservoirs, establishing the technical feasibility of the method.

| | | | | Recovery Factor | |
|---|---|---|---|---|---|
| | | | | Low end scenario | High end scenario |
| Test | Field | Test pressure (psig) | Soaking time (hr) | Por = 6 % $S_o$ = 100 % | Por = 3 % $S_o$ = 70 % |
| 1.1 | Barnett | 3,000 | 10 | 18 | 51 |
| 1.2 | Barnett | 1,600 | 10 | 19 | 55 |
| 1.3 | Eagle Ford | 3,000 | 10 | 22 | 62 |

Table 8 – Recovery factors scenarios for the tests were a measurable amount of oil was recovered during the core-flooding experiments performed in preserved sidewall core plugs

CT-scanning uses the attenuation of several X-rays when passing through an object in multiple directions to produce, using computer algorithms, a three-dimensional image of such object. By scanning the

experimental set up multiple times we added time as a fourth dimension. Figure 12, presents CT-images taken from test 1.1 (Table 8). The scale at the left in Figure 12 is in terms of Hounsfield units, commonly referred as CT-numbers. The Hounsfield unit is directly correlated to the density and composition of the material scanned, where higher CT-numbers correspond to higher density. For instance, the CT-number of air is -1,000 HU, whereas for water is 0 HU.

For test run 1.1 the evolution of CT-number as a function of time for two slices of the core plug are presented in Figure 12. The test was conducted at 3,000 psig and 150 ˚F. It is evident from the images, that $CO_2$ starts penetrating the core within a few hours after the experiment is started. This observation was unexpected, given the low transport properties of the organic rich shale matrix, and the poor gas injectivity observed experimentally (Figure 6). In this case, the CT-number is increasing with time because of a rise in density of the oil, resulting from the penetration of $CO_2$.

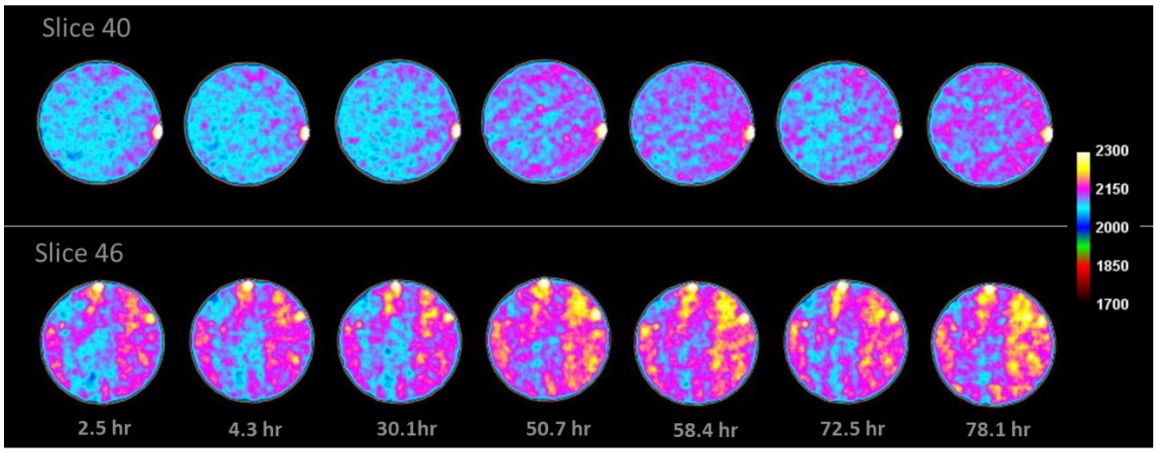


Figure 12 – CT-scan images from experiment 1.1 showing the changes in CT-number as a function of time for slides 40 and 46 of the preserved sidewall core.

The increase of CT-number as a function of time for test run 1.1 can also be observed to the left of Figure 13. To the right of the same figure we show the CT-number as a function of time for the test run 1.2

performed at 1,600 psig and 150˚F. Both tests were done using core plugs from the Barnett shale. The CT-number presented in Figure 13 is the average CT-number for the two samples used in each of the tests. In test runs 1.1 and 1.2, two samples were packed instead of one to maximize the volume of oil recovered and facilitate its measurement. In all other tests presented in this work, only one sample was employed. The change of CT-number as function of time reaffirms the deductions made from the observation of the CT-images. Within hours of initiating injection, $CO_2$ begins penetrating the organic rich shale core plugs; which changes the composition of the oil, resulting in a change in density that is reflected in the CT-number.

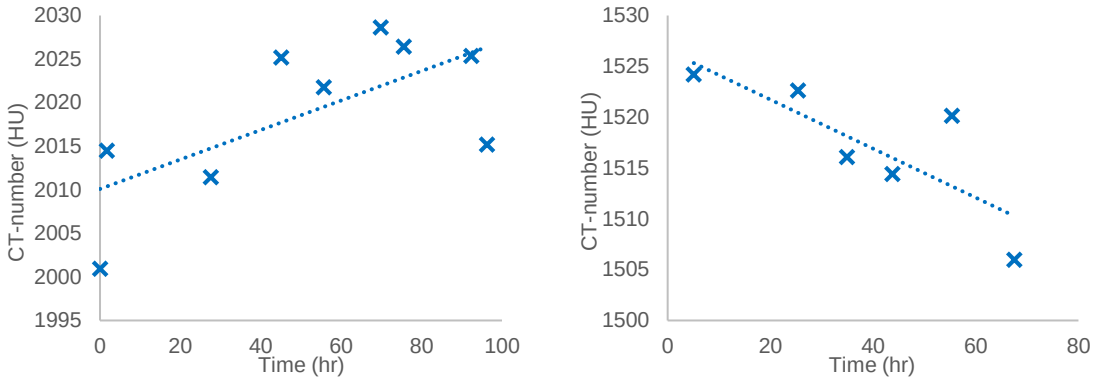


Figure 13 – CT-number as a function of time. Left: Test 1.1 at 3000 psig and 150 F. Right: Test 2.2 at 1600 psig and 150 F. Both experiments were performed with core samples from the Barnett shale.

The change in CT-number as a function of time follows opposite trends in tests runs 1.1 and 1.2 (Figure 13). The only difference between both tests is the pressure, test run 1.1 was done at 3,000 psig, whereas test run 1.2 was done at 1,600 psig. Figure 14 shows density as a function of pressure for $CO_2$, butane, pentane, hexane and heptane. It also shows the conditions of test runs 1.1 and 1.2. We do not know the composition of the oil, but we know it is a light oil that is likely rich in intermediate components. The trends in the change of CT-number with pressure in Figure 13 can be explained by the behavior of density shown in Figure 14. For the test run 1.1, performed at 3,000 psig, the density of the $CO_2$ is higher than the density of the hydrocarbons intermediate components. As time goes by, the lighter components of the oil are vaporized

into the $CO_2$ contained in the high permeability medium comprised of the glass beads, while simultaneously, $CO_2$ is dissolved in the oil within the core sample. Since the oil is releasing lighter hydrocarbon components with lower density and taking in $CO_2$ of higher density, the result is an increment in the overall density of the oil, and therefore, its CT-number, with time.

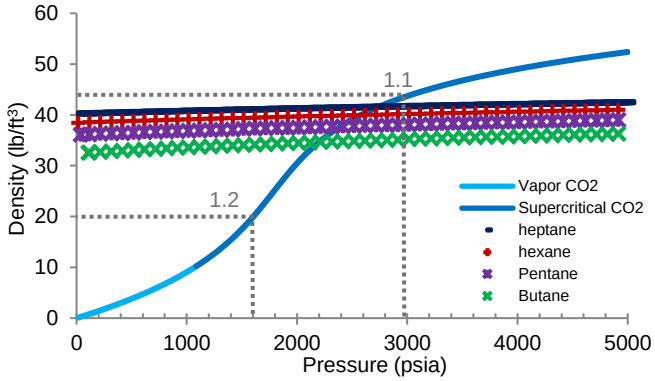


Figure 14 – Density as a function of pressure for $CO_2$, butane, pentane, hexane and heptane. The conditions of test runs 1.1 and 1.2 are shown.

For the test run 1.2 the opposite happens. At 1,600 psig the density of the $CO_2$ is much lower than the density of the intermediate hydrocarbon components (Figure 14). As the experiment advances, the lighter components of the oil are vaporized into the $CO_2$ occupying the high permeability medium surrounding the core. But in this case, the oil is releasing lighter hydrocarbon components, and taking in $CO_2$ of a lower density, resulting in a reduction of the density of the oil inside the core, and therefore, its CT-number.

Additionally, the appearance of the produced oil supports our hypothesis. The oil collected during the experiments had a yellow coloration for the three test runs where oil was produced. However, only the Eagle Ford wells produce oil of a similar color in the field. The area in the Barnett shale where these cores were collected produces crude oil of a black coloration. This indicates we are producing only the lighter components of the oil within the core. These lighter components are stripped out and vaporized in the $CO_2$

stored in the high permeability medium surrounding the core during the soaking time. When the $CO_2$ is displaced out of the core-holder and flashed at room conditions the hydrocarbon components condense and are collected.

The discussion so far has been centered in the experiments where oil was produced, but those were only three out of nine runs. Those three experiments, however, yielded crude oil production from the first huff-and-puff cycle, indicating the process is fast, which is also supported by the plot of CT-number with time and by the CT-images. But most of the experiments, six out of nine, produced no oil at all, or they produced an amount of oil that was too small to be measured. Our results, are in a totally opposite side of the spectrum. We either produced a large amount of oil, or have no production at all. This contrast led us to suspect the reason behind the unsuccessful runs was low oil saturation. Since the core plugs were used as received, there is no guarantee that all samples contain a substantial amount of oil. Actually, given the heterogeneity intrinsic to oil reservoirs, retrieving cores with different degrees of oil saturation is very likely.

## SUMMARY

The work presented in this chapter laid the ground for the rest of this investigation. We first showed, experimentally, that injecting gas directly into the matrix of organic rich shale reservoirs is not feasible. Nevertheless, since the oil shale fields in the US already contain tens of thousands of wells with multiple stages of hydraulic fractures, that will be available for gas injection after primary production is exhausted, we developed a physical model to simulate in the laboratory the injection of $CO_2$ through a hydraulic fracture. We built equipment that enabled the experimental simulation of huff-and-puff and continuous gas injection at pressure and temperature equivalent to the reservoir, and we integrated it to the CT-scanner to monitor the changes in density inside the core plug as a function of time.

We performed nine core-flooding experiments using preserved sidewall cores from the Barnett, the Eagle Ford, the Bakken, and the Wolfcamp shale. Three successful experiments yielded significant oil recovery,

demonstrating the technical feasibility of using $CO_2$ to extract the naturally occurring crude oil from organic rich shale core plugs. More importantly, the time frame for this recovery process was surprisingly fast, resulting in oil production starting in the first huff-and-puff cycle, even with the low transport properties of the reservoir rocks. Observation of the CT-images and the CT-numbers as a function of time, indicated that $CO_2$ penetrates the core within hours of being injected, dissolves in the oil, and strips out the lighter hydrocarbon components causing changes to the crude oil composition and density. The vaporized hydrocarbon components are then transported outside with the displaced $CO_2$ at the end of each huff-and-puff cycle, where they are condensed as the $CO_2$ is flashed at room conditions.

The experimental results so far have provided an assessment of the potential of $CO_2$ for EOR in organic rich shales and a good understanding of the mechanisms responsible for production. However, there is still a lot of uncertainty surrounding the recovery factor. The lack of knowledge of the porosity and oil saturation in the preserved sidewall core samples prevents us from making accurate recovery factor calculations. With assumptions, we estimated recovery to fall between 18 and 62 % of the initial oil in the samples. Although, we recognize that this range needs to be narrowed for it to be of any use for economic estimations. Additionally, in the experiments in which oil was not recovered we concluded that the uncertainty of the oil saturation was responsible. In this situation, it is imperative that we know the porosity and oil saturation so we can reduce the uncertainty of our results. Additionally, we must have knowledge of the composition and the minimum miscibility pressure (MMP) of the system crude oil – $CO_2$ would add to the understanding of the recovery mechanisms.

Additionally, we realize that the organics in shale reservoirs can adsorb some gases. Hence, the $CO_2$ injected will not only go to the porous space, but it will also be sorbed by the organic matter. This opens interrogations regarding $CO_2$ utilization. If the sorption capacity of the reservoir rocks is high enough to store a significant amount of the $CO_2$ injected, this could increase the volume of $CO_2$ required to produce a barrel of crude oil, or $CO_2$ utilization, to a level that can make the project uneconomical. Consequently, the assessment of $CO_2$ sorption is required to evaluate the economic potential of the process.

# CHAPTER IV

## ROCK AND CRUDE OIL CHARACTERIZATION AND PREPARATION[2]

The experimental work performed in preserved sidewall cores revealed the need for a better characterization of the rock and the crude oil samples so that we could improve the assessment of the recovery factor, the production mechanisms, and to gain some understanding on the $CO_2$ utilization. This chapter documents a long, but necessary, and fruitful detour in our project. Here we describe the equipment and the methods we used to clean the organic rich shale core samples, measure their porosity and gas sorption, and to re-saturate them with crude oil from the corresponding formations. Additionally, we show the measurement of the minimum miscibility pressure of the system crude oil – $CO_2$ for the two oils used, and we address our use of dopants in the crude oil to improve the visualization during CT-scanning. Even when we show some interesting findings regarding the pethrophysical characterization of organic rich shale samples, the main purpose of this chapter is to describe how we produced core plugs of known porosity, $CO_2$ sorption, and oil saturation that are used later for gas injection experiments with EOR purposes. All the equipment described in this chapter, apart from the slim tube apparatus used for the MMP measurements, was designed and built in house as a part of this research work.

### CORE SAMPLES

We decided to focus the rest of the investigation in the Wolfcamp formation of the Permian basin, one of the most prolific organic rich shale oil accumulations in the US. Focusing on just one field enabled us to use the same oil in several experiments at different conditions, gain more knowledge regarding the effect of the operational conditions on recovery, and the mechanisms responsible for oil production. On the contrary,

[2] Part of the contents presented in this chapter have been reprinted from "Non-Destructive Measurement of Porosity, Compressibility and Gas Sorption in Core Plugs from the Wolfcamp Shale" by Francisco D. Tovar, Maria A. Barrufet and David S. Schechter. SPE paper 185604-MS. Copyright 2014 by Society of Petroleum Engineers. Reproduced with permission of SPE. Further reproduction prohibited without permission.

having samples from multiple fields saturated with their respective oil would make comparisons among experiments less valuable.

We used a total of 11 samples in this investigation taken in two different wells (Table 9). Core plugs from one through three were recovered from well 1, and the rest of the samples were collected from well 2. The samples from well 1, were delivered to us preserved with plastic wrap and aluminum foil, whereas the samples from well two were received unpreserved. Upon their arrival, all core plugs were stored at controlled conditions of humidity and temperature to prevent their dehydration and the generation of cracks.

| Sample | Well | Depth (ft) | Volume ($cm^3$) | Mass (g) |
|---|---|---|---|---|
| 1 | 1 | 8,344.1 | 20.74 | 49.58 |
| 2 | 1 | 8,350.1 | 25.43 | 65.07 |
| 3 | 1 | 8,377.1 | 22.93 | 60.58 |
| 4 | 2 | 8,469.3 | 19.49 | 50.21 |
| 5 | 2 | 8,470.8 | 19.32 | 50.72 |
| 6 | 2 | 8,471.8 | 18.80 | 49.00 |
| 7 | 2 | 8,484.7 | 18.99 | 50.52 |
| 8 | 2 | 8,486.8 | 19.68 | 48.96 |
| 9 | 2 | 8,490.35 | 18.91 | 50.28 |
| 10 | 2 | 8,491.4 | 19.51 | 51.56 |
| 11 | 2 | 8,497.6 | 18.97 | 50.88 |

Table 9 – Mass, volume and depth of the core samples from the Wolfcamp formation used in chapters IV, V and VI.

## CLEANING

Core cleaning was done using Dean-Stark extraction (Dean and Stark 1920). The apparatus is depicted in the recommended practices for core analysis published by API (1998), and it is equivalent to the one used to clean and measure fluids saturation in conventional sandstone and carbonate reservoir rocks, with moderate and high permeability. The exposure time for the organic rich shale samples was greatly increased due to their poor transport properties. The first stage of the extraction was carried out for two weeks using toluene. The two weeks period was selected after monitoring weight variation with extraction time. Toluene extraction was followed by one week of methanol extraction intended to remove salts that may remain in

the porous media, and to facilitate the drying process. In our samples we did not see any indication of the presence of salts, however, SEM images were provided to us showing salt crystals in core samples from the Bakken shale, prompting us to include the methanol extraction stage as a precaution.

Dean-Stark extraction was performed only for cleaning purposes. We did not recover any water from the cores, and since we did not know the oil density, the gravimetric calculation of oil saturation was not possible. We attempted to estimate the volume of oil removed by performing gas chromatography on the toluene used for extraction, but the high volume of toluene compared to the small volume of oil made the oil components undetectable. Our attempt to calculate the remaining oil saturation in the cores aimed to provide post-mortem information about the recovery factors in the experiments performed with preserved sidewall cores.

The use of a solvent, such as toluene, during Dean-Stark extraction has been suggested to lead to the dehydration of clays as a consequence of the wetting nature of the solvent, so caution should be paid when working with samples with high clay content (Handwerger et al. 2012). Kerogen is not soluble in toluene, but bitumen is. If the samples are believed to contain a significant amount of bitumen the use of solvent extraction for cleaning is not advised. We have no indication of the presence of bitumen in the samples used in this investigation.

Following the extraction process the samples were dried in a vacuum oven at a temperature below reservoir temperature for at least ten days. Reservoir temperature was not exceeded to assure the samples do not suffer fabric alterations during the drying process. The duration of the drying process was established by gravimetric analysis of a few samples.

## POROSITY AND COMPRESSIBILITY

We used a gas expansion pycnometer to measure porosity and compressibility. The same equipment was also used later to measure gas sorption. We avoided the common practice of using crushed rock material for porosity measurements because we intended to measure the porosity of the same core plugs to be used later to measure recovery. Also, we were concerned about the possibility that by crushing the sample we could connect pores that would otherwise be isolated, leading to higher porosity.

One obvious disadvantage of using core plugs instead of crushed rock material is the increment in the experimental time. Measurements take several days when they are performed in rock plugs. For this reason, we discarded the possibility of using confining pressure in our measurements. The use of confining pressure requires the core plug to be packed in a core-holder. Constantly packing and unpacking samples from a core-holder can be arduous and time consuming. The architecture of the core-holder only permits the measurement gas to access the rock through the ends of the sample, further increasing experimental time. Moreover, helium is commonly used for porosity measurement because of its negligible sorption in the organic matter. But the helium molecule is extremely small, of only 0.265 nm, making leaking through the confining sleeve of the core-holder almost inevitable. The presence of leaks leads to increased experimental time to collect the required data to make corrections. We believe confinement has an unimportant effect in the measurement of porosity. Conversely, for the quantification of transport capacity small changes in the width of slit pores due to confinement can have a meaningful impact and confinement should not be neglected.

### Gas expansion pycnometer

A gas expansion pycnometer was built in house (Figure 15). The equipment is made of a reference cell and a sample cell, separated by a needle valve (valve 3). The internal diameter is 1 in for the reference cell and 1.1 in for the sample cell. Both cells have an internal height of approximately 1.7 in. The equipment is

provided with a gauge pressure transducer with an accuracy of ±0.08% (BSL or best straight line; combining linearity, hysteresis and repeatability), and capable of making 1,000 readings/second, connected to a computer to record pressure data as a function of time. Gas is fed to the equipment directly from a compressed gas cylinder or it is pressurized further using a syringe pump and a floating piston accumulator. A vacuum pump is attached to remove air from the cells and the pore space of the sample. The cells are placed inside a forced convection oven that can control the temperature with an accuracy of 0.1 ˚C.

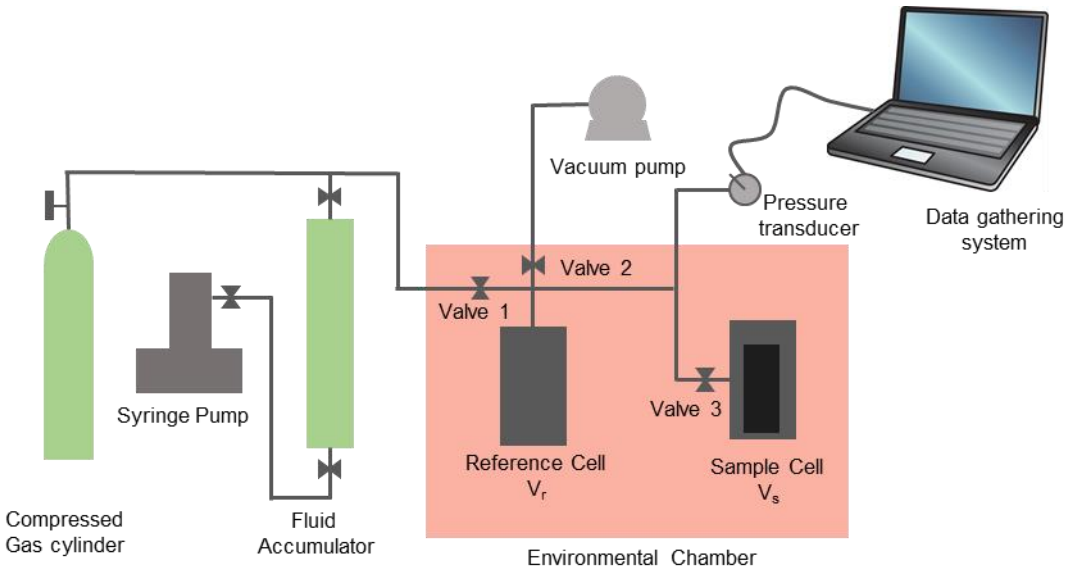


Figure 15 – Schematic representation of the gas expansion pycnometer used for the measurement of porosity, compressibility and gas sorption.

**Experimental procedure**

To measure porosity, the rock sample is placed within the sample cell and vacuum is applied to both the sample and reference cell, for at least eight hours. We performed the measurements at reservoir temperature (165 ˚F), but a temperature different than reservoir temperature can be used as far as it is kept constant throughout the experiment. For the first measurement stage, helium from the compressed cylinder is allowed

into both cells, and pressure is monitored for stabilization. This can take anywhere from a few hours to a few days depending on the transport properties of the sample. The stabilized pressure is recorded as the initial sample cell pressure ($p_{si_1}$). Valve 3 is closed to isolate the sample cell from the reference cell, and more gas is allowed to enter the reference cell, increasing the cell pressure. The stabilized pressure of the reference cell is now recorded as the initial reference cell pressure ($p_{ri_1}$). During this step, the additional gas entering the reference cell has no access to the sample, and therefore, pressure stabilization occurs when the temperature is equilibrated. Finally, valve 3 is opened and gas is allowed to travel from the reference cell to the sample cell. The stabilized pressure is recorded as the final pressure ($p_{f_1}$).

For the second stage, the stabilized pressure from the first stage is recorded as the initial sample cell pressure ($p_{f_1} = p_{si_2}$). Valve 3 is closed to isolate the sample cell and gas is allowed from the compressed gas cylinder into the reference cell. After pressure is stable, the initial reference cell pressure for the second stage is recorded ($p_{ri_2}$). Valve 3 is opened and the stabilized final pressure for the second stage is read ($p_{f_2}$). Subsequent stages proceed in a similar manner. When necessary, a syringe pump is used to increase the pressure beyond the one in the pressurized helium gas cylinder. At least two stages are necessary to calculate both porosity and compressibility, we performed a minimum of three stages for all cases.

**Calculations**

Porosity and compressibility were evaluated using three different approaches. The first approach ignores the changes in rock volume for small pressures increments, and resembles the recommended practices for core analysis published by API (1998). The second approach, accounts for the variation in rock volume as a function of pressure by means of introducing compressibility as a constant coefficient, a commonly used method. The third approach, will consider compressibility to be constant only within a certain pressure range. This option was introduced to check for the validity of the assumption of constant compressibility.

*Slightly compressible rock approach*

The moles of gas at initial conditions in the sample cell and in the reference cell are given by;

$$n_{si}=\frac{p_{si}\,(V_s - V_{gi})}{R\,Z_{si}T} \quad \text{……………} \quad 1$$

$$n_{ri}=\frac{p_{ri}V_r}{R\ Z_{ri}\ T} \quad \text{……………} \quad 2$$

Where ***n*** is moles of gas, ***p*** is the pressure, ***V*** is the volume, ***R*** is the gas constant, ***Z*** is the compressibility factor of helium, and ***T*** is the temperature. The subscripts ***s*** and ***r*** denote the volumes of the sample cell and the reference cell, whereas ***si*** and ***ri*** refer to the initial conditions in the sample and reference cell respectively. $V_{gi}$ denotes the volume of the rock grains at the pressure $p_{si}$ and the temperature ***T***.

Similarly, after the cells are communicated and the pressure has stabilized, the moles of gas in the reference and the sample cell are given by the following expressions, where the subscript ***f*** now denotes the final stabilized conditions.

$$n_{sf}=\frac{p_f\,(V_s - V_{gf})}{R\,Z_f\ T} \quad \text{……………} \quad 3$$

$$n_{rf}=\frac{p_fV_r}{R\ Z_fT} \quad \text{……………} \quad 4$$

The volume of rock grains or skeletal volume at the final equilibrium pressure is given in Eq. 3 by $V_{gf}$. Since the moles of gas contained in the system remain constant, we can establish the following relation;

$$n_{si}+n_{ri}=n_{sf}+n_{rf} \quad \text{……………} \quad 5$$

The volumes of both the sample cell (***$V_s$***) and the reference cell (***$V_r$***) considered in Eqs. 1 to 4 include the dead volumes in pipes and valves.

Substituting Eqs. 1 to 4 in Eq. 5, we obtain;

$$\frac{p_{si}\,(V_s\text{-}V_{gi})}{R\,Z_{si}T}+\frac{p_{ri}\,V_r}{R\,Z_{ri}T}=\frac{p_f\,(V_s\text{-}V_{gf})}{R\,Z_fT}+\frac{p_f\,V_r}{R\,Z_fT} \quad \ldots\ldots\ldots\ldots\ldots\ldots \quad 6$$

If we take small pressure increments, close to 100 psig, such that the final equilibrium pressure (***$p_f$*** ) is only slightly higher than the initial pressure in the sample cell (***$p_{si}$)***, and the compressibility of the rock is small enough, it can be assumed that the volume of the rock grains does not decrease considerably, making ***$V_g \approx V_{gi} \approx V_{gf}$***.

In Eq. 6, the temperature (***T***) can be dismissed as it is maintained constant throughout the experiment. Solving for the volume of the rock grains (***$V_g$***) we obtain;

$$V_g=\frac{\frac{p_f}{Z_f}[V_r+V_s]-\frac{p_{ri}\,V_r}{Z_{ri}}-\frac{p_{si}\,V_s}{Z_{si}}}{\left[\frac{p_f}{Z_f}-\frac{p_{si}}{Z_{si}}\right]} \quad \ldots\ldots\ldots\ldots\ldots\ldots \quad 7$$

Eq. 7 gives the volume of grains (***$V_g$***) as a function of pressure, all the pressures and volumes for such calculations are known, and the compressibility factors for helium (***$Z_{ri}$, $Z_{si}$*** and ***$Z_f$***) are calculated from an equation of state or an accurate correlation.

A plot of ***$V_g$*** as a function of ***$p_f$*** (or ***$p_{si}$***) is built and the volume of grain is extrapolated to the ***y*** axis to obtain the grain volume (***$V_{g0}$***) and the porosity at room pressure. The porosity can be calculated with knowledge of the bulk volume of the core plug.

*Constant rock compressibility approach*

Rearranging Eq. 6;

$$V_r\left[\frac{p_{ri}}{Z_{ri}}-\frac{p_f}{Z_f}\right]+V_s\left[\frac{p_{si}}{Z_{si}}-\frac{p_f}{Z_f}\right]=\frac{p_{si}\,V_{gi}}{Z_{si}}-\frac{p_f\,V_{gf}}{Z_f} \qquad \text{……} \qquad 8$$

The constant compressibility ***c*** of the rock grains is defined as;

$$c=-\frac{1}{V_{g0}}\left[\frac{V_g-V_{g0}}{p-p_0}\right] \qquad \text{……} \qquad 9$$

In Eq. 9, $p_0$ is a reference pressure and $V_{g0}$ is the volume of the rock grain at such pressure. For convenience, $p_0$ is taken as the room pressure, which is assumed to be zero-gauge pressure. Eq. 9 can be arranged to express the volume of rock grains $V_g$ at any pressure $p$ as a function of the compressibility **c** and the reference grain volume $V_{g0}$.

$$V_g=V_{g0}\,[1-p\,c] \qquad \text{……} \qquad 10$$

The volume of rock grains, at both the initial sample cell pressure ($p_{si}$) and the final stabilized pressure ($p_f$) can be written as a function of the volume of grains at the reference pressure or room pressure using Eq. 10.

$$V_{gi}=V_{g0}\,[1-p_{si}\,c] \qquad \text{……} \qquad 11$$

$$V_{gf}=V_{g0}\,[1-p_f\,c] \qquad \text{……} \qquad 12$$

Substituting Eq. 11 and Eq. 12 in Eq. 8,

$$V_r\left[\frac{p_{ri}}{Z_{ri}}-\frac{p_f}{Z_f}\right]+V_s\left[\frac{p_{si}}{Z_{si}}-\frac{p_f}{Z_f}\right]=V_{g0}\left[\frac{p_{si}}{Z_{si}}-\frac{p_f}{Z_f}\right]+V_{g0}\,c\left[\frac{p_f^2}{Z_f}-\frac{p_{si}^2}{Z_{si}}\right] \qquad \text{……} \qquad 13$$

Eq. 13 has two unknowns, the rock grain volume at room pressure ($V_{g0}$) and the rock compressibility ($c$). We can use pressure and z factors from any two stabilized stages to solve for both variables. For any two stages, one and two, Eq. 13 can be written as;

$$V_r\left[\frac{p_{ri_1}}{Z_{ri_1}}-\frac{p_{f_1}}{Z_{f_1}}\right]+V_s\left[\frac{p_{si_1}}{Z_{si_1}}-\frac{p_{f_1}}{Z_{f_1}}\right]=V_{g0}\left[\frac{p_{si_1}}{Z_{si_1}}-\frac{p_{f_1}}{Z_{f_1}}\right]+V_{g0}\,c\,\left[\frac{p_{f_1}^2}{Z_{f_1}}-\frac{p_{si_1}^2}{Z_{si_1}}\right] \quad \ldots\ldots\ldots\ldots\ldots\ldots\ldots\ldots\ldots\ldots \quad 14$$

$$V_r\left[\frac{p_{ri_2}}{Z_{ri_2}}-\frac{p_{f_2}}{Z_{f_2}}\right]+V_s\left[\frac{p_{si_2}}{Z_{si_2}}-\frac{p_{f_2}}{Z_{f_2}}\right]=V_{g0}\left[\frac{p_{si_2}}{Z_{si_2}}-\frac{p_{f_2}}{Z_{f_2}}\right]+V_{g0}\,c\,\left[\frac{p_{f_2}^2}{Z_{f_2}}-\frac{p_{si_2}^2}{Z_{si_2}}\right] \quad \ldots\ldots\ldots\ldots\ldots\ldots\ldots\ldots\ldots\ldots \quad 15$$

Where the new subscripts ***1*** and ***2*** denote the experimental stage. Eqs. 14 and 15 can be solved for $V_{g0}$;

$$V_{g0}=\frac{V_r\left[\frac{p_{ri_1}}{Z_{ri_1}}-\frac{p_{f_1}}{Z_{f_1}}\right]+V_s\left[\frac{p_{si_1}}{Z_{si_1}}-\frac{p_{f_1}}{Z_{f_1}}\right]}{\left[\frac{p_{si_1}}{Z_{si_1}}-\frac{p_{f_1}}{Z_{f_1}}\right]+c\,\left[\frac{p_{f_1}^2}{Z_{f_1}}-\frac{p_{si_1}^2}{Z_{si_1}}\right]} \quad \ldots\ldots\ldots\ldots\ldots\ldots\ldots\ldots\ldots\ldots\ldots\ldots\ldots\ldots\ldots\ldots \quad 16$$

$$V_{g0}=\frac{V_r\left[\frac{p_{ri_2}}{Z_{ri_2}}-\frac{p_{f_2}}{Z_{f_2}}\right]+V_s\left[\frac{p_{si_2}}{Z_{si_2}}-\frac{p_{f_2}}{Z_{f_2}}\right]}{\left[\frac{p_{si_2}}{Z_{si_2}}-\frac{p_{f_2}}{Z_{f_2}}\right]+c\,\left[\frac{p_{f_2}^2}{Z_{f_2}}-\frac{p_{si_2}^2}{Z_{si_2}}\right]} \quad \ldots\ldots\ldots\ldots\ldots\ldots\ldots\ldots\ldots\ldots\ldots\ldots\ldots\ldots\ldots\ldots \quad 17$$

Combining Eqs. 16 and 17, solving for the compressibility and making some variable changes, we obtain;

$$c=\frac{V_r\,[A_2\,B_1-A_1\,B_2]+V_s\,[B_2\,B_1-B_1\,B_2]}{V_r\,[A_1\,C_2-A_2\,C_1]+V_s\,[B_1\,C_2-B_2\,C_1]} \quad \ldots\ldots\ldots\ldots\ldots\ldots\ldots\ldots\ldots\ldots\ldots\ldots\ldots\ldots\ldots\ldots \quad 18$$

Where the coefficients ***A***, ***B*** and ***C*** are given by the following expressions, and the subscripts ***1*** and ***2*** denote the experimental stage;

$$A=\left[\frac{p_{ri}}{Z_{ri}}-\frac{p_f}{Z_f}\right] \quad \ldots\ldots\ldots\ldots\ldots\ldots\ldots\ldots\ldots\ldots\ldots\ldots\ldots\ldots\ldots\ldots\ldots\ldots\ldots\ldots \quad 19$$

$$B=\left[\frac{p_{si}}{Z_{si}}-\frac{p_f}{Z_f}\right] \quad \ldots\ldots\ldots\ldots\ldots\ldots\ldots\ldots\ldots\ldots\ldots\ldots\ldots\ldots\ldots\ldots\ldots\ldots\ldots\ldots \quad 20$$

$$C = \left[\frac{p_f^2}{Z_f} - \frac{p_{si}^2}{Z_{si}}\right] \qquad \text{..........} \qquad 21$$

With the pressures measured during the experiments (***$p_{si}$***, ***$p_{ri}$*** and ***$p_f$***) and the compressibility factors for helium (***$Z_{si}$***, ***$Z_{ri}$*** and ***$Z_f$***) obtained from an EOS or a correlation, ***A***, ***B*** and ***C*** can be calculated from Eqs. 19 to 21 and the compressibility ***c*** can be calculated from Eq. 18, we use the volume of the cells (***$V_s$***, ***$V_r$***) to calculate the grain or skeletal volume at room pressure (***$V_{g0}$***) from Eq. 16, or 17. With the bulk volume of the sample measured independently the porosity at room conditions can be obtained.

*Piecewise variable rock compressibility approach*

The compressibility defined in Eq. 9 implies that the volume of rock changes linearly as a function of pressure, from the room pressure to both, the initial sample cell pressure (***$p_{si}$***) and the final equilibrium pressure of any stage (***$p_f$***). Such pressures could be significantly higher than the room pressure.

To evaluate the behavior of compressibility as a function of pressure, we now consider the compressibility to be constant only between the initial sample pressure (***$p_{si}$***) and the final equilibrium pressure (***$p_f$***) in every stage. We start by re-writing Eq. 9 as follows;

$$c^* = -\frac{1}{V_{gf}}\left[\frac{V_{gi} - V_{gf}}{p_{si} - p_f}\right] \qquad \text{..........} \qquad 22$$

Note that the reference pressure is no longer the room pressure (***$p_0$***), and therefore there is no relation of the rock grain volumes, ***$V_{gi}$*** and ***$V_{gf}$***, at the experimental pressures ***$p_{si}$*** and ***$p_f$***, with the grain rock volume at room pressure (***$V_{g0}$***). We restrain ourselves from assuming that by studying the change in volume between the initial sample cell pressure, and the final stabilized pressure, we can gain any knowledge of the volume of grain rock at room conditions. We called this local compressibility ***c**** to differentiate it from the constant compressibility ***c*** we used previously.

Using Eq. 22 we arrive to the following expressions for $V_{gi}$ and $V_{gf}$;

$$V_{gi} = V_{gf}\left[1 - c^{*}\left(p_{si} - p_{f}\right)\right] \qquad \ldots\ldots 23$$

$$V_{gf} = \frac{V_{gi}}{\left[1 - c^{*}\left(p_{si} - p_{f}\right)\right]} \qquad \ldots\ldots 24$$

Substituting Eqs. 23 and 24 in Eq. 8 and solving for $V_{gf}$ and $V_{gi}$ respectively, we obtain;

$$V_{gf} = \frac{V_{r}\left[\frac{p_{ri}}{Z_{ri}} - \frac{p_{f}}{Z_{f}}\right] + V_{s}\left[\frac{p_{si}}{Z_{si}} - \frac{p_{f}}{Z_{f}}\right]}{\left[\frac{p_{si}}{Z_{si}} - \frac{p_{f}}{Z_{f}}\right] + c^{*}\left[\frac{p_{si}\,p_{f}}{Z_{si}} - \frac{p_{si}^{2}}{Z_{f}}\right]} \qquad \ldots\ldots 25$$

$$V_{gi} = \frac{V_{r}\left[\frac{p_{ri}}{Z_{ri}} - \frac{p_{f}}{Z_{f}}\right] + V_{s}\left[\frac{p_{si}}{Z_{si}} - \frac{p_{f}}{Z_{f}}\right]}{\left[\frac{p_{si}}{Z_{si}} - \frac{p_{f}}{Z_{f}\left[1 - c^{*}\left(p_{si} - p_{f}\right)\right]}\right]} \qquad \ldots\ldots 26$$

We consider two experimental stages, and write Eq. 25 for the first experimental stage, and Eq. 26 for the second.

$$V_{gf_{1}} = \frac{V_{r}\left[\frac{p_{ri_{1}}}{Z_{ri_{1}}} - \frac{p_{f_{1}}}{Z_{f_{1}}}\right] + V_{s}\left[\frac{p_{si_{1}}}{Z_{si_{1}}} - \frac{p_{f_{1}}}{Z_{f_{1}}}\right]}{\left[\frac{p_{si_{1}}}{Z_{si_{1}}} - \frac{p_{f_{1}}}{Z_{f_{1}}}\right] + c^{*}\left[\frac{p_{si_{1}}\,p_{f_{1}}}{Z_{si_{1}}} - \frac{p_{si_{1}}^{2}}{Z_{f_{1}}}\right]} \qquad \ldots\ldots 27$$

$$V_{gi_{2}} = \frac{V_{r}\left[\frac{p_{ri_{2}}}{Z_{ri_{2}}} - \frac{p_{f_{2}}}{Z_{f_{2}}}\right] + V_{s}\left[\frac{p_{si_{2}}}{Z_{si_{2}}} - \frac{p_{f_{2}}}{Z_{f_{2}}}\right]}{\left[\frac{p_{si_{2}}}{Z_{si_{2}}} - \frac{p_{f_{2}}}{Z_{f_{2}}\left[1 - c^{*}\left(p_{si_{2}} - p_{f_{2}}\right)\right]}\right]} \qquad \ldots\ldots 28$$

If the experimental stages are carried out consecutively, as suggested by our protocol, the volume of the rock grains at the end of the first stage ($V_{gf_1}$) will equal the volume of the gains at the beginning of the

second ($V_{gi_2}$). Imposing that condition, we combine expressions 26, 27 and 28 and arrive to the following equation;

$$\alpha c^{*2} + \beta c^{*} + \gamma = 0 \qquad \ldots\ldots 29$$

And the local compressibility ***c**** can be found by;

$$c^{*} = \frac{-\beta - \sqrt{\beta^2 - 4\alpha\gamma}}{2\alpha} \qquad \ldots\ldots 30$$

The constants $\alpha$, $\beta$ and $\gamma$ in Eq. 30 are given by;

$$\alpha = [V_r A_2 + V_s B_2]\, D_1 \left(p_{si_2} - p_{f_2}\right) \qquad \ldots\ldots 31$$

$$\beta = V_r \left[A_2 B_1 \left(p_{si_2} - p_{f_2}\right) - A_2 D_1 - A_1 E_2 \left(p_{si_2} - p_{f_2}\right)\right] + V_s \left[B_2 B_1 \left(p_{si_2} - p_{f_2}\right) - B_2 D_1 - B_1 E_2 \left(p_{si_2} - p_{f_2}\right)\right] \qquad \ldots\ldots 32$$

$$\gamma = V_r \left[A_1 B_2 - A_2 B_1\right] \qquad \ldots\ldots 33$$

***A***, ***B*** and ***C*** are defined by Eqs. 19, 20 and 21. The expressions for ***D*** and ***E*** follow, and the subscripts ***1*** and ***2*** denote the experimental stage.

$$D = \left[\frac{p_{si}\, p_f}{Z_{si}} - \frac{p_{si}^2}{Z_{si}}\right] \qquad \ldots\ldots 34$$

$$E = \frac{p_{si}}{Z_{si}} \qquad \ldots\ldots 35$$

Once the local compressibility (***c****) has been found, the volume of grains ($V_{gi}$, $V_{gf}$) at both the final equilibrium pressure ($p_f$) and the initial pressure of the sample cell ($p_{si}$) can be found. With knowledge of

the bulk volume of the core plug, the porosity can be estimated as a function of pressure. An extrapolation to room pressure is necessary to find the porosity at such conditions from this approach.

**Results and discussions**

Figure 16 shows the final grain volume ($V_{gf}$) as a function of the equilibrium pressure ($p_f$) of sample two for the three solutions proposed. Neglecting the compressibility results in an underestimation of the grain volume (Figure 16), and therefore in an overestimation of the pore volume. The grain volume and the compressibility calculated using the constant compressibility approach and the piecewise variable compressibility approach are similar, meaning the assumption of constant compressibility for the range of pressures used in this investigation is valid.

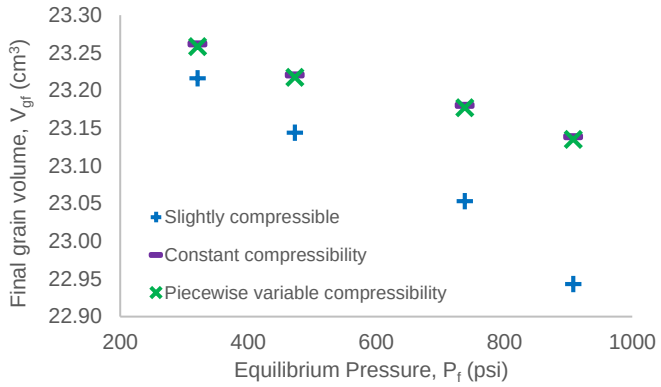


Figure 16 – Final grain volume as a function of equilibrium pressure for sample number two.

A decrease in the magnitude of the compressibility as a function of pressure was reported by Santos and Akkutlu (2013) at higher pressures than those employed in this research, prompting us to explore this possibility. We will continue to use the constant compressibility model in our subsequent measurements to

observe the behavior of the rock compressibility. The results for porosity and compressibility using our second approach, with a constant compressibility coefficient, are presented in Table 10.

| Sample | Grain volume, $V_{g0}$ ($cm^3$) | Porosity (%) | Compressibility, c (1/psi) |
|---|---|---|---|
| 1 | 18.60 | 10.30 | $8.16x10^{-6}$ |
| 2 | 23.34 | 8.22 | $9.89x10^{-6}$ |
| 3 | 21.57 | 5.94 | $6.44x10^{-6}$ |
| 4 | 18.23 | 6.44 | $4.50x10^{-6}$ |
| 5 | 17.36 | 10.12 | $8.73x10^{-6}$ |
| 6 | 17.28 | 8.10 | $5.32x10^{-6}$ |
| 7 | 17.49 | 7.89 | $2.23x10^{-6}$ |
| 8 | 17.98 | 8.65 | $2.14x10^{-5}$ |
| 9 | 17.52 | 7.35 | $9.18x10^{-6}$ |
| 10 | 18.07 | 7.37 | $2.19x10^{-5}$ |
| 11 | 17.61 | 7.17 | $1.07x10^{-5}$ |

Table 10 – Porosity and compressibility for the Wolfcamp core samples.

The porosity ranges from 5.94% to 10.30%. Samples from the same well taken from similar depths present significant variation in porosity. These results highlight the importance of measuring the porosity of core plugs as opposed to the use of crushed rock material. The rock porosity is comprised of several contributors because significant heterogeneity can be found even at the core scale in shale reservoirs. Figure 17 shows computerized tomography scan (CT scan) images from the three samples from Well 1. The figure shows a cross section of each core selected to highlight the major heterogeneities. The scale to the left of Figure 17 is in terms of CT number or Hounsfield unit. CT number is directly correlated to the density and the composition of the material, higher CT number implies a higher density. For instance, CT number for air is -1,000 HU, and 0 HU for water.

The images were captured using a medical CT scanner with a spatial resolution of 350 microns, therefore, the heterogeneities of the core at a smaller scale cannot be observed. It is evident that sample 1 is much more heterogeneous than samples 2 and 3. Sample 1 shows horizons of different density that are compatible with bedding planes, two of horizons, colored red and black, could potentially be fractures. Sample 2 is a lot more homogeneous, showing only one horizontal feature of lower density, whereas sample 3 does not show any.

Note also that CT numbers in samples two and three are higher than in sample one. All these observations agree with the porosity results shown it Table 10.

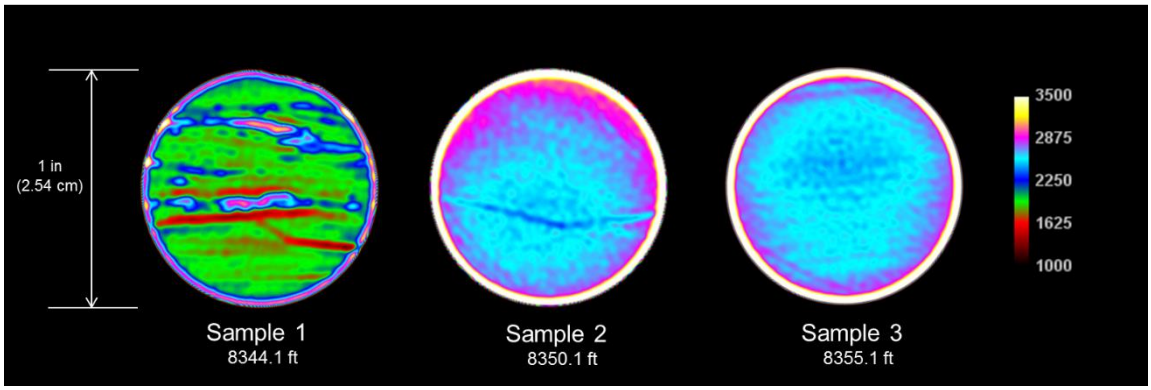


Figure 17 – Computerized tomography scan images of the samples from Well 1. The images correspond to a cross section of the core plug. The scale shown is in terms of CT number or Hounsfield units, which is directly related to the density of the material

The use of core plug samples for porosity measurement is more time consuming than the traditional method of using crushed rock samples. On the other hand, the features shown in Figure 17 are likely to be lost by crushing the rock, and their contribution to the porosity of the core plug sample will not be captured leading to a false perception of homogeneity among samples. Note that even after crushing, these samples will still have different porosities because they have different densities suggesting the rock matrix changes from one to another, however, as we will show later, core plug porosity and crushed porosity can differ significantly. There is no consistency among experimenters regarding the size of the crushed rock particles in porosity and adsorption measurement. Chalmers and Bustin (2007) and Chareonsuppanimit et al. (2012) reported particle size of 250 μm, Weniger et al. (2010) mentioned less than 2 mm, whereas Heller and Zoback (2014) did between 50 and 150 μm, as a few examples.

SORPTION CAPACITY AND TOTAL STORAGE

We measure $CO_2$ sorption using the same equipment we described for porosity measurement. The outcome of our experiment is the total amount of gas in the sample cell, sorbed and free. Then, by using the measured porosity and compressibility of the shale sample using helium, a weakly adsorbent gas, we determine the volume available for free gas storage, or bulk gas volume. Subtracting this from the total, we obtain the excess sorption or Gibbs surface excess quantity. We approximate the volume of the sorbed layer and correct the bulk free gas volume to obtain absolute sorption. Following in the sections below, we present the experimental procedure, the calculations, and the results.

**Experimental procedure**

For the sorption measurements, the protocol is similar to the one described for the porosity and compressibility measurements. Sorption was measured using $CO_2$ and the experiments were performed at the reservoir temperature of 165 ˚F. Two experimental stages are necessary, we performed at least three stages.

**Calculations**

The number of moles in the reference cell will remain as defined by Eqs. 2 and 4 at the initial reference cell pressure ($\boldsymbol{p_{ri}}$) and the final stabilized pressure ($\boldsymbol{p_f}$), respectively. In the sample cell, the gas will be stored in the void volume of the cell and the pore volume of the rock sample, but additionally, we consider that gas can be stored via sorption on the organic component of the rock sample.

We selected a Langmuir isotherm (Langmuir 1917) to model the moles of gas sorbed ($\boldsymbol{n_{si\text{-}s}}$) in the sample at initial conditions ($\boldsymbol{p_{si}}$). The Langmuir isotherm has been successfully applied before to model $CO_2$, nitrogen and methane sorption (Nuttall et al. 2005, Chalmers and Bustin 2008, Heller and Zoback 2014) and its use

has been also supported by sorbed gas density profiles in mesopores computed by molecular modeling and simulation (Ambrose et al. 2012).

$$n_{si\text{-}s} = n_{s\text{-}s\ max} \frac{p_{si}}{p_{si} + p_L} \qquad \ldots\ldots \qquad 36$$

Where $n_{s\text{-}s\ max}$ is the maximum amount of gas in moles that can be sorbed in the sample, and $p_L$ is the Langmuir pressure. In a similar manner, the moles of gas sorbed in the sample ($n_{sf\text{-}s}$) at the final stabilized pressure conditions ($p_f$) are written;

$$n_{sf\text{-}s} = n_{s\text{-}s\ max} \frac{p_f}{p_f + p_L} \qquad \ldots\ldots \qquad 37$$

The moles of free gas inside the cell and the pore space within the sample ($n_{si\text{-}f}$, $n_{sf\text{-}f}$) can be expressed using the real gas law as previously, both at the initial sample cell pressure ($p_{si}$) and the stabilized final pressure for the stage ($p_f$);

$$n_{si\text{-}f} = \frac{p_{si}\ V_{si\text{-}f}}{Z_{si}\ R\ T} \qquad \ldots\ldots \qquad 38$$

$$n_{sf\text{-}f} = \frac{p_f\ V_{sf\text{-}f}}{Z_f\ R\ T} \qquad \ldots\ldots \qquad 39$$

The terms $V_{si\text{-}f}$, and $V_{sf\text{-}f}$ in Eqs. 38 and 39 refer to the volume available to store gas in a free state in the sample cell at its initial pressure ($p_{si}$) and the final stabilized pressure ($p_f$). They are defined by;

$$V_{si\text{-}f} = V_s - V_{gi} - V_{ads\ i} \qquad \ldots\ldots \qquad 40$$

$$V_{sf\text{-}f} = V_s - V_{gf} - V_{ads\ f} \qquad \ldots\ldots \qquad 41$$

Where $V_s$ is the volume of the sample cell, $V_{gi}$ is the volume occupied by the grains of the rock sample at the initial sample cell pressure ($p_{si}$), $V_{gf}$ is its equivalent at final stabilized pressure ($p_f$). $V_{ads\,i}$, and $V_{ads\,f}$ are the volumes occupied by the layer of sorbate on the surface of the rock grains at initial sample cell pressure and final stabilized pressure, respectively.

The reasoning behind the incorporation of the volume of the sorbed phase ($V_{ads\,i}$, $V_{ads\,f}$) in Eqs. 40 and 41 is depicted in Figure 18. The grain volume ($V_{gi}$, $V_{gf}$) in Eqs. 40 and 41 have been measured previously with helium during our porosity and compressibility experiments. However, when the sample cell is saturated with $CO_2$, or other adsorbent gas, the molecules stored in a sorbed state conform a layer that occupies a volume, this volume is certainly small, but in micro and mesoporous materials is a relevant fraction of the pore volume that remains available for free gas storage. If this volume is not deducted, the volume available for free gas is overestimated.

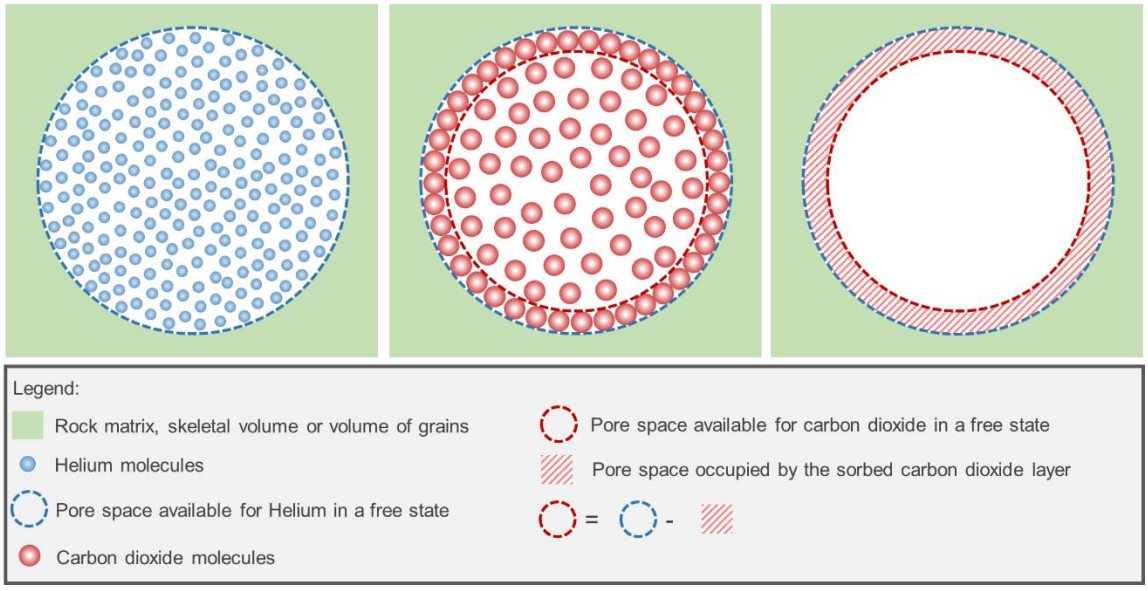


Figure 18 – Schematic representation of the relation among the pore space available for free helium, the pore space occupied by the layer of sorbed carbon dioxide, and the pore space available for free carbon dioxide.

The volume of the adsorbed phase (***V**_**ads**_*) can be written also in terms of a Langmuir isotherm (Santos and Akkutlu 2013, Ambrose et al. 2012);

$$V_{ads} = V_{ads\ max}\ \frac{p}{p + p_L} \qquad \text{……………} \quad 42$$

Where $V_{ads\ max}$ is the volume occupied by the maximum amount of gas that could be sorbed by the rock, $p$ refers to the pressure of interest and $p_L$ is the Langmuir pressure. Now, we define the density of the sorbed phase ($\rho_s$);

$$\rho_s = \frac{m_{ads\ max}}{V_{ads\ max}} = \frac{n_{s\text{-}s\ max}\ M}{V_{ads\ max}} \qquad \text{……………} \quad 43$$

The density of the sorbed phase ($\rho_s$) in Eq. 43 is expressed in terms of the mass of the sorbed phase ($m_{ads\ max}$) and its volume ($V_{ads\ max}$). The mass can be conveniently written as the product of the maximum amount of gas in moles the rock can sorb ($n_{s\text{-}s\ max}$) times the molecular weight of the gas ($M$).

Substituting Eq. 43 in Eq. 42, we obtain an expression for the volume of the sorbed phase at the conditions of interest;

$$V_{ads\ i} = \frac{n_{s\text{-}s\ max} M}{\rho_s}\left[\frac{p_{si}}{p_{si} + p_L}\right] \qquad \text{……………} \quad 44$$

$$V_{ads\ f} = \frac{n_{s\text{-}s\ max} M}{\rho_s}\left[\frac{p_f}{p_f + p_L}\right] \qquad \text{……………} \quad 45$$

The approximation of the density of the sorbed phase ($\rho_s$) is an intricate matter and it will be addressed later. Eqs. 37 and 39 can be added to obtain an expression for moles of gas in the sample cell at the final equilibrium pressure ($p_f$).

$$n_{sf} = n_{sf\text{-}s} + n_{sf\text{-}f} = n_{s\text{-}s\,max}\frac{p_f}{p_f + p_L} + n_{sf\text{-}f} = \frac{p_f\,V_{sf\text{-}f}}{Z_f\,R\,T} \qquad \cdots\cdots\cdots\cdots \qquad 46$$

Substituting Eqs. 41 and 45,

$$n_{sf} = n_{s\text{-}s\,max}\frac{p_f}{p_f + p_L} + \frac{p_f\left(V_s - V_{gf}\right)}{Z_f\,R\,T} - \frac{p_f}{Z_f\,R\,T}\,\frac{n_{s\text{-}s\,max}\,M}{\rho_s}\left[\frac{p_f}{p_f + p_L}\right] \qquad \cdots\cdots\cdots\cdots \qquad 47$$

Rearranging;

$$\frac{n_{sf} - \dfrac{p_f}{Z_f\,R\,T}\left[V_s - V_{gf}\right]}{1 - \dfrac{M}{\rho_s}\dfrac{p_f}{Z_f\,RT}} = n_{s\text{-}s\,max}\left[\frac{p_f}{p_f + p_L}\right] \qquad \cdots\cdots\cdots\cdots \qquad 48$$

By observation of Eqs. 37 and 48, the moles of sorbed gas in the rock sample at each equilibrium pressure are;

$$n_{sf\text{-}s} = \frac{n_{sf} - \dfrac{p_f}{Z_f\,R\,T}\left[V_s - V_{gf}\right]}{1 - \dfrac{M}{\rho_s}\dfrac{p_f}{Z_f\,R\,T}} \qquad \cdots\cdots\cdots\cdots \qquad 49$$

The calculation of the total moles in the sample cell at each final equilibrium pressure (***$n_{sf}$***) required in Eq. 49 can be obtained from Eq. 50;

$$n_{sf} = n_{ri} + n_{si} - n_{rf} \qquad \cdots\cdots\cdots\cdots \qquad 50$$

Solving this equation for the moles in the sample cell at each final equilibrium pressure (***$n_{sf}$***), and separating the moles of gas initially in the sample cell (***$n_{si}$***) in the free (***$n_{si\text{-}f}$***) and sorbed (***$n_{si\text{-}s}$***) components we get;

$$n_{sf} = n_{ri} + \left(n_{si\text{-}s} + n_{si\text{-}f}\right) - n_{rf} \qquad \cdots\cdots\cdots\cdots \qquad 51$$

All the elements in Eq. 51 have been defined earlier in Eqs. 2, 36, 38 and 4. For the density of the sorbed phase, we will use the approach of Dubinin (1960) based on the ***b*** constant of the Van Der Walls equation of state. For $CO_2$, the density of the adsorbed phase ($\rho_s$) equals 1.03 g/cm$^3$.

Finally, Eq. 37 can be arranged in the form proposed by Mavor, Owen, and Pratt (1990) as suggested by Santos and Akkutlu (2013), taking advantage of the possibility of expressing the adsorption isotherm as a straight line;

$$\frac{1}{n_{sf\text{-}s}} = \left[\frac{p_L}{n_{s\text{-}s\ max}}\right]\frac{1}{p_f} + \frac{1}{n_{s\text{-}s\ max}} \quad \ldots\ldots\ldots\ldots\ldots\ldots\ldots\ldots\ldots\ldots\ldots\ldots \quad 52$$

Eq. 52 shows that a plot of $1/n_{sf\text{-}s}$ as a function of $1/p_f$ will have a slope equal to $p_L/n_{s\text{-}s\ max}$ and an intercept of $1/n_{s\text{-}s\ max}$. We estimate the adsorption parameters, $n_{sf\text{-}s}$ and $p_L$ in Eq. 52 by regressing to fit the experimental data. The moles of gas sorbed ($n_{sf\text{-}s}$) can be converted to the more traditional Langmuir volume ($G_{SL}$) using again the definition of density;

$$G_{SL}=\frac{n_{sf\text{-}s}\ M}{\rho_{SC}\ w} \quad \ldots\ldots\ldots\ldots\ldots\ldots\ldots\ldots\ldots\ldots\ldots\ldots \quad 53$$

In Eq. 53 $w$ is the mass of the shale sample and $\rho_{SC}$ is the density of the sorbed gas at standard conditions.

## Results and discussions

The experimental data was regressed using the Mavor straight line representation (Mavor, Owen, and Pratt 1990) of the Langmuir sorption model (Langmuir 1917), as presented in Eq. 52. The sorption isotherms are illustrated in Figure 19 and the Langmuir volume and pressure resulting from the regression process are shown in Table 11. We obtained a good match of all the experimental data resulting in coefficients of determination close to 1. Sample 2 presented the minimum sorption capacity with a Langmuir volume of

38.77 scf/ton, whereas the maximum sorption capacity is observed for sample 1 with a Langmuir volume of 154.41 scf/ton.

| Sample | Langmuir Volume, $G_{SL}$ (scf/ton) | Langmuir Pressure, $P_L$ (psig) | $R^2$ |
|---|---|---|---|
| 1 | 154.41 | 1,381.24 | 1.00 |
| 2 | 38.77 | 512.59 | 0.98 |
| 3 | 41.06 | 669.86 | 1.00 |
| 4 | 64.37 | 1,332.16 | 0.91 |
| 5 | 65.58 | 2,444.83 | 1.00 |
| 6 | 133.51 | 1,384.52 | 1.00 |
| 7 | 87.59 | 1,899.41 | 0.99 |
| 8 | 129.90 | 952.30 | 1.00 |
| 9 | 87.04 | 1,368.98 | 1.00 |
| 10 | 42.12 | 1,298.84 | 0.94 |
| 11 | 71.94 | 1,206.49 | 0.99 |

Table 11 – Langmuir sorption parameters for the Wolfcamp core plugs.

The sorption results are consistent with the porosity and the CT scanner images. Sorption occurs in the organic fraction of the rock matrix, and the sorption capacity mainly depends on the amount of organic matter, its maturity, and the type of macerals (Chalmers and Bustin 2008).

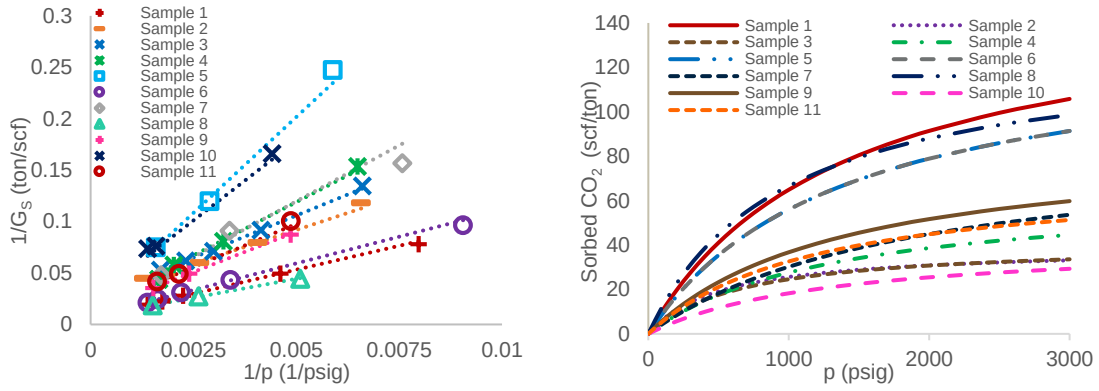


Figure 19 – Sorption isotherms. Left: experimental data fit using the straight line approach. Right: traditional representation of the Langmuir model

Several authors have found gas sorption capacity to grow linearly as TOC of the rock increases (Nuttall et al. 2005, Chalmers and Bustin 2007, 2008, Ross and Bustin 2009, Weniger et al. 2010, Chareonsuppanimit et al. 2012). We observed a similar trend in our samples (Figure 20). The sorption capacity of our organic rich shale core plugs decreased linearly with CT-number. This is because CT-number is widely controlled by the density, and organic matter content has been suggested to be the main reason for the variations in shale density (Schmoker 1979).

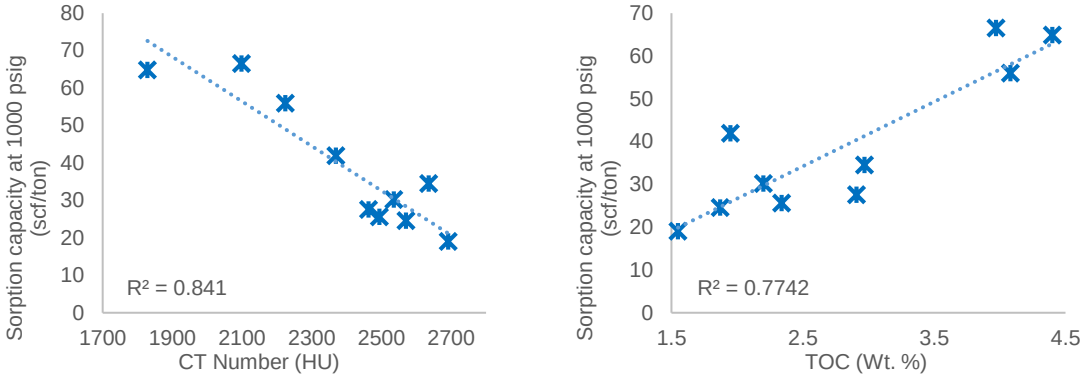


Figure 20 – Sorption capacity at 1,000 psig as a function of CT number and TOC. Note the linear relationship in both cases.

Additionally, higher porosity has been correlated to high TOC in literature, because the organic matter is rich in micro and mesopores (Chalmers and Bustin 2007, 2008, Kang et al. 2011). We observed this behavior in our organic rich shale core samples (Figure 21). The relation between porosity and CT-number has been previously documented for conventional reservoirs within our research group (Skinner, Tovar, and Schechter 2015). In this investigation, we extend this relationship to unconventional tight shale cores. We found porosity to decrease linearly with CT-number for the organic shale core plugs under investigation (Figure 21). The CT-number is dependent on the bulk rock density, which can be obtained from a volume weighted average of the rock grains density, and the density of the gas occupying the empty spaces between

such grains. Making CT-number a function of porosity. In the case of organic rich shale the rock grain density is also dependent on the TOC.

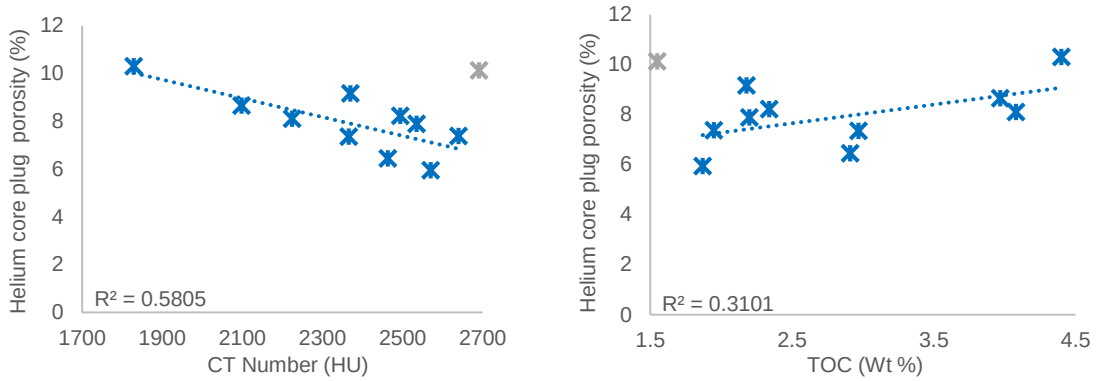


Figure 21 – Helium core plug porosity as a function of CT-number and TOC. Note the linear relations in both cases. The outlier corresponds to sample 5.

The helium porosity measured in the core plugs correlates better to CT-number than to TOC in large part because the first, captures the empty space within the sample, including all pores, fractures, and micro-fractures; whereas the latter only captures the porosity associated to the organic matter. Note that in Figure 21 there is a point that has been greyed out. Such point corresponds to sample 5, and it was not considered for the correlations. We have three reasons for this. The first, is that sample 5 contained a particularly large fracture that significantly contributed to its porosity (10.12%, Table 10). The fracture should have been captured by the CT-scanner correlation, but not by the TOC one. The second reason is the complexity of the sample, the core plug was taken in a bedding plane and it is possible to observe three well defined rock types, with different densities, and therefore, different CT-numbers ( Figure 22). We do not know exactly what the consequence of this can be in our measurements, but in our experience measuring rock properties for conventional and unconventional reservoirs, we have obtained unreliable measurements in very heterogeneous samples. The third reason is that one of the regions in sample 5 has a particularly high CT-number that increased the average CT-number of the sample.

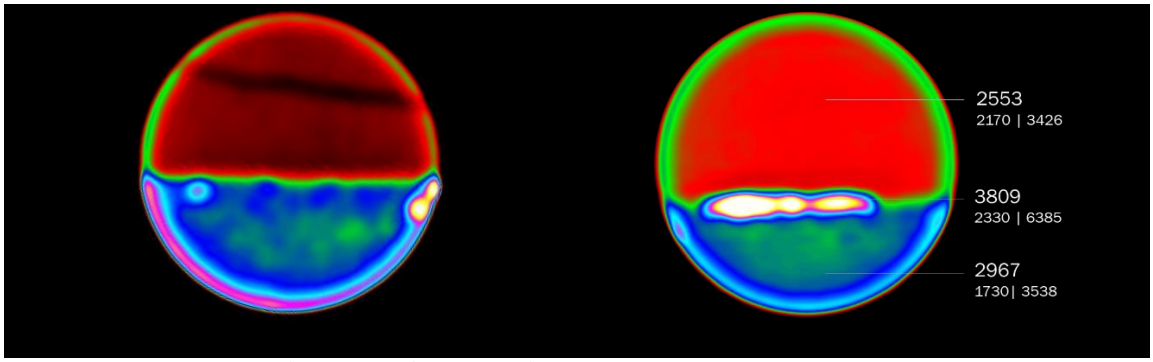

Figure 22 – CT-scanner image of sample 5. Left: shows the fracture in the sample in black. Right: shows the three rock types within the sample and the lowest, the highest and the average CT-number for each region.

From Figure 20 and Figure 21, we could have anticipated the linear relation between CT-number and TOC showed in Figure 23. This relation is based on the control that the amount of organic matter exerts over the rock density, which governs the CT-number. The three relationships we have shown between CT-number and porosity, sorption capacity, and TOC are relevant because the CT-number of the shale samples can be measured in minutes without destroying the core plugs, or invading them with any fluids that could alter them. Therefore, once the porosity, sorption capacity, and TOC of a few samples are measured in the laboratory and satisfactory relations of those three parameters have been established with the CT-number, we can estimate those three parameters in additional samples in minutes, without altering them, by measuring their CT-number. This is a major step forward from current practices. The laboratory measurement of porosity and adsorption requires several weeks when it is done in core plugs. If the samples are crushed, the measuring time can be reduced, but at the expense of the destruction of the rock sample. Similarly, measuring TOC requires the sample to be destroyed. This is a positive finding for the characterization of organic rich shale plays, and provides for additional, faster tools to measure porosity, sorption or TOC which are often needed as input of other laboratory procedures.

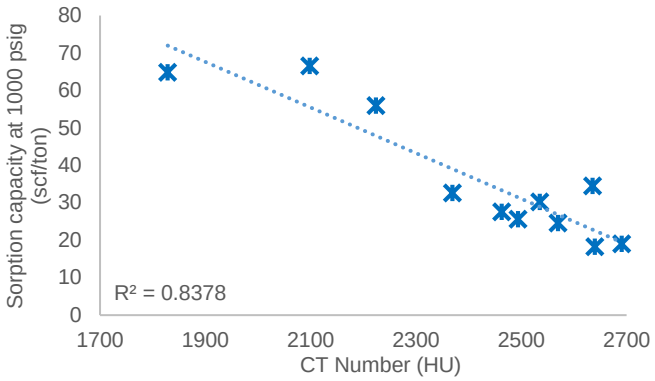


Figure 23 – TOC as a function of CT-number. Note the linear relation.

Most of the $CO_2$ in the samples tested is stored in a free state within the porous space (Figure 24). At low pressures, sorption constitutes an important storage mechanism. At about 100 psig the fraction of $CO_2$ stored via sorption ranges from 25% to 62% of the total. Even though the volume of gas stored in a sorbed state increases with pressure, its relative contribution to the total storage capacity of the rock decreases. This is a consequence of the much faster increase with pressure of the gas stored in the free space, driven by the high gas compressibility. At 1,000 psig, sorption still accounts for between 17% to 41% of the $CO_2$ storage capacity of all samples. But at 2,500 psig, however, the total $CO_2$ storage capacity ranged between 296 and 602 scf/ton, of which only 6% to 20% is in a sorbed state. The relative contribution of these storage mechanisms is relevant in both carbon sequestration and $CO_2$ EOR. A higher percentage of $CO_2$ stored in a sorbed state is attractive for carbon sequestration, whereas for EOR purposes it is not. This is because the volume of $CO_2$ sorbed takes longer to be recovered during the depletion of the reservoir pressure than the amount stored free in the porous space. The application of $CO_2$ EOR in shale oil reservoirs is currently conceptualized most commonly as a huff and puff process due to the lack of connectivity and the presence of natural fractures in such rocks. The lack of connectivity prohibits the continuous flow of $CO_2$ from injector to producer wells, whereas the presence of a well-developed fracture network will enable connectivity but will cause $CO_2$ cycling. In a huff and puff scheme, the $CO_2$ that is sorbed during the injection stage may not be completely recovered during the depletion stage, raising $CO_2$ utilization.

Utilization is the volume at standard conditions of $CO_2$ required to produce a stock tank barrel of oil, and it is a main player in the economics of a $CO_2$ EOR project. In a hypothetic continuous injection case, the pressure will be kept nearly constant and the sorbed $CO_2$ would remain trapped.

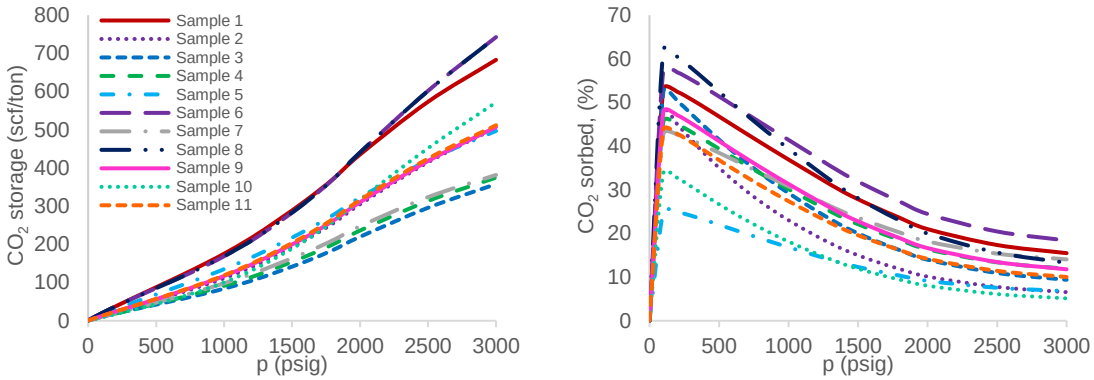


Figure 24 – Left: total (free + sorbed) $CO_2$ storage as a function of pressure. Right: percentage of the total $CO_2$ storage in a sorbed state

The change of the rock volume as a function of pressure is incorporated in our final expression for sorption, Eq. 52, through the moles of gas present in the sample cell at each equilibrium pressure $\boldsymbol{p_f}$ in a sorbed state ($\boldsymbol{n_{sf\text{-}s}}$), defined by Eq. 49, which requires the volume of the grains of rock matrix at each equilibrium pressure ($\boldsymbol{V_{gf}}$). The volume of the rock matrix can be calculated at any pressure with knowledge of a reference volume of rock matrix, the pressure at which such volume was measured, and the compressibility of the rock. This can be accomplished using our second approach for porosity and compressibility, which considers constant compressibility, using Eq. 10. And in our third approach, with variable rock compressibility using Eq. 24. Ignoring the decrease in the volume of rock matrix with increasing pressure results in the overestimation of the sorption capacity of the rock (Figure 25). While the rock skeletal volume decreases, more volume for free gas storage is made available inside the sample cell. If this newly created space is not accounted for, the gas stored in it will not be deducted from the sorbed gas. This overestimation of gas sorption is bigger

in the low sorption capacity rocks and increases with pressure because of the effect of the compressibility of the free gas.

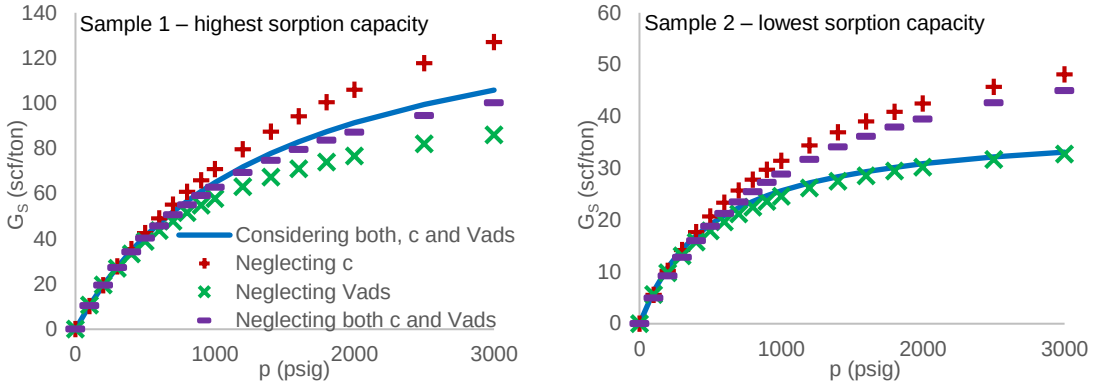


Figure 25 – Effect of neglecting the volume of the sorbed phase and the compressibility in sorption calculations

The molecules of gas adsorbed on the rock matrix occupy a volume. The $CO_2$ molecule has an ellipsoidal shape with a length of 0.54 nm and a kinetic diameter of 0.34 nm (Roque-Malherbe et al. 2011, Balmaseda et al. 2003), the kinetic diameter of methane is 0.3817 nm and the one nitrogen is 0.3698 nm (Vermesse, Vidal, and Malbrunot 1996). Even when these molecules are extremely small, they occupy a relevant space in the reduced volume inside the micropores found in the organic matter of shale reservoir rock. Since an important fraction of the porosity in such rocks can be comprised of micropores and mesopores, neglecting the volume of the sorbed layer leads to an overestimation of the pore space available for free gas storage. We illustrated in Figure 18 the reasoning behind the inclusion of the term $\boldsymbol{V_{ads}}$ to account for the volume of the sorbed layer in Eqs. 40 and 41. When the term is omitted (Figure 25), the volume occupied by the sorbed layer is erroneously considered to be available to store free gas, leading to an overestimation of the amount of free gas within the sample cell and consequently to the underestimation of the sorption capacity of the rock. This problem becomes more serious for rocks with high sorption capacity. Note also that since the effects of neglecting the rock compressibility and the volume of the adsorbed layer weight in opposite

directions, ignoring both of them results in a closer estimation of sorption than ignoring either one of them for sample 1. For the case of sample 2, since the adsorption capacity is low, neglecting compressibility can lead to considerable error, whereas neglecting the volume of the adsorbed layer does not affect the outcome significantly.

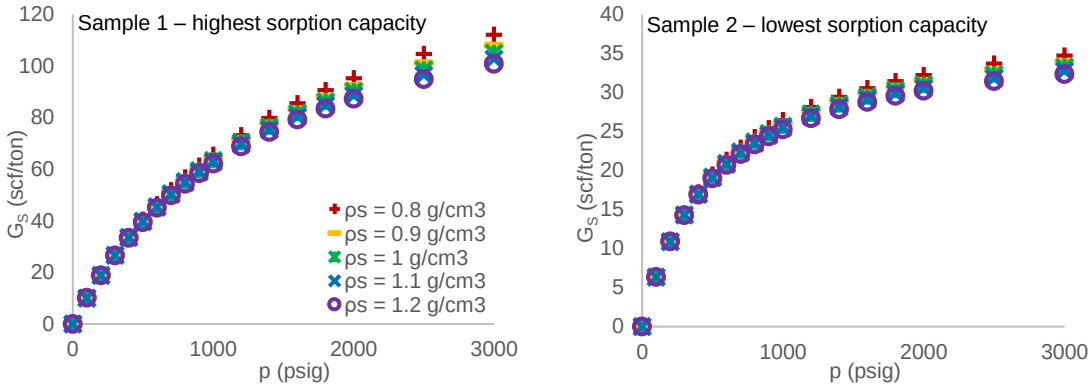


Figure 26 – Effect of the magnitude of the density of the sorbed phase in the sorption capacity calculation

We related the maximum volume of the sorbed layer ($\boldsymbol{V_{ads\ max}}$) to the density of the sorbed phase ($\boldsymbol{\rho_s}$) in Eq. 43. The latter is not, however, a trivial magnitude to measure. Molecular modeling and simulation, and real canonical ensemble are techniques that have been used to estimate it (Ambrose et al. 2012). It has also been found that the density of the sorbed phase is a function of temperature, pressure and pore size (Weniger et al. 2010, Ming et al. 2003, Ambrose et al. 2012). The employment of molecular modeling and simulation demands a specialized set of resources and skills. A simpler approach was proposed by Dubinin (1960) using the ***b*** constant of the Van der Walls cubic equation of state, which accounts for the volume of the molecules in PVT calculations. Using that approximation, we estimated a value of 1.03 g/cm$^3$ for $CO_2$. Another method, proposed by Humayun and Tomasko (2000) consists in extrapolating the linear region in a plot of excess gas adsorption as a function of gas density using high pressure adsorption data. Using that method, Sudibandriyo et al. (2003) estimated the density of the sorbed phase of $CO_2$ on activated carbon in

1.02 g/cm$^3$, and Chareonsuppanimit et al. (2012) estimated the density of the sorbed phase of $CO_2$ on five shale samples from the data reported by Weniger et al. (2010) to be between 0.79 and 1.08 g/cm$^3$.

To realize the impact of the uncertainty related to the density of the sorbed phase determination, we calculated sorption for samples one and two using a range for the density of the sorbed layer of $CO_2$ from 0.8 to 1.2 gr/cm$^3$, and we present the results in Figure 26. Small variations in the density of the sorbed layer of gas has a limited impact in the determination of the sorption capacity in our samples. This is particularly true for samples with low sorption capacity. For samples of this nature, the use of sophisticated methods to determine the density of the sorbed layer of $CO_2$ may not be justified, keeping also in mind that such methods also come with limitations, and they are also an approximation. Uncertainties in the determination of the compressibility had a bigger impact than the density of the sorbed layer in the determination of the sorbed capacity of our samples. The effect is more pronounced for our low sorption capacity case (Figure 27).

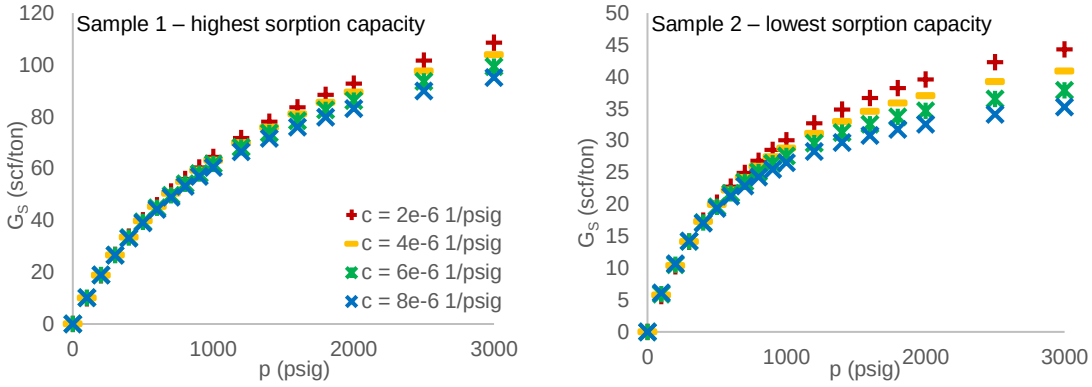


Figure 27 – Effect of the magnitude of the compressibility of the rock in the sorption capacity calculation

The use of Helium to measure porosity and compressibility introduces another source of error in the calculation of the sorption capacity. The kinetic diameter of the helium molecule is 0.2556 nm (Vermesse, Vidal, and Malbrunot 1996), which is smaller than the kinetic diameter of $CO_2$, nitrogen and methane. Thus,

in samples with significant microporosity, the volume available for free or bulk gas calculated with helium is larger than the one that $CO_2$, methane, nitrogen, or other sorbent gases with larger molecular kinetic diameter could access. This overestimation in the volume available for free gas will result in an underestimation of the volume of sorbed gas. The extent of this deviation depends on the prevalence of microporosity in the sample and therefore it is difficult to quantify without knowledge of the pore size distribution. Calculations using the same sorbent gas to determine porosity of the sample imply the use of the sorption data to regress not only the Langmuir parameters but also for porosity and compressibility. Kang et al. (2011) used this approach with samples from the Barnett shale. However the nonlinear regression of multiple parameters can lead to non-unique solutions which later was pointed out by Santos and Akkutlu (2013).

## MINERAL CHARACTERIZATION

The mineral composition of our organic rich shale samples was obtained by X-ray diffraction (XRD) analysis and is presented in Figure 28. XRD was performed after the samples were used for the experiments introduced in the following chapters. The core samples were finely grinded, but not sieved, to preserve the proportions of the different minerals. For both wells, 1 and 2, the predominant minerals are quartz, and calcite. Every sample is composed of at least 40% of one of these two minerals. Muscovite is the third most predominant mineral, followed by dolomite and siderite, which was found in only two samples consisting of less than 1 % of the composition.

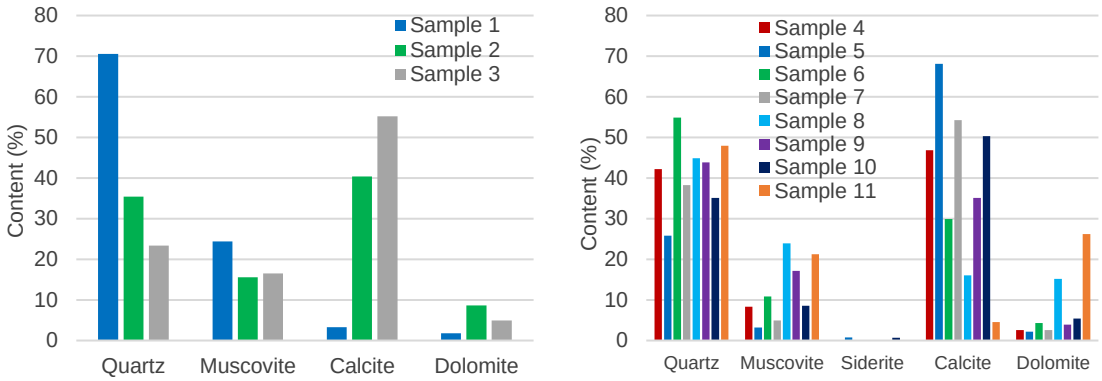


Figure 28 – Mineral composition of the organic shale core samples used in this investigation. Left: samples from well 1. Right: samples from well 2. Note that the main components in both cases are quartz and calcite.

Out of the 11 samples, five of them are predominately composed by silicates (Figure 29), four by carbonates, and two have almost equal proportions of silicates and carbonates. This highlights the important differences in mineral composition within the Wolfcamp formation. In both wells, we found samples in each one of those three groups, even when the core plugs were obtained from adjacent depths. This further supports the differences in porosity, and CT-number, presented in Figure 17.

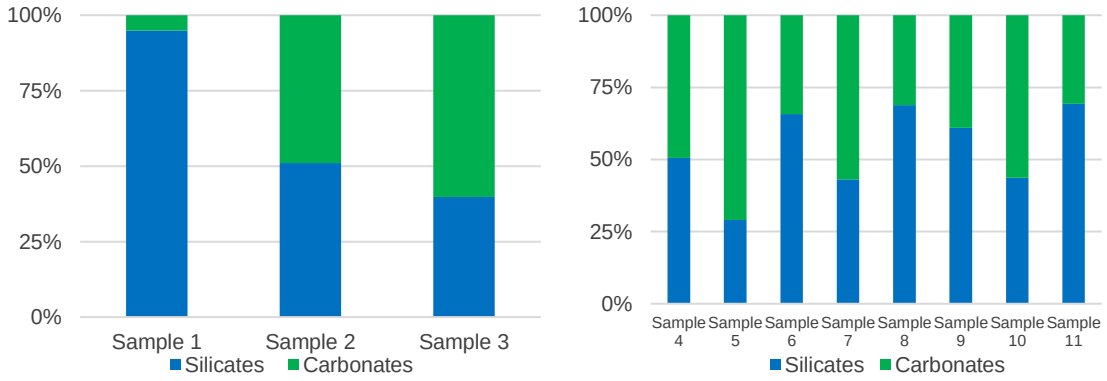


Figure 29 – Proportion of silicates and carbonates in the samples used in this investigation. Left: samples from well 1. Right: samples from well 2.

We pointed out earlier, with the help of Figure 22, that sample 5 had three definite regions that were different rock types. The differences between the two major regions were obvious even from simple observation of the core plugs. One section of the core was lighter in color than the other. We separated those parts and obtained the mineral composition for each one of them (Figure 30). The lighter region was richer in calcite than the darker portion.

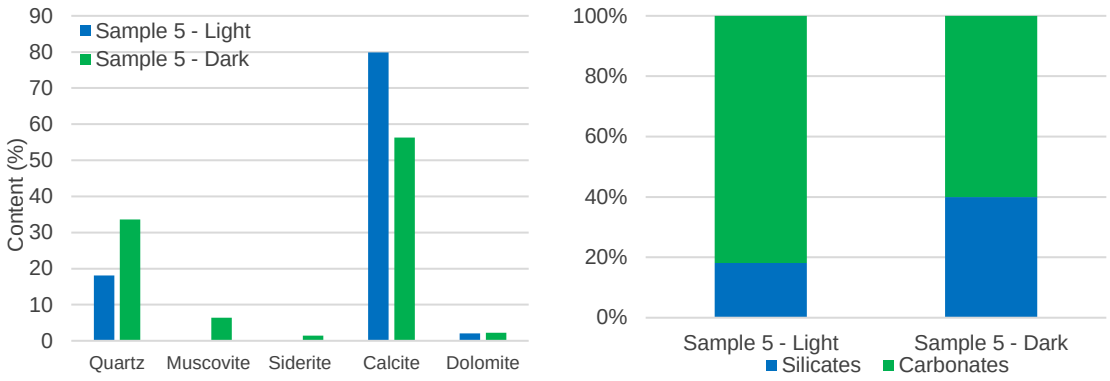


Figure 30 – Left: mineral composition of the two major regions of sample 5. Right: proportion of silicates and carbonates of the two major regions of sample 5.

These compositional variations within the same core plug indicate that heterogeneity can be significant in the Wolfcamp formation. We found some correlation between porosity and mineralogy. Figure 31 shows that porosity increases with quartz content, and total silicates. The correlation with muscovite content was found to be weaker and we did not highlight it in the plot. Porosity was also found to decrease with calcite, and total carbonates content. In this case, the correlation with dolomite was omitted because it was weaker. Similar correlations with mineral content were presented earlier by Chalmers, Ross, and Bustin (2012).

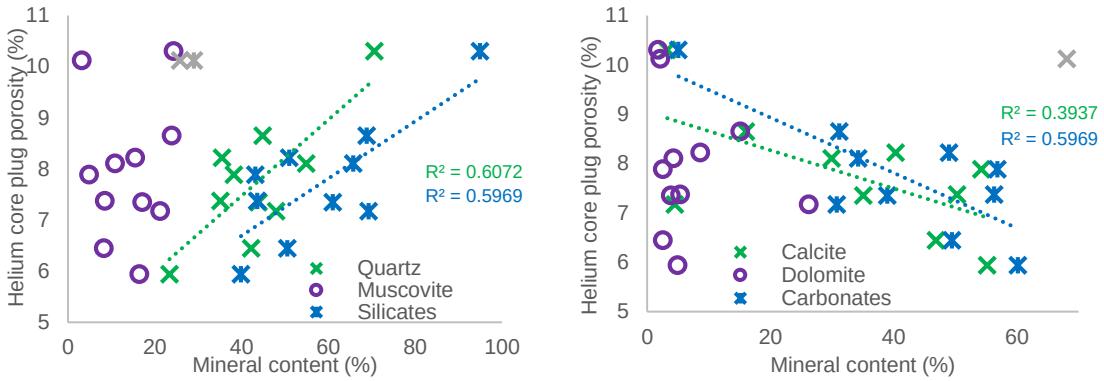


Figure 31 – Relation between the helium porosity measured in core plugs and the mineral composition of the samples. Left: relation with quartz, muscovite and total silicates. Right: relation with calcite, dolomite and total carbonates.

## CORE PLUGS RE-SATURATION

The knowledge of the volume of oil contained in the core samples is required to perform accurate calculations of recovery factor. Once the cores were cleaned and their storage capacity was measured in the laboratory, they were re-saturated with dead crude oil. The core plugs collected from well 1 were saturated with crude oil 1, produced from well 1. Similarly, the core plugs from well 2 were saturated with crude oil 2, produced from well 2. Figure 32 is a schematic of the equipment used for re-saturation. The cores were stored in high pressure vessels and submitted to vacuum for 24 hours. After that, crude oil was allowed to flow to the vessels from two floating piston accumulators, and the pressure was set at 10,000 psig using a syringe pump.

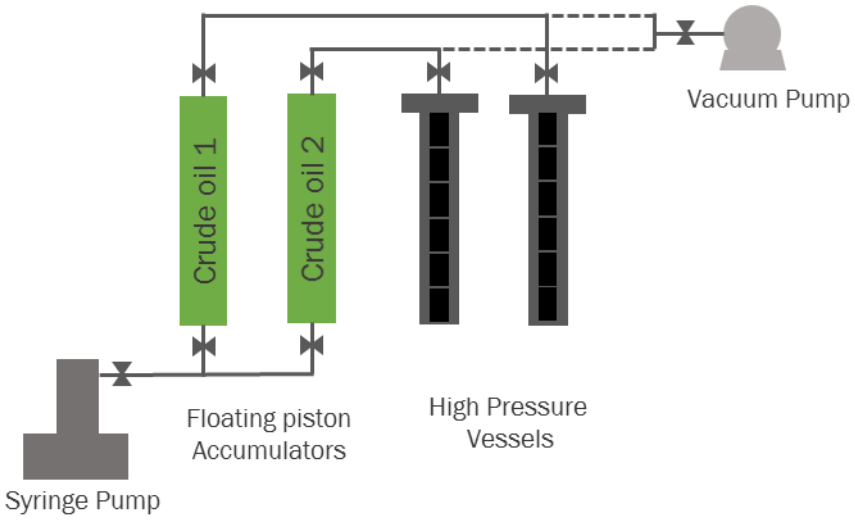


Figure 32 – Schematic of the equipment used for the organic rich shale cores re-saturation with dead crude oil

Oil saturation as a function of time is presented in Figure 33. Most samples reached an oil saturation within the range of 30 to 60% after three to four months under oil injection at high pressure. Oil penetrates the bigger pores first causing the saturation to increase faster during the first month of injection. As time advances, oil is forced to move into smaller pores causing the saturation process to slow down. After three to four months of injection, the increment in saturation as a function of time declines substantially, approaching zero in some cases, indicating the oil has saturated most of the pore volume it can access. The remaining pore volume is comprised by micropores and mesopores that are too small for the larger hydrocarbon molecules to access, or by pores that are large enough to host the molecules but that are connected through smaller pore throats that will not allow higher hydrocarbon molecules to pass.

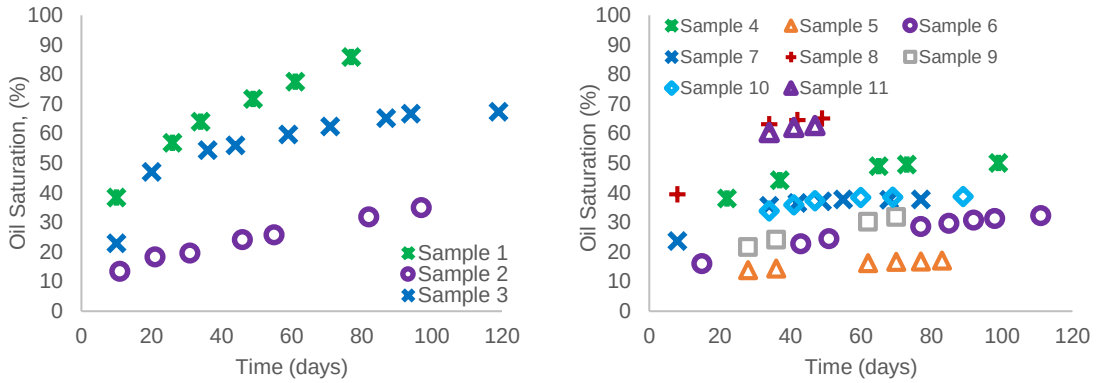


Figure 33 – Oil saturation as a function of time for the re-saturation of the organic rich samples with crude oil. Oil injection pressure was 10,000 psig. Left: samples from well 1, saturated with crude oil 1. Right: samples from well 2, saturated with crude oil 2.

The different slopes in the saturation curves of core plugs that are being saturated under the same conditions, with the same crude oil, provided further evidence of heterogeneity that we have been presenting, and suggest that transport properties in organic rich shales can differ substantially in samples from adjacent depths.

## PORE SIZE DISTRIBUTION

The pore size distribution was obtained from Mercury injection capillary pressure (MICP) experiments. The core plugs were cleaned using toluene and methanol, dried in a convection oven, crushed, and sieved to -20+35 mesh size (Comisky et al. 2011). For samples 1, 2, 3, 4, 6 and 8; MICP was performed in the same plug where all other experiments were executed. The samples were cleaned and dried, porosity and sorption were measured, they were re-saturated with oil and used for gas injection experiments in the CT-scanner; after that, they were cleaned and dried again, and divided in two pieces. One of the pieces was used for XRD analysis, and the other for MICP. For the rest of the samples, a companion core plug was submitted to the MICP analysis while the other tests were performed.

Figure 34 presents histograms showing the pore size distribution for all the core plugs. In all cases, the bin grouping pore throats from 4.9 to 10.1 nm concentrates the highest pore volume. This highlights the unconventional nature of these cores due to the important presence of mesopores, and confirms the core plugs we are using truly represent the characteristics of organic rich shale reservoirs.

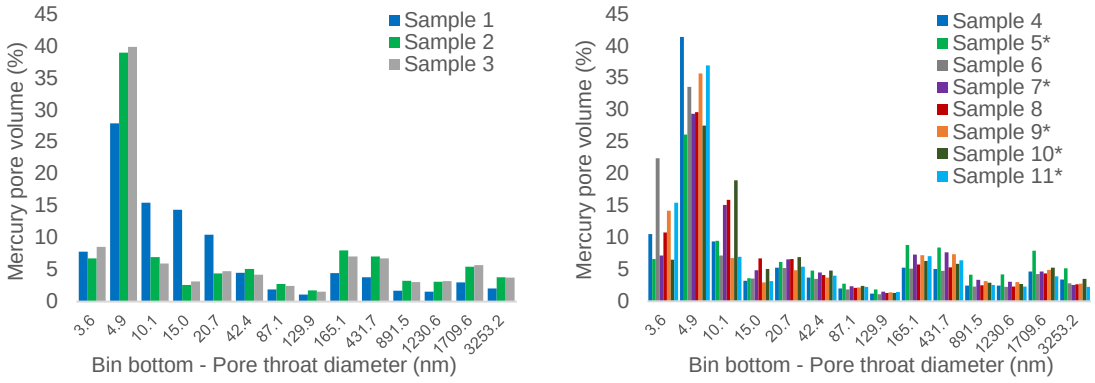


Figure 34 – Pore size distribution from MICP. Left: samples from well 1. Right: samples from well 2. Note that most of the pores are below 5 nm. The (*) indicates the testing was done in a companion sample.

Almost all the core plugs in our investigation have more than half of their pore volume comprised by mesopores (≤ 50 nm) and micropores (< 2 nm). Unfortunately, MICP is only able to investigate pore throat sizes down to 3.6 nm, and therefore we are not able to observe the micropores. Only the controversial sample 5, presented approximately 61 % of macropores (Figure 35). The pore volume in samples 8, 9, and 10 is practically equally divided between macropores and mesopores.

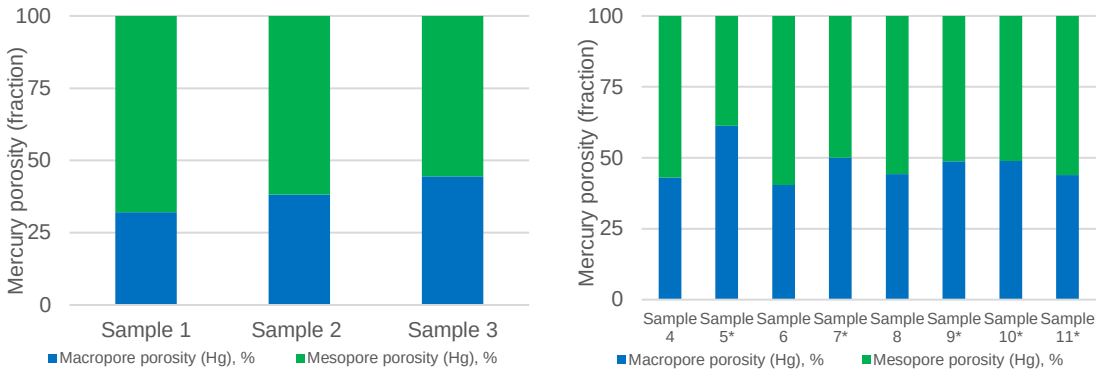


Figure 35 – Fraction of mesopores (≤ 50 nm) and macropores (>50 nm). Note that most samples have more than half of the pore volume comprised by mesopores and micropores. The (*) indicates the testing was done in a companion sample

A comparison of the porosity measured with helium using core plugs, and the one measured with mercury in the crushed rock reveals they are not equivalent (Figure 36). There are several reasons for this. In the first place, the helium molecule is smaller than the mercury molecule. The kinetic diameter of helium is 0.265 nm, whereas the kinetic diameter of mercury is 0.314 nm (Sondergeld, Newsham, et al. 2010). This means that helium can penetrate smaller pores than mercury, resulting in a higher porosity when helium is used for measurement instead of mercury. Also, the measurements made with helium were performed on core plugs, whereas the MICP work was done on crushed samples. This means the experiments with helium also incorporate micro-fractures, and fractures, making the porosity even higher. The gap between helium porosity and mercury porosity is potentially reduced by the grinding process. Crushing the rock samples can communicate pores that were originally isolated, increasing mercury porosity. These aspects need to be considered when observing Figure 36.

For all the samples, the porosity measured with helium was higher than the one measured with mercury. Both the presence of a fracture, and microporosity, are believed to be relevant contributors to the excess of porosity measured with helium. Samples 1, 2, 4, 5, 7 and 8 have fractures that can be distinguished using the CT-scanner, like the ones in Figure 17 and Figure 22. However, the helium porosity of sample 1 is not much higher than its mercury porosity, meaning that in that case the presence of a fracture did not increase

the porosity significantly. On the other side, sample 5 has a fracture that probably contributed to the porosity and it is the reason why samples 5 shows the biggest gap between helium and mercury porosities among all samples. Samples 9 and 10, where there are no fractures visible with the CT-scanner, also have helium porosity significantly higher than mercury porosity, suggesting in this case the microporosity is responsible. Yet, it is also possible that these samples have microfractures that were not captured by CT-scanning. Based on these results it is reasonable to believe there is significant microporosity in the majority of this samples, therefore, and based also on Figure 35, it is safe to say that most of the pore volume in all the samples is comprised of micropores and mesopores.

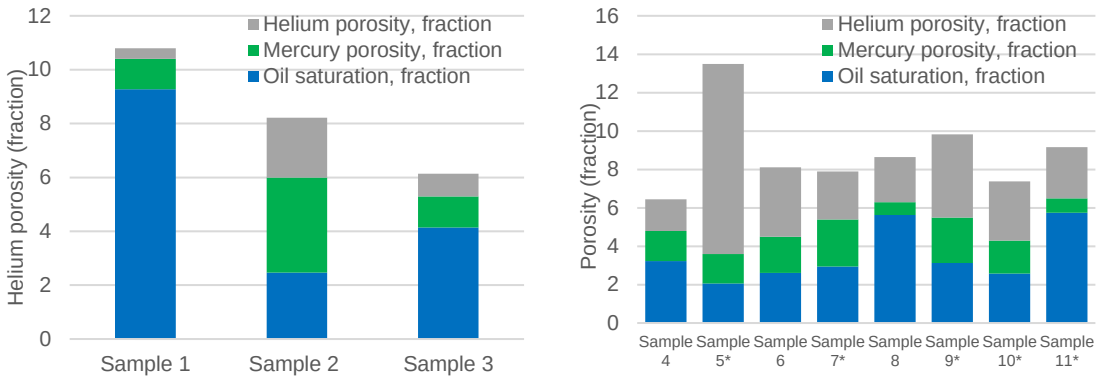


Figure 36 – Comparison of the pore volume saturated by helium, mercury and crude oil. Left: samples from well 1. Right: samples from well 2. Keep in mind that helium porosimetry and oil re-saturation were performed in core plugs whereas MICP was performed in crushed rock. The (*) indicates mercury porosity was measured in a companion sample

The porosity accessed by oil during the saturation process is also presented in Figure 36. Oil is comprised by hundreds of hydrocarbon molecules of different sizes. The composition of the oil from well 1 is shown later in Chapter VI, in Figure 53. We used dead oil in our work, and therefore the lighter hydrocarbon components are not present in our samples. The smaller molecule that was found in significant quantities was hexane. The kinetic diameter of the hexane molecule is 0.692 nm; more than twice the diameters of mercury and helium. The rest of the hydrocarbon molecules are much bigger. For this reason, oil is able to penetrate a much smaller fraction of the pore volume of the rock during the re-saturation process.

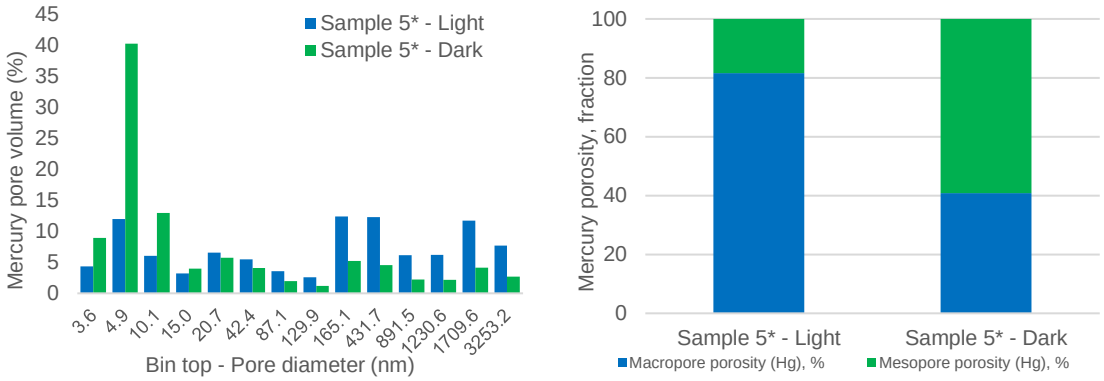


Figure 37 – Pore size distribution and fraction of macropores (≤ 50 nm) and mesopores (>50 nm) in the two different rock types found in sample 5. Note there are marked differences in pore size distribution.

Earlier, we established that sample 5 was comprised of three different rock types. We first identified those three regions using CT-scanner images (Figure 22) that showed well delimited areas of different density. Later, we separated the two major regions, performed XRD analysis on them, and found their mineral compositions are different. The darker region is richer in quartz and total silicates, whereas the lighter one is richer in calcite and total carbonates (Figure 30). Now, we show they also have different pore size distributions (Figure 37). The darker region, richer in silicates, has a higher prevalence of mesopores. Whereas the lighter region, richer in carbonates contain more macropores. Consequently, the total porosity of the darker region, 5.1%, is higher than the total porosity of the lighter one, 2.1%. This finding agrees with the trends of porosity and mineralogy presented in Figure 31, since higher concentration of silicates in the darker region is associated to higher porosity, and higher concentration of carbonates in the lighter area are associated to lower porosity. In fact, we present again the correlation of porosity and mineralogy in Figure 38, but now using mercury porosity measured in crushed cores, instead of the helium porosity measured in the core plugs. The correlations in this case are better for two reasons. The mercury porosimetry is unable to penetrate pore throats below 3.6 nm, and for this reason, the micropores, and some of the mesopores, are not taken into account in this measurement, as we have already stated. Microporosity is mainly associated with the organic matter, meaning that the contribution of the organic matrix has been weakened. Since the mineral composition only comprises the inorganic matrix we should expect a better correlation with a

porosity that is not considering the full contribution of the kerogen. The second reason is the effect of the fractures and microfractures have also been eliminated, making the porosity more representative of the rock matrix.

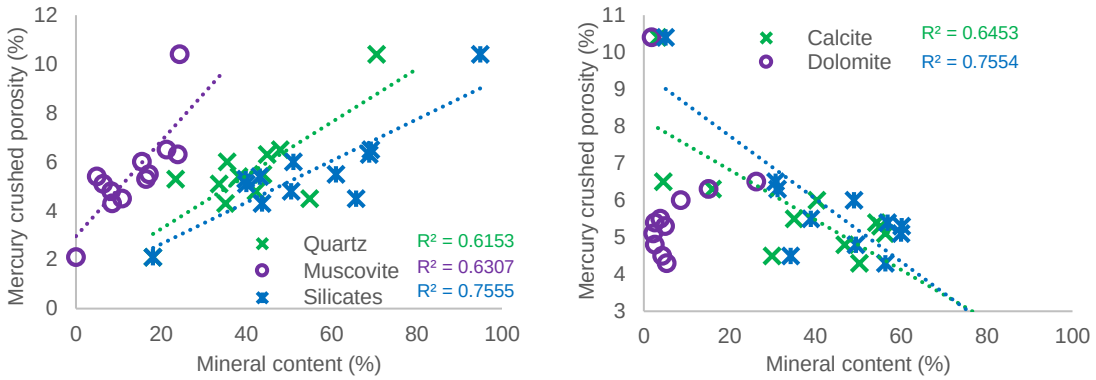


Figure 38 – Mercury crushed porosity as a function of mineral content. Left: Silicates. Right: Carbonates. Note the coefficients of determination are higher than when helium porosity was used.

The stress Swanson permeability to air was also calculated based on the MICP data (Figure 39). Organic rich shale permeability is a complex matter, and there are not yet universally accepted models to describe it. However, we are including the stress Swanson permeability to air just as a reference, to further support the unconventional nature of our samples. We did not find any correlation between permeability and CT-number, as we have presented previously for conventional reservoirs (Skinner, Tovar, and Schechter 2015), nor did we find a correlation between stress Swanson permeability and mineralogy.

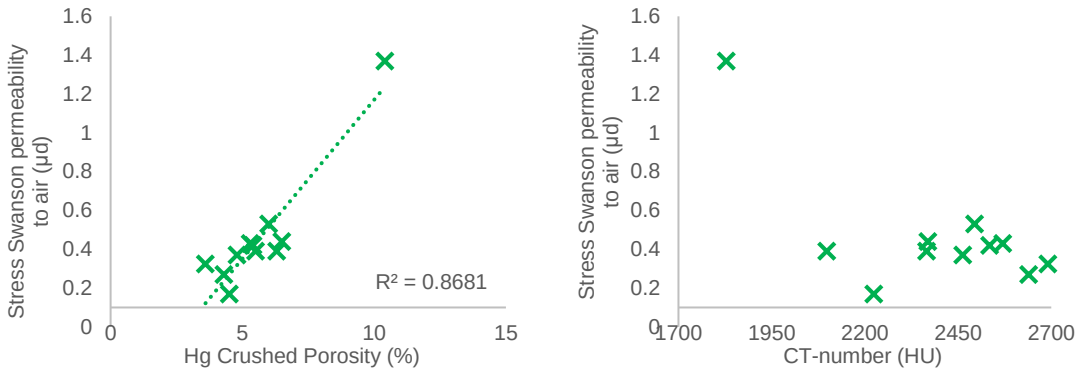


Figure 39 – Left: Stress Swanson permeability as a function of mercury crushed porosity. Right: Stress Swanson permeability as a function of CT-number.

## $CO_2$ – CRUDE OIL MMP

Minimum miscibility pressure is one of the most important design variables for gas injection. It is defined as the pressure at which the crude oil and the injection gas mix in all proportions, and hence there is no interface between them. Theoretically, the displacement efficiency of crude oil by an injection gas at a pressure equal to the MMP or above it, is 100%. This means that all the crude oil contacted by the gas will be displaced. However, the low gas to oil viscosity ratio results in low sweep efficiency, and therefore, the injected gas contacts a limited volume of the crude oil. Despite this, it is highly desirable to operate gas injection processes slightly above the MMP in conventional reservoirs because it results in much higher recovery factors.

It has been argued that MMP is lower in the micropores and mesopores as a consequence of pore confinement of the crude oil (Teklu et al. 2014). However, our current understanding of such phenomena is still incipient and there are no experimental methods yet for the estimation of MMP in organic rich shales. This is complicated by the wide pore size distribution observed in such rocks. Thus, in this investigation, we determine MMP without taking into account the effect of confinement, using the conventional slim tubing technique. This will enable us to observe the importance of the MMP value that can be calculated

with the techniques currently available in the design of a gas injection process in an organic rich shale reservoir.

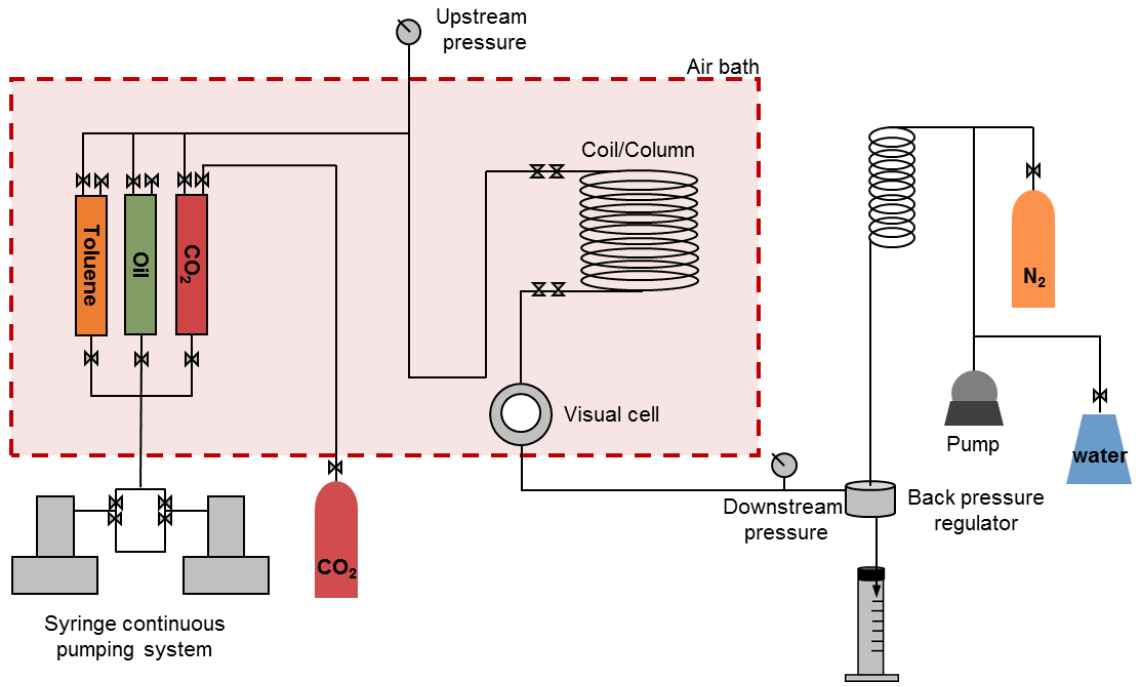


Figure 40 – Schematic of the slim tubing apparatus used for MMP measurements (Tovar 2014, Tovar, Barrufet, and Schechter 2015).

We determined the MMP using the slim tubing technique with a column 80 ft in length, an outside diameter of 0.25 in, and of wall thickness of 0.063 in. Figure 40 is a schematic representation of the equipment. Before oil injection, the column is vacuumed for about 8 hr, and 2 pore volumes of oil are injected at 0.2 $cm^3$/min to reach an oil saturation of 100%. The MMP study then is performed by displacing the crude oil with $CO_2$ at a rate of 0.06 $cm^3$/min. The procedure is repeated at various pressures, and the recovery factor is plotted as a function of the displacement pressure. The MMP is regarded as the point at which there is a sudden change in the displacement efficiency. Below the MMP, recovery is a strong function of pressure as the partial miscibility of the crude oil with the displacement gas increases with pressure. Above the MMP, since the crude oil and the displacement gas are already mixed in all proportions and the displacement efficiency

is theoretically 100%, recovery is a weak function of pressure. More details about our procedures for MMP determination can be found in Adel, Tovar, and Schechter (2016), Tovar, Barrufet, and Schechter (2015), and Adel (2016). The recovery factor as a function of pressure for crude oil 1 and crude oil 2 are presented in Figure 41. Crude oil 1 has a MMP of 3,706 psig whereas crude oil 2 has a MMP of 1,925 psig. In both cases, dead crude oil was employed.

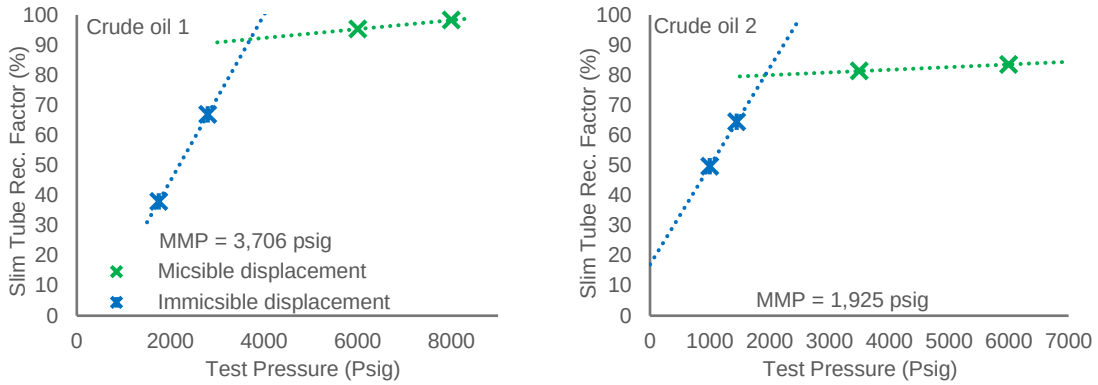


Figure 41 – Slim tube recovery factor as a function of pressure for MMP determination with $CO_2$. Left: Crude oil 1, MMP = 1,925 psig. Right: Crude oil 2, MMP = 3,706 psig

## SUMMARY

This chapter presented a comprehensive workflow that enables the preparation of core samples for the investigation of enhanced oil recovery processes in organic rich shales reservoirs. The process, which takes from four to five months, comprises cleaning, measuring storage capacity, and re-saturating the organic rich shale core plugs.

For the storage measurements, we took three different approaches towards compressibility. The first approach neglected rock compressibility and resulted in an underestimation of the grain volume, and therefore, an overestimated porosity. The second approach, considered the rock compressibility to be

constant between room pressure and the experimental pressure. Whereas the third approach, considered the compressibility to be constant only between two consecutive experimental pressures. We performed all measurements below 1,000 psig, and for that range of pressure we did not observe significant differences between the results obtained using the second and third approaches.

We found that porosity, sorption, and TOC, correlate with CT-number. This is a significant contribution towards the characterization of organic rich shale plays. The CT-number of a core plug can be measured in a few minutes in enabling estimations of TOC, porosity, and sorption capacity for organic rich shale samples, much faster than with the use of the current methods. Of course, laboratory measurements in a few samples are still required to create a reliable correlation. The use of CT-number to estimate porosity is desirable as it is based on the density of the bulk rock, and therefore, will account for fractures and micro-fractures.

Quartz and calcite are the principal minerals found in our samples. Even though the samples are from adjacent depths in their respective wells, five of the eleven samples are mainly comprised by silicates, four by carbonates and two have almost identical proportions of them. We found porosity to increase with quartz and total silicate content, and to decrease with calcite and total carbonate content. This has been previously shown in literature. In the case of mineral content, the matrix porosity measured with mercury in crushed samples showed slightly better correlations than the porosity measured in whole cores with helium. We argued this is because mercury porosity does not consider the presence of fractures and micropores, whereas helium porosity does.

According to our results, at high pressure most of the $CO_2$ is stored in the core plugs in a free state. Above 2,500 psig, sorption accounts for only up to 20% of the storage capacity. Whereas at low pressure, sorption is the most relevant storage mechanism. Significant errors can be made in the calculation of sorption capacity when the volume occupied by the sorbed layer of the measuring fluid, or the rock compressibility, are not accounted for. For our samples, the use of the Dubinin approximation, based on the b parameter of the Van der Walls equation of state, provided for a reasonable approximation for the density of the sorbed layer.

Small errors in the determination of the rock compressibility can lead to significant errors in the determination of sorption capacity.

The re-saturation of organic rich shale core plugs with crude oil was accomplished at high pressure. It took from three to four months to achieve 30 to 60% oil saturation in most samples. The access of crude oil to the pore space is limited by the small size of the pores, and pore throats. The pore size distribution of our samples is such that close to half, or more than half of the pore volume is comprised by mesopores (≤50 nm). Nonetheless, we measured pore size distribution using mercury, and the total porosity resulting from these experiments is consistently lower than the helium porosity. We attribute that difference to the fact that the molecule of helium is smaller and can reach micropores, whereas the molecule of mercury cannot. Also, mercury porosity was measured in crushed cores with no fractures and micro-fractures, whereas helium porosity was measured in core plugs, where fractures and micro-fractures are considered. Based on this, it is reasonable to believe that our samples have significant microporosity that was not captured by the MICP analysis, and therefore, we can infer than more than half of the pore volume in all of our samples is comprised by micropores and mesopores. That is the reason why the hydrocarbon molecules cannot saturate the entire pore volume. We need to keep in mind that we used dead oil for the re-saturation process, and the smaller molecule found in significant quantities through GC was hexane, which is more than twice as big as the helium and mercury molecules. All the experiments we did in our samples demonstrated that significant heterogeneity exits among them, even when they are from adjacent depths, highlighting the heterogeneous nature of the Wolfcamp formation.

Finally, we measured MMP for our crude oil samples using the slim tubing technique. For crude oil 1, the resulting MMP was 3,706 psig, whereas for crude oil 2 it was 1,925 psig. MMP will play an important role in the experimental design for the next chapters since a major goal of this investigation is to understand the role of the reservoir pressure in the process, and how it is related to the MMP measured for bulk oil systems, without accounting for the effect of confinement in small pores.

# CHAPTER V

# EFFECT OF PRESSURE AND SOAKING TIME ON RECOVERY FACTOR

We established in chapter III that $CO_2$ can be used to extract the naturally occurring crude oil contained in organic rich shale reservoir rocks. However, there was significant uncertainty regarding the recovery factors that could be achieved. Such uncertainty, prompted us to develop and adapt the rock preparation and characterization procedures presented in Chapter IV. In this chapter, we use the organic rich shale core plugs that were cleaned and re-saturated with crude oil to perform experiments like those performed in Chapter III. Yet, now we possess an accurate knowledge of the oil saturation within the core that enables us to make accurate recovery factor measurements. We present a series of experiments that investigate the effect of soaking time, operating pressure, and the relation between operating pressure and slim-tube MMP.

In this chapter we focus on the understanding of how externally controlled operational parameters can be adjusted to maximize recovery factor under gas injection. Here, we limit ourselves to a discussion of the experimental observations and their practical implications, and leave the discussion regarding the role that the poor fluid transport through the rock and the oil composition play in recovery for the next chapter.

## EXPERIMENTAL PROTOCOL

These experiments resemble the ones performed in preserved sidewall cores described in Chapter III. The core plugs are packed in an aluminum core-holder and the presence of a hydraulic fracture is simulated using glass beads as depicted in Figure 7. The core-flooding equipment used to perform the gas injection process is integrated to a CT-scanning device (Figure 8). Once again, what set these experiments apart from the ones presented earlier, is that in this occasion we have knowledge of the volume of oil contained in the core samples, and therefore, we can make accurate recovery factor calculations.

Nine experiments were performed injecting carbon dioxide in organic rich shale core plugs from the Wolfcamp formation, through a hydraulic fracture. The first set of experiments was comprised of three tests using the core plugs and the crude oil from well 1 (Figure 42).

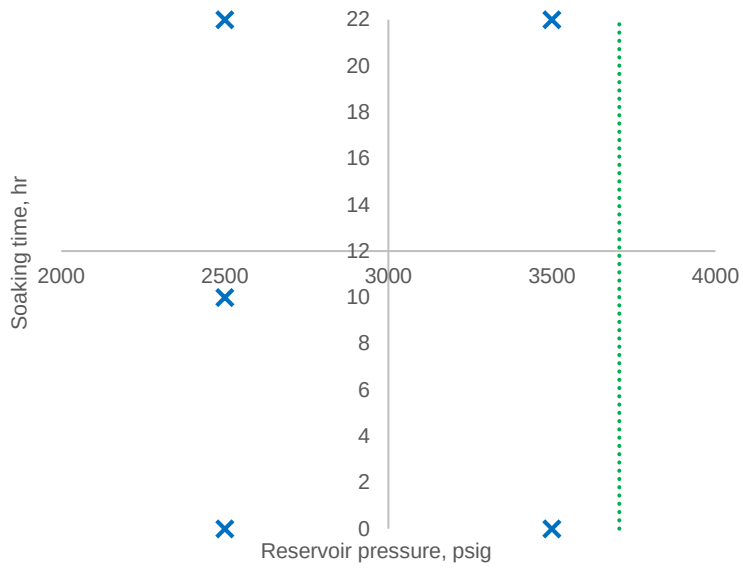


Figure 42 – Experimental matrix for the first set of runs with cores and crude oil from well 1. The points represent the conditions of the data points collected in our experimental runs and the line is the MMP for crude oil 1 which was 3,706 psig. All experiments were performed at 165 ˚F.

For each one of the runs, the soaking time was kept constant, and two operation pressures were investigated. The soaking times were 22 hours, 10 hours, or in the case of continuous injection, zero hours. Each test was performed for two pressures, 2,500 and 3,500 psig. The first pressure step is significantly below the slim tube MMP of the crude oil 1, which is 3,706 psig; whereas the second pressure step is at near miscible conditions. For the huff-and-puff cases, three huff-and-puff cycles were done at each pressure level. For the continuous injection case, one pore volume was injected every 12 hours, and after three days of injection, the pressure was increased from 2,500 psig to 3,500 psig, and three more days of injection were performed. One pore volume is comprised of the fracture volume re-created with the glass beads, and the helium pore volume measured for each shale sample. In all experiments, the temperature was kept constant at the

reservoir temperature of 165˚F. For the experimental run performed at 10 hours of soaking time, only one data point was collected at 2,500 psig. This was because the experimental set-up failed when the pressure was being increased to 3,500 psig, and we were unable to reinstate the test.

The second set of experiments was comprised of six tests using the core plugs and crude oil from well 2. In this case, three pressure levels and two soaking times were investigated. The pressure levels were 1,200 psig, 2,100 psig, and 3,100 psig. The experiments performed at 1,200 psig were done significantly below the slim tube MMP of 1,925 psig. The ones performed at 2,100 psig were done slightly above, and the ones at 3,100 psig were notably above the MMP. The soaking time was either 22 hours, or zero, corresponding to continuous injection. In contrast with the first set of experiments, both pressure and soaking time were kept constant for the duration of each run; and the experiments were continued until an incremental recovery factor of less than 2% was attained for 24 hours.

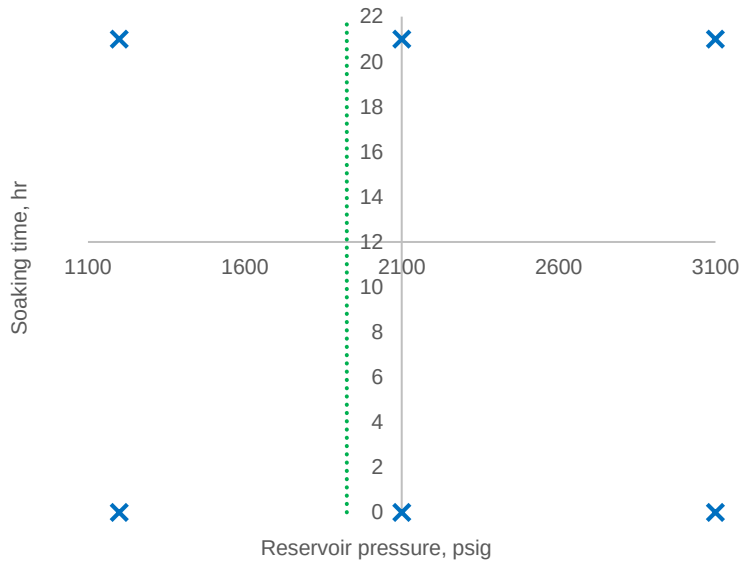


Figure 43 – Experimental matrix for the second set of experiments with cores and crude oil from well 2. The points represent the conditions of the experimental runs and the line is the MMP for crude oil 2. All experiments were performed at 165 ˚F.

**Recovery factors**

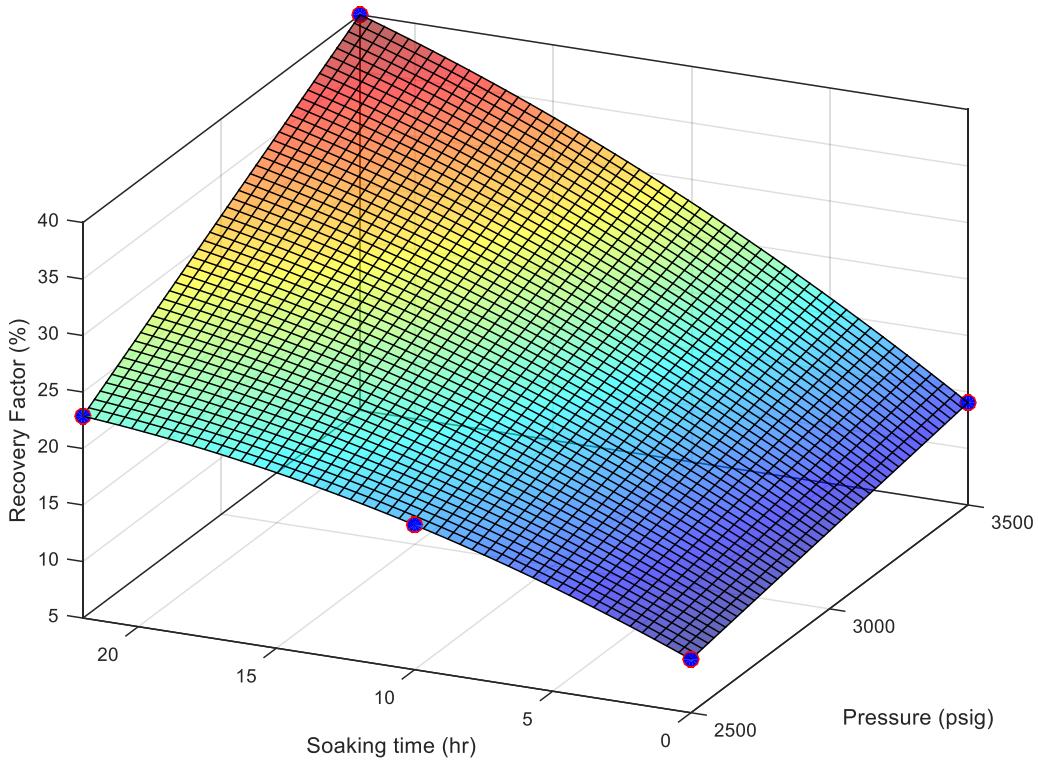


Figure 44 – Surface response of recovery factor as a function of pressure and soaking time for the first set of experiments, performed with the core plugs and the crude oil from well 1.

Figure 44 presents a surface response of recovery factor as a function of pressure and soaking time for the first set of experiments. The maximum recovery factor was of 40%, reached at the maximum pressure of 3,500 psig, and the maximum soaking time of 22 hours. Conversely, the lowest recovery factor was close to 10%, obtained under continuous injection at the lowest pressure of 2,500 psig. Figure 44 suggests that both factors, pressure and soaking time, heavily influence recovery. Higher pressure and higher soaking times lead to higher recovery, whereas lower pressure and lower soaking time leads to lower recovery.

| Test run | Sample | Soaking time (hr) | Pressure (psig) | Recovery factor (%) | Error (%) |
|---|---|---|---|---|---|
| 1.1 | 1 | 22 | 2,500 | 23 | ± 0.5 |
| 1.1 | 1 | 22 | 3,500 | 40 | ± 0.5 |
| 1.2 | 2 | 10 | 2,500 | 18 | ± 1 |
| 1.2 | 2 | 10 | 3,500 | 0* | ± 0* |
| 1.3 | 3 | 0 | 2,500 | 10 | ± 1 |
| 1.3 | 3 | 0 | 3,500 | 14 | ± 1 |

Table 12 – Conditions and recovery factors for the first set of experiments performed using cores and crude oil from well 1 drilled in the Wolfcamp formation. All runs were performed at the reservoir temperature of 165 F. The slim tube MMP for crude oil 1 is 3,706 psig. The (*) denotes a system failure during the experiment.

The recovery factor of 40% reached at 3,500 psig during the test run 1.1 demonstrates that significant recovery can be achieved using carbon dioxide in organic rich shale reservoirs at pressures close to the slim tube MMP for the crude oil – $CO_2$ system (Table 12). The crude oil produced during the experiments was significantly lighter than the oil injected into the core plugs. This was made evident by simple observation of the color of the crude oil samples and it was later confirmed by gas chromatography analysis. The produced samples were light yellow whereas the injected oil was dark brown to black. This change in composition gives insights regarding the production mechanisms, but also implies that the crude oil contacted by the $CO_2$ at 3,500 psig during test run 1.1 had a different composition, and therefore, a different MMP than the original oil. This is a consequence of the production of the lighter components during the three cycles of injection at 2,500 psig performed before increasing the pressure to 3,500 psig, during that same experimental run. This circumstance prompted some changes in the experimental design for the second set of experiments.

The helium porosity of samples 1, 2, and 3, are 10.30, 8.22 and 5.94%, respectively (Table 10). In Figure 44, there is also a positive correlation between porosity and recovery. Higher porosities are often associated with better transport properties that could facilitate recovery. We present an argument regarding the role of transport in recovery factor in organic rich shale in the next chapter.

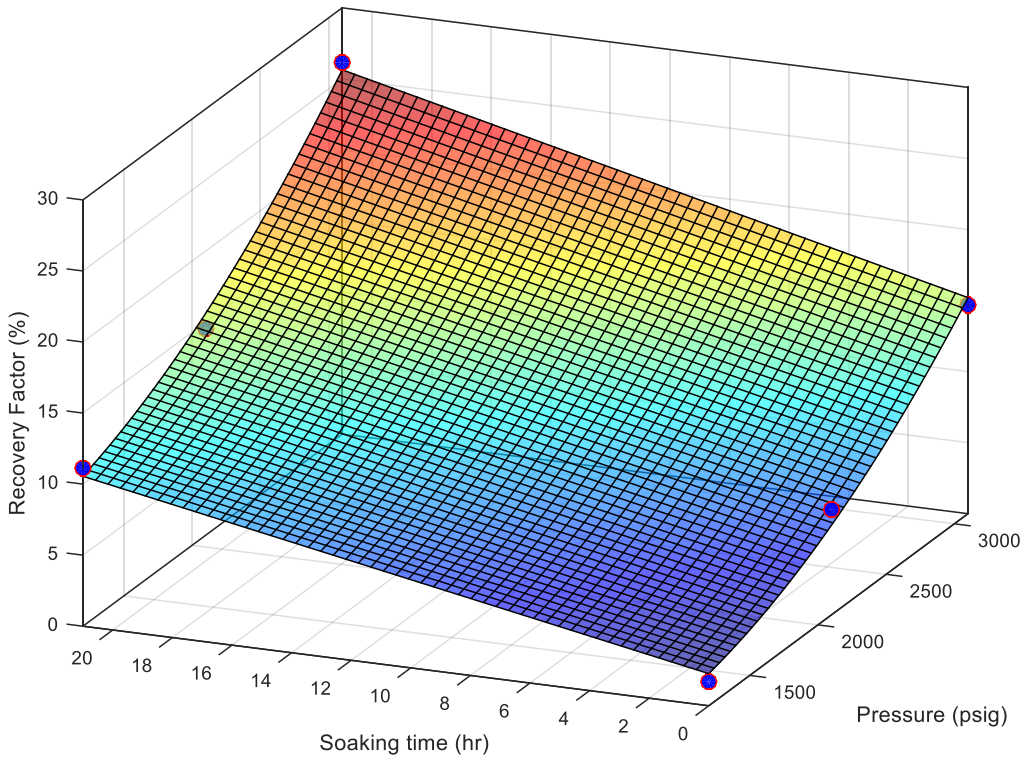


Figure 45 – Surface response showing recovery factor as a function of soaking time and pressure for the second set of experiments performed using the core plugs and the oil from well 2.

Figure 45 shows a surface response of recovery factor as a function of pressure and soaking time for the second set of experiments. Once again, the highest recovery factor of 26.15% was obtained at the highest pressure of 3,100 psig, and the longest soaking time of 21 hours (Table 13). The test with the lowest recovery factor was conducted under continuous injection at 1,200 psig, and it did not present any oil recovery. The same pressure, with a soaking time of 21 hours resulted in a recovery factor of 11.13%. These results further indicate the recovery factor is considerably influenced by both pressure and soaking time, and put $CO_2$ in an attractive position to be used for EOR in organic rich shales. Recovery factors of the orders reported in these experiments can potentially add billions of barrels of crude oil reserves, given the vast amount of resources contained in unconventional plays. In all the experiments $CO_2$ was at supercritical conditions.

| Test run | Sample | Soaking time (hr) | Pressure (psig) | Recovery factor (%) | Error (%) |
|---|---|---|---|---|---|
| 2.1 | 4 | 21 | 1,200 | 11 | ±1 |
| 2.2 | 5 | 0 | 2,100 | 7 | ±1 |
| 2.3 | 6 | 21 | 2,100 | 15 | ±1 |
| 2.4 | 8 | 21 | 3,100 | 26 | ±0.9 |
| 2.5 | 9 | 0 | 1,200 | 2 | ±1 |
| 2.6 | 11 | 0 | 3,100 | 15 | ±0.9 |

Table 13 – Conditions and recovery factors for the second set of experiments performed using cores and crude oil from well 2 drilled in the Wolfcamp formation. All runs were performed at the reservoir temperature of 165 F. The slim tube MMP for crude oil 1 is 1,925 psig.

**Effect of pressure on recovery factor**

Operating pressure heavily influenced recovery factors in our experiments. Increasing pressure always led to an increase in the recovery factor. During the first set of experiments, performed with core plugs and crude oil from well 1, an increment of 1,000 psig in pressure during continuous flooding, from 2,500 to 3,500 psig, rose the recovery factor by 44.4%, from 9.73 to 14.05% (Figure 46). A similar increase of pressure during the huff-and-puff case with a soaking time of 22 hours resulted in an increment of 74.9% in recovery factor. All the runs of the first set of experiments were performed below the MMP of 3,706 psig. The strong dependence of recovery factor on pressure below the slim tube MMP coincides with the behavior of conventional reservoirs.

The second set of experiments confirmed that higher operating pressure results in a higher recovery factor. In this case, increasing the pressure from 1,200 to 2,100 psig, raised the recovery factor by 338% during continuous injection, and by 52.4% during huff-and-puff with a soaking time of 22 hours. Similarly, when the pressure was raised from 2,100 to 3,100 psig, recovery factor increased in 98% for the continuous injection case, and by 80% for the huff-and-puff run (Figure 46).

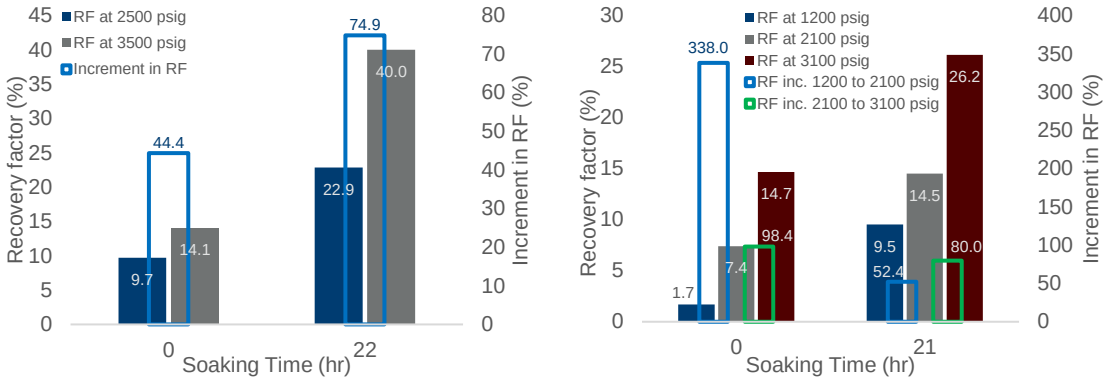


Figure 46 – Effect of pressure in recovery factor. Left: first set of experiments performed with core plugs and oil from well 1, MMP for this case is 3,706 psig. Right: second set of experiments, performed with core plugs and crude oil from well 2, MMP for this case is 1,925 psig.

The results obtained in the second set of experiments represent a sharp departure from the conventional wisdom. This is because further increases in pressure above the slim tube MMP of 1,925 psig caused the recovery factor to almost double. This was observed in both injection schemes investigated, continuous injection and huff-and-puff.

The experiments performed at 2,100 psig, and 3,100 psig are both above the MMP (Table 13). In conventional reservoirs, once the MMP is reached, oil and $CO_2$ mix in all proportions to create a unique phase. Under those conditions, the absence of an interphase between the oil and the $CO_2$ eliminate capillary forces, thus maximizing displacement efficiency. Consequently, further increments in pressure do not have a meaningful effect on the displacement efficiency, and the recovery factor becomes a weak function of pressure. Conversely, this is not what the results for organic rich shale reservoirs suggest. According to Figure 45, in organic rich shale reservoirs, further increments in pressure above the slim tube MMP lead to higher recovery factors. This was true for both huff-and-puff, and continuous injection.

This major deviation from the behavior expected in conventional reservoirs must be considered during the design of gas injection processes in organic rich shales. It should also be noted that this behavior is counter-intuitive given what is being proposed with regards to the phase behavior of fluids contained in organic rich

micropores and small mesopores. The MMP is expected to be reduced because of confinement, however, the experimental results shown in Figure 45 indicate that if this improvement in phase behavior occurs, its effect is outweighed by the negative influence of the poor transport in organic rich shale rocks. We will elaborate on this topic in the next chapter when we address the recovery mechanisms.

**Effect of soaking time on recovery factor**

We also found soaking influences recovery factor. During the first set of experiments using the oil and core plugs from well 1, increasing soaking time from zero to 22 hours while keeping the pressure constant at 2,500 psig resulted in a recovery factor increase of 135% (Figure 47). At 3,500 psig, the same increase in soaking time resulted in 184% increase in recovery factor. At both pressure levels investigated, the recovery factor more than doubled when going from continuous injection to the huff-and-puff like scheme. The intermediate soaking time of 11 hours shown in Figure 44 suggest that recovery factor does not grow linearly with soaking time and therefore an optimal soaking time must exist, beyond which further increments in soaking time will not result in significant additional oil recovery.

We obtained comparable results for the second set of experiments using the core plugs and the crude oil from well 2. At the three pressure levels of 1,200, 2,100 and 3,100 psig, the recovery factor was significantly increased by switching from a continuous injection to a huff-and-puff like scheme. This was the case above and below the slim tube MMP of 1,925 psig. Below MMP, at 1,200 psig, recovery was increased by almost five folds. Whereas above the MMP, at 2,100 and 3,100 psig, recovery was nearly doubled.

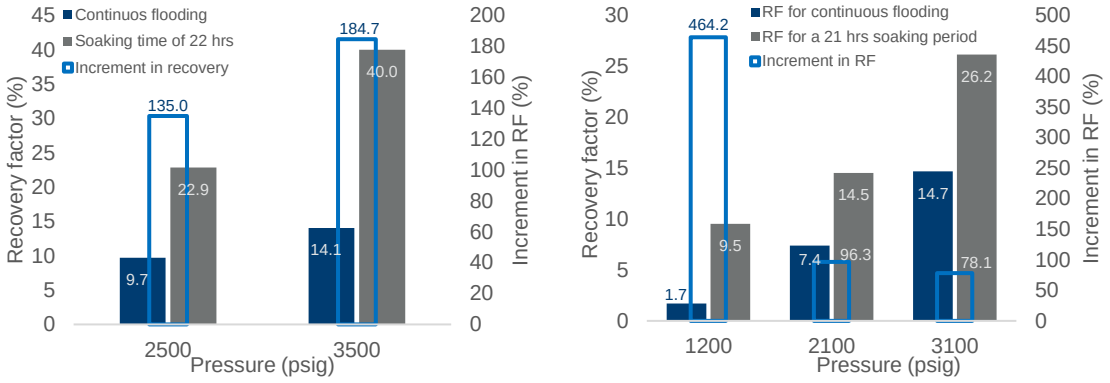


Figure 47 – Effect of soaking time in recovery factor. Left: first set of experiments performed with core plugs and oil from well 1. Right: second set of experiments, performed with core plugs and crude oil from well 2.

It becomes clear from our results that a huff-and-puff scheme is more appropriate for the application of gas injection with EOR purposes in organic rich shale reservoirs. We believe this behavior is closely related to the vaporizing and condensing gas drive mechanisms for miscibility development, and we will expand on this argument in the following chapter.

**Time-frame for recovery**

Almost as important as the attainable recovery factors is the time frame in which such recovery can be reached. The low transport in organic rich shale plays creates concerns regarding the feasibility of enhanced oil recovery processes. They could take too long. In chapter IV, we desmostrated that saturating the organic rich shale core plugs with helium for porosity measurement, $CO_2$ for sorption measurements, or crude oil, are lengthy processes. However, we also have shown that we do not intend to inject $CO_2$ directly into the matrix, but through a hydraulic fracture, this would make injection a fast process.

Our experimental results show that recovering oil from organic rich shale reservoirs using $CO_2$ is not a lengthy process. Figure 48 illustrates recovery as a function of cycle number for one of the huff-and-puff experiments, and recovery factor as a function of injection time for one of the continuous test runs. In the

case of huff-and-puff, most of the recovery is attained in the first cycle, which implies that it happens within the first 24 hours. Similar results were observed in all the huff-and-puff experiments. This is of great importance, because as we have seen, huff-and-puff consistently provided the highest recovery factors, and we are recommending this injection scheme for field applications. On top of that, huff-and-puff makes more sense operationally.

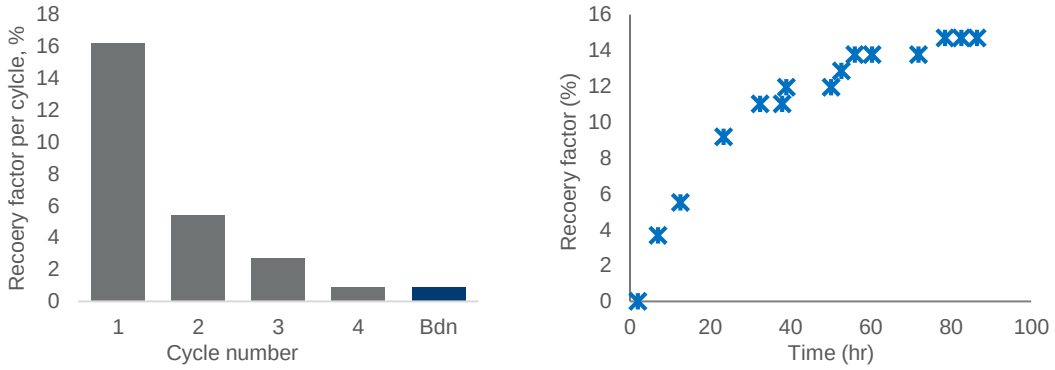


Figure 48 – Left: recovery factor per cycle during huff-and-puff injection of $CO_2$ in an organic rich shale core plug, the example shown is for test run 2.4 at 3100 psig and soaking time of 21 hrs. Bdn stands for blowdown. Right: Recovery factor as a function of time during continuous $CO_2$ injection in an organic rich shale core plug, the example shown corresponds to test run 2.6 at 3100 psig.

For continuous injection, recovery is also attained in a short period. A similar production profile was observed in all the experimental runs where continuous injection was applied. Most of the recovery is obtained within the first 24 hours. The speed at which the hydrocarbon molecules can migrate to the gas phase is a clear indication of the relevance of the diffusion based transport mechanisms in this process, since Darcy flow under this low transport conditions would suggest longer time frame for recovery, more aligned with our observations during the re-saturation stage.

SUMMARY

We presented in this chapter recovery factors measured in organic rich shale core plugs that were re-saturated with crude oil in the laboratory. The knowledge of the volume of oil present in the sample enabled the accurate calculation of recovery factor. The experiments were designed to observe the effect of operating pressure and soaking time on recovery. Two sets of experiments were performed, the first set employed core plugs and crude oil from well 1, whereas the second used the cores and crude oil from well 2. Both wells are in the Wolfcamp formation in the Permian Basin, and we addressed the oil and rock properties in Chapter IV. The maximum recovery factor was 40% for the first set of experiments and 26.15% for the second. These results highlight the great potential for $CO_2$ to be used for EOR in organic rich shale reservoirs. Considering the 20 billion of undiscovered, technically recoverable resources contained in the Wolfcamp formation of the Permian basin, according to USGS estimations, it is easy to picture how the application of gas injection for EOR can dramatically extend the life and potential of crude oil bearing organic rich shales.

This chapter focuses on the effect of operating pressure and soaking time because they can be manipulated by the operator to optimize the process. We found both variables to heavily influence recovery factor. Increasing operating pressure notably rises recovery factor. This was demonstrated in both sets of experiments performed. Increasing the pressure by 1,000 psig increased recovery factor from 44 to 338%, depending on soaking time and crude oil composition. A major departure with respect to the behavior of conventional reservoirs is that further increments in pressure beyond the slim tube MMP resulted in significant additional recovery. This was observed from the results of our second set of experiments. Indeed, the shape of the surface response for the second set of experiments suggest that we would obtain larger recovery factor at higher pressures than the ones tested, meaning that we should operate at pressures significantly higher than the slim tube MMP.

Similarly, going from continuous flooding to soaking times of 21 and 22 hours increased recovery factor from 78.1 to 464.2%, depending on operating pressure and crude oil composition. This indicates that a huff-and-puff scheme is optimal for this process. The addition of an intermediate soaking time of 10 hours in the first set of experiments suggests that recovery is not a linear function of soaking time, and an optimal soaking time must exist, beyond which further increments in soaking time will not result in significant additional oil recovery.

Even when the transport properties of the core plugs are extremely poor, the oil recovery process is fast. In our first set of experiments, we produced up to 40% of the initial oil in the core plugs in the span of six days. And in the second set, we produced up to 26% in 4.2 days. Moreover, the highest rate of recovery was observed in the first 24 hours, for both huff-and-puff, and continuous injection. These times are inconsistent with Darcy flow, which would result in longer periods for fluid transport, in agreement with what was observed during the re-saturation of the core-plugs with oil. This strongly suggest other transport mechanisms, such as molecular diffusion, are involved. $CO_2$ is known to easily diffuse through different materials, and the selective vaporization of the lighter components enable the smaller molecules to move out of the organic rich shale matrix into the $CO_2$ phase leaving the heavier, bigger molecules, behind. This constitutes an important feature of the transport and recovery mechanisms.

Finally, our experimental results indicate that the field operation of gas injection with EOR purposes in organic rich shale reservoirs should be performed in huff-and-puff fashion at pressures significantly above the slim-tube MMP. However, we make further discussion regarding field applications in Chapter VII.

# CHAPTER VI

# MECHANISMS OF RECOVERY

We present in this chapter additional experimental data and analysis that provide insightful information regarding the mechanism of recovery during gas injection with EOR purposes in organic rich shale reservoirs. We introduce a set of additional experiments performed with carbon dioxide in a high permeability sandstone reservoir rock. By contrasting recovery in high permeability rock and organic rich shale we understand the role of transport on recovery. We also present a set of experiments performed using nitrogen as EOR gas in organic rich shale. This improves our understanding of the role of miscibility when we compare the results with the recovery factors we presented in the previous chapter, using $CO_2$. We make use of the data captured using the CT-scanner to illustrate the changes in composition with time and position. This chapter provides a clear picture of the kinetics of the mass transfer process between the gas injected and the crude oil. We close this chapter by using ternary diagrams to explain the effect of transport, pressure, and soaking time on recovery during gas injection in organic rich shale.

## $CO_2$ INJECTION THROUGH A HYDRAULIC FRACTURE IN A HIGH PERMEABILITY RESERVOIR ROCK

We conducted three experiments using 100 md permeability Berea sandstone (Table 14). Each one of them was designed to resemble experiments performed previously with organic rich shale, the rock type being the only difference. The test run 1.4 was performed to resemble experiment 1.1 from the first set of experiments, which used the crude oil from well 1. That experiment consisted of three huff-and-puff cycles at 2,500 psig, followed by three more cycles at 3,500 psig. The test runs 2.7 and 2.8, were done to resemble experiments 2.3 and 2.4 using crude oil from well 2. They were performed at 2,100 and 3,100 psig respectively. We maintained constant pressure during each one of these experiments, and performed huff-and-puff injection until the incremental recovery factor between two consecutive cycles was less than 2%. For the test run 1.4, the experimental pressure was close, but below the slim-tube MMP for the crude oil 1, of 3,706 psig. For

the experiments 2.7 and 2.8, the experimental pressure was above the slim tube MMP measured for crude oil 2 of 1,925 psig. Reservoir temperature of 165˚F was used for all experiments.

| Test run | Duplicated run | Sample | Soaking time (hr) | Pressure (psig) | Recovery factor (%) | Error (%) |
|---|---|---|---|---|---|---|
| 1.4 | 1.1 | Berea 1 | 22 | 2,500 | 38 | ±0.3 |
| 1.4 | 1.1 | Berea 1 | 22 | 3,500 | 55 | ±0.3 |
| 2.7 | 2.3 | Berea 2 | 21 | 2,100 | 37 | ±0.3 |
| 2.8 | 2.4 | Berea 3 | 21 | 3,100 | 44 | ±0.2 |

Table 14 – Description and results of the experiments performed in using Berea sandstone of 100 md of permeability. Experiment 1.4 was performed with crude oil from well 1, and experiments 2.7 and 2.8 with crude oil from well 2. Temperature was 165˚F.

We present the results from test run 1.4 in Table 14 and in Figure 49. The figure shows the surface response obtained during the first set of experiments performed with organic rich shale core plugs and crude oil from well 1, together with the results from the experiment repeated in 100 md Berea sandstone. At first, the recovery factor of 55.33% obtained with Berea seems low for a clean, homogeneous, 100 md rock flooded at near miscible conditions at 3,500 psig. In our experience, bearing in mind that there was no water present in this experiment, we would expect to recover more than 80% of the oil in place in a conventional core-flooding. For reference, we have obtained 73% recovery in Berea sandstone of only 12 md in the presence of water. Water reduces recovery by obstructing the $CO_2$ from contacting the oil (Tovar, Barrufet, and Schechter 2015).

For test 1.4 we could argue that the oil contacted at near miscible conditions had been altered by the three production cycles performed previously at the lower pressure of 2,500 psig. And therefore, MMP could have increased causing the low recovery. This is because all huff-and-puff experiments performed with crude oil from well 1 consisted of three injection cycles at 2,500 psig, and three injection cycles at 3,500 psig.

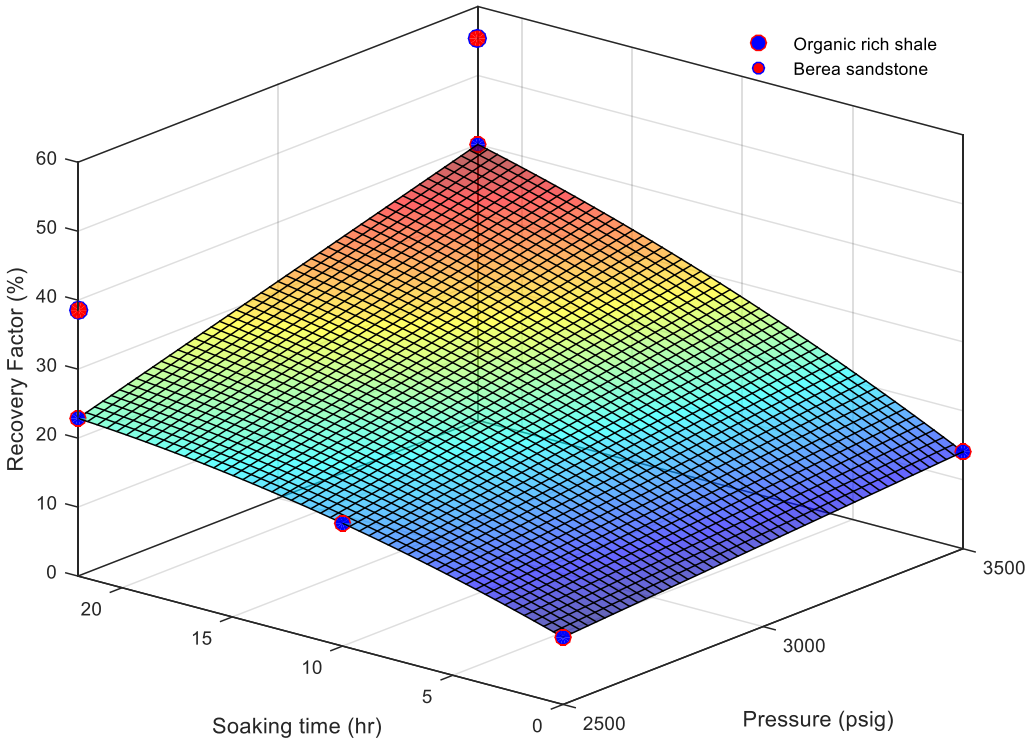


Figure 49 – Surface response of recovery factor as a function of pressure and soaking time for the first set of experiments performed with organic rich shale rock and crude oil from well 1, showing two additional points in red for the test points repeated with 100 md Berea sandstone. The slim tube MMP is 3,706 psig.

The results from the repeated tests 2.7 and 2.8, performed with 100 md Berea sandstone using crude oil from well 2, are not much better. Pressure for these experiments were 2,100, and 3,100 psig respectively, both above the slim tube MMP for crude oil 2. The pressure was maintained constant, so there were no compositional changes in the oil before their first contact with $CO_2$. Nevertheless, recovery factor was of 37.3% at 2,100 psig, and 43.6% at 3,100 psig. Again, these are low for $CO_2$ flooding in a clean, homogeneous, high permeability sandstone.

The reason for the poor performance is that we were not flooding a homogeneous system. The presence of a hydraulic fracture with a permeability of several darcies (Figure 7), which is at least one order of magnitude higher than the high permeability Berea sandstone of 100 md. As a result, $CO_2$ will preferentially flow through the high permeability medium recreating the fracture, and not through the matrix; and oil production

will occur through vaporizing gas drive. This is confirmed by the characteristics of the oil produced, which in these experiments, as in the ones performed in organic rich shale, was light yellow; suggesting it was comprised only of the lighter ends of the dark oil used to saturate the samples. We present pictures and oil chromatography later in this chapter to support these claims.

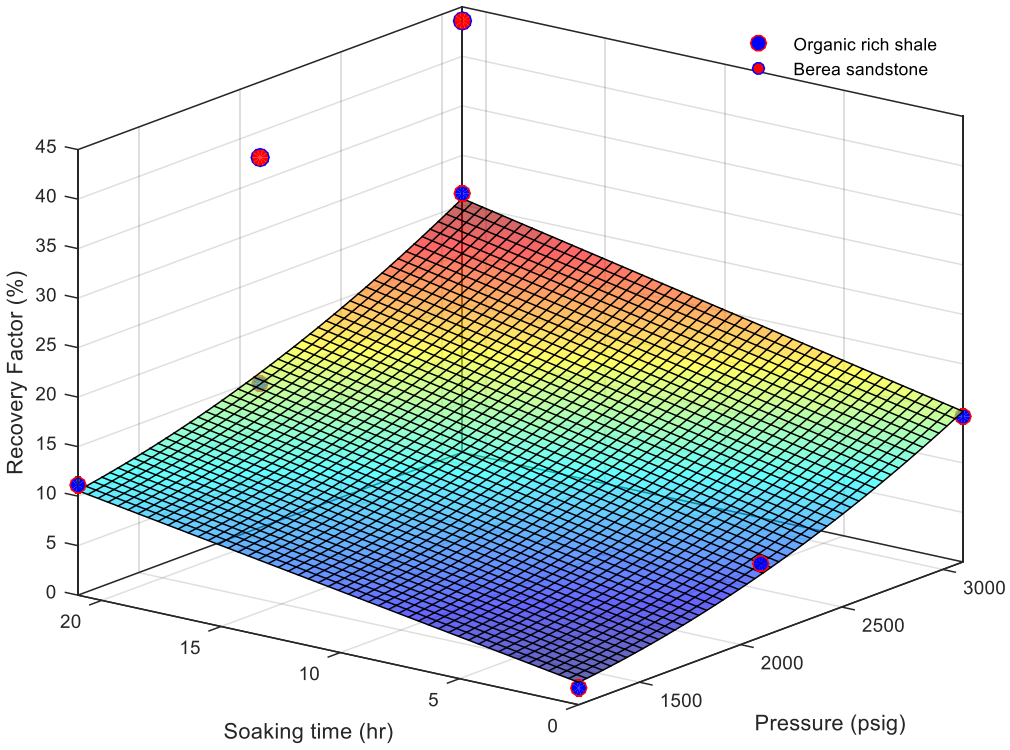


Figure 50 – Surface response of recovery factor as a function of pressure and soaking time for the second set of experiments performed with reservoir rock and crude oil from well 2 showing the results of the experiments repeated in 100 md Berea Sandstone. The slim tube MMP for this oil was 1,925 psig.

These observations are relevant because they suggest oil production is mainly controlled by the recovery mechanism, and that the transport properties of organic rich shales have less influence. This comes from the fact that increasing the rock permeability in several orders of magnitude increased the recovery from 39.9

to 156.7% (Figure 51). These increases are significant, but comparable, or even inferior, to the ones obtained because of pressure and soaking time increases (Figure 46Figure 47). This indicates that pressure and soaking time have more impact than transport, thus recovery is mainly controlled by the efficiency of the vaporizing-condensing gas drive taking place.

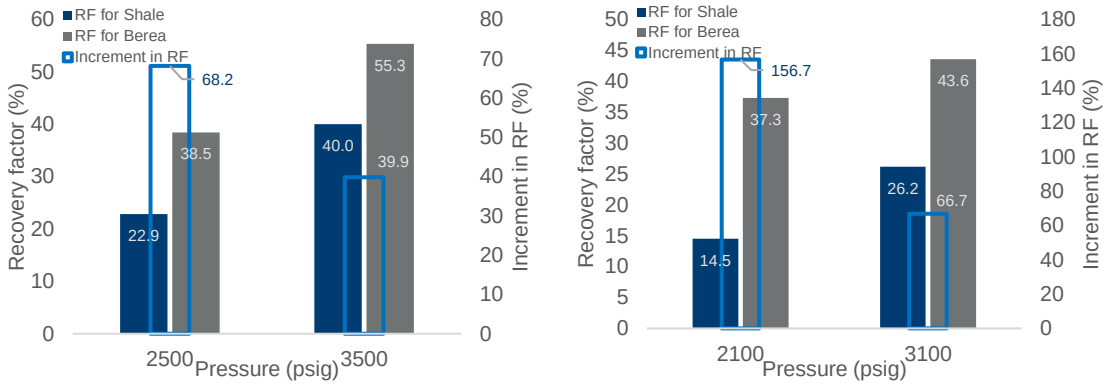


Figure 51 – Comparison of recovery factors obtained for organic rich shales and Berea. Left: experiments performed with 22 hrs of soaking time using crude oil from well 1, slim tube MMP for this oil is 3,706 psig. Right: experiments performed with 21 hrs of soaking time using crude oil from well 2, slim tube MMP for this oil is 1,925. All experiments are huff-and-puff.

Another interesting observation from the results in the Berea sandstone, is that increasing the pressure from 2,100 to 3,100 psig in runs 2.7 and 2.8 only increased recovery by 16.9%. This is significantly below the 80.69% increment between the equivalent runs performed in organic rich shale. Recall that these experiments used crude oil 2 with a slim tube MMP of 1,925 psig. We argued in the previous chapter that in organic rich shale operating pressure increments beyond the slim tube MMP do result in significant additional recovery. We see now that in Berea the additional recovery is not that significant. This is an indication that even when fluid transport through the matrix is not the main control on recovery, it affects the recovery mechanisms significantly.

CHARACTERISTICS OF THE PRODUCED OIL

The composition of the oil produced suggests peripheral vaporizing gas drive as the production mechanism. During all the gas injection experiments the crude oil recovered was significantly lighter than the one we used to re-saturate the core plugs. The injected oil during the saturation process was dark brown to black. In contrast, the oil produced was light yellow. This is evident in Figure 52, and it is true for both, experiments performed in organic rich shale and in Berea sandstone. In the image, all the effluents are considerable lighter in color than the injected oil. Moreover, we can see that the oil recovered at a lower pressure (number 4) is lighter than the one extracted at a higher pressure (number 2 and 3). This supports the relation between pressure and recovery. As pressure is increased $CO_2$ can vaporize more hydrocarbon components and therefore recovery is increased.

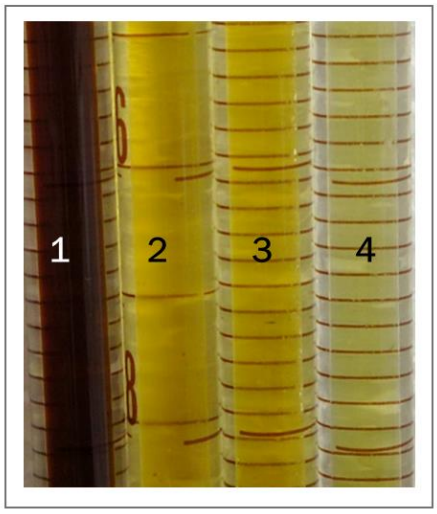


Legend

(1) Crude oil 1. Used for the re-saturation of the cores in runs 1.1 to 1.4.

(2) Oil recovered in test run 1.1. This run used shale sample 1, soaking time of 22 hr, and pressures of 2,500 and 3,500 psig.

(3) Fraction of the oil recovered in test run 1.4. This run used Berea sample 1, soaking time of 22 hr, and pressures of 2,500 and 3,500 psig. This fraction contains oil recovered at both pressures.

(4) Fraction of the oil recovered in test run 1.4. This run used Berea sample 1, soaking time of 22 hr, and pressures of 2,500 and 3,500 psig. This fraction contains oil recovered only at 2,500 psig.

Figure 52 – Comparison of the appearance of the injected oil and produced oil in experiments performed with crude oil 1. Note that the injected oil (1) is much darker than any of the oil recovered from the experiments (2,3 and 4).

Oil composition determined by gas chromatography is presented in Figure 53. We have included the compositions of the original crude oil 1, and its composition after it was doped with 5% wt. of iodobenzene.

Both compositions are almost identical as we would expect since the chromatography was meant to identify only the hydrocarbon components. The re-saturation of the core plugs was done using the doped oil, and we discuss the reasons for this in a later section within this chapter. We used dead oil in our work, which explains the low content of light ends ($C_2$ to $C_5$).

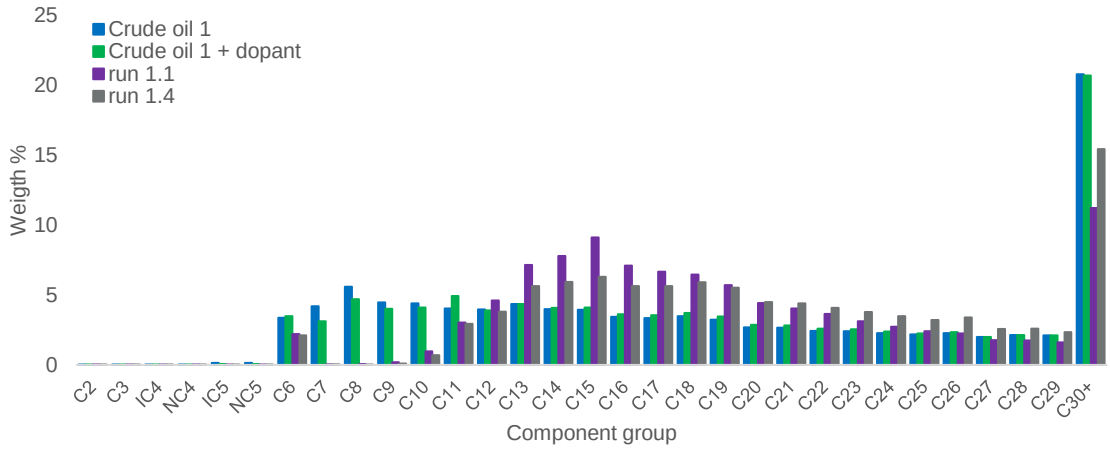


Figure 53 – Oil composition of the crude oil 1, the doped crude oil 1 and the effluents from test run 1.1 and test run 1.4.

In Figure 53 we observe the oil produced during the experiments, both in Berea and in organic rich shale, lost some intermediate components ($C_7$ – $C_{10}$). We believed these components were dragged by the gas phase when flashed at room conditions, and therefore were not recovered. It is evident that the oil recovered during runs 1.1 and 1.4 is lighter than the injected oil, as it has a higher concentration of intermediates ($C_{12}$ – $C_{22}$), and a lower concentration of the heavy ends ($C_{30+}$). This is a consequence of the mechanism of production being a vaporizing gas drive, in which the hydrocarbons recovered depend on which fractions can be vaporized into $CO_2$ at a given pressure. The higher the pressure, the higher the number of components that can be vaporized.

Interestingly, the composition of the oil recovered during test run 1.1 and 1.4 are not the same. Both runs consisted of three cycles of 22 hours of soaking time at 2,500 psig, followed by three more of such cycles at 3,500 psig. The only difference between those two experiments was that test run 1.1 was performed using an organic rich shale core plug and test run 1.4 was performed using a Berea sandstone of 100 md. We attribute the difference to the low transport in the shale, that as we will point out later it slows down and impairs the vaporizing gas drive process.

## NITROGEN INJECTION THROUGH A HYDRAULIC FRACTURE IN ORGANIC RICH SHALE

Organic rich shale samples from well 2, saturated with their corresponding crude oil were used in two experiments with nitrogen. In this case, each experiment was performed at two pressure steps. A huff-and-puff like injection with a soaking time of 21 hours was used in all tests with Nitrogen. Each pressure step was continued until the incremental oil recovery factor between two consecutive huff-and-puff cycles was less than 2%. A summary of the experimental conditions and results can be found in Table 15, and a graphical representation of the experimental conditions for all experiments performed with crude oil and organic rich shale core plugs from well 2, with nitrogen and carbon dioxide, are presented in Figure 54.

| Test run | Sample | Soaking time (hr) | Pressure (psig) | Recovery factor (%) |
|---|---|---|---|---|
| 3.1 | 7 | 21 | 3,100 | 0 |
| 3.1 | 7 | 21 | 3,750 | 0 |
| 3.2 | 10 | 21 | 4,500 | 0 |
| 3.2 | 10 | 21 | 5,000 | 0 |

Table 15 – Experimental conditions and results for Nitrogen injection in organic rich shales. All the experiments were performed at the reservoir temperature of 165 ˚F.

The experimental pressures for the runs using nitrogen were 3,100, 3,750, 4,500 and 5,000 psig. The lowest experimental pressure for nitrogen corresponds to the highest used with carbon dioxide in shale cores and

with crude oil from well 2. However, no recovery was obtained with nitrogen. This was unexpected given the high experimental pressures.

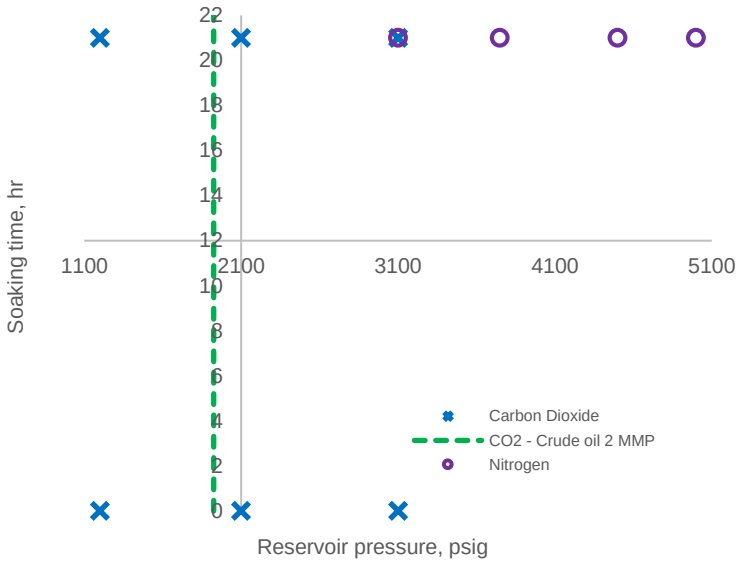


Figure 54 – Experimental matrix showing the tests performed with Nitrogen and Carbon Dioxide using organic rich core plugs and crude oil from well 2. The line is the CO2 – Oil slim tube MMP of 1,925 psig. All the experiments were done at the reservoir temperature of 165 ˚F.

Miscibility is harder to reach with nitrogen. MMP with nitrogen is roughly double the $CO_2$ MMP. That would put the MMP with nitrogen for crude oil 2 around 4,000 psig. However, we exceeded this value by 1,000 psig and still observed no recovery. Conversely, when we performed $CO_2$ huff-and-puff with 21 hours of soaking time at 1,200 psig, 725 psig below the $CO_2$ MMP, we still recovered 9.54% of the oil. This suggests that the low transport properties of the rock affect the miscibility process setting the effectivity of carbon dioxide and nitrogen even further apart than they are in conventional reservoirs.

It is evident from the results with nitrogen that its use for EOR in organic rich shales will likely be ineffective. However, this will ultimately depend on the oil composition and will be related to the MMP with nitrogen. Moreover, this is also discouraging for the application of dry gas, which also exhibit a MMP

larger than $CO_2$. This is unfortunate given that hydrocarbon gases are widely available in the oilfield. Yet the use of ethane would yield better recovery than carbon dioxide due to its lower MMP with crude oil, but its application may be limited by economics. An alternative would be the enrichment of methane with ethane, hydrogen sulfide, or other gases that lower the MMP; therefore, improving the vaporizing gas drive mechanism.

## COMPOSITIONAL CHANGES

During the first stage of this investigation, described in Chapter III, we showed that the use of a CT-scanner enabled us to track the changes of saturation or composition within the core as a function of time. Such changes are evident from direct observation of the color variations in the images (Figure 12), and from plotting average CT number as a function of time for the whole core sample (Figure 13). In this section, we will expand on the understanding of the capabilities of CT-scanning to observe what is taking place within the core plugs during the experiments.

We start by introducing the use of dopants to improve the contrast between the gas and the oil. We follow that by a discussion of the changes in compositions observed in the experiments performed using the organic rich core plugs re-saturated in the laboratory. Later, we present the limitations in the analysis of CT number, and we will finish by offering a more detailed examination of the changes in composition in specific areas of the cores that will enable a wider understanding of the recovery mechanisms taking place.

### The use of dopants to improve the visualization of compositional changes

In chapter III we presented images and plots that show the CT-scanner is sensitive enough to capture the saturation or composition changes in core-flooding like experiments using organic rich shale. It accomplishes this by tracking changes in the density of the materials. Therefore, there must be noticeable differences between the densities of the fluids involved to take advantage of CT-scanning technology. We

showed that when we inject $CO_2$ to displace oil at low pressure the CT-number decreases, whereas at high pressure it increases (Figure 13). This is explained by the strong dependence of the density of $CO_2$ on pressure, compared to that of oil. The density of oil changes little with pressure (Figure 14). But depending on the experimental pressure, the $CO_2$ density can be lower, similar, or higher, than the oil density. If the density of the $CO_2$ injected is similar than the density of oil, the CT-scanner will not be able to see the changes of compositions, nor saturations, because there will be no changes in density.

During the proof of concept presented in Chapter III, we deliberately chose the pressure conditions to ensure enough difference between the density of oil and $CO_2$. Yet that approach, if effective, prevents us from running tests within the range of pressures where there is not enough contrast. To eliminate that limitation, we introduced a dopant, or tracer, in the experiments we performed using re-saturated organic rich shale core plugs. The fact that we re-saturated the core plugs in the laboratory enabled us to place the dopant in the oil before starting the saturation process.

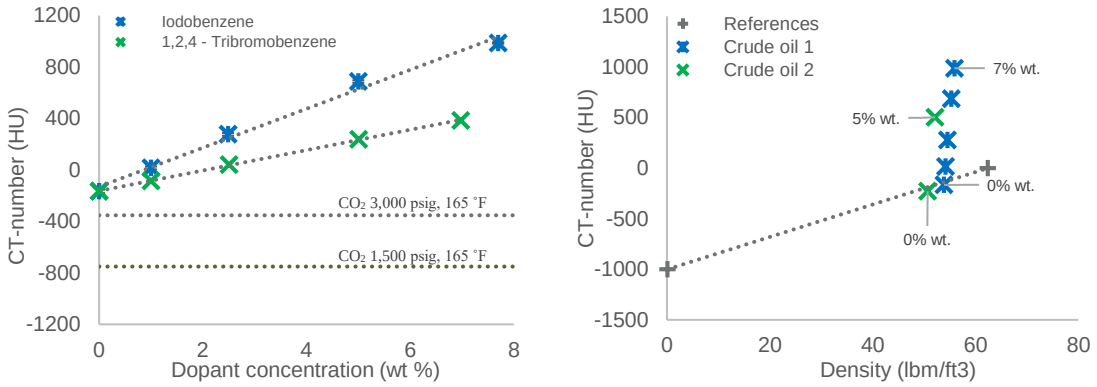


Figure 55 – Effect of the dopants in the CT-number and density of the crude oils 1 and 2. Left: CT-number as a function of dopant concentration for crude oil from well 1, showing two different dopants: Iodobenzene and 1,2,4 – Tribromobenzene. Right: CT-number as a function of density for the crude oils from wells 1 and 2.

Two dopants were considered, Iodobenzene and 1,2,4-Tribromobenzene. Figure 55 shows a plot of CT-number as a function of dopant concentration for both tracers using crude oil 1. Iodobenzene was found to

cause a higher increase in CT-number when compared to 1,2,4-Tribromobenzene at the same concentration. The same plot shows the estimated CT-number for $CO_2$ at 1,500 psig and 3,000 psig. We selected Iodobenzene in a concentration of 5% wt. to dope crude oils 1 and 2.

The dopants change the CT-number of the oil without causing significant alterations to its density. Figure 55 also shows a plot of CT-number as a function of density. As a reference, the CT-numbers for air (-1,000 HU) and water (0 HU) are also displayed connected with a line. Such line defines the Hounsfield scale. The relation between the CT-number and the density of most materials fall within that line. The same plot shows the CT-number as a function of density for crude oils 1 and 2, with and without dopant. The relation between CT-number and density for both oils without dopant is perfectly defined by the line representing the Hounsfield scale. However, as dopant is added to the oil, the oil CT-number increases disproportionally to its density. We take advantage of this property of dopants to increase the contrast between the oil and the gas injected in our experiments.

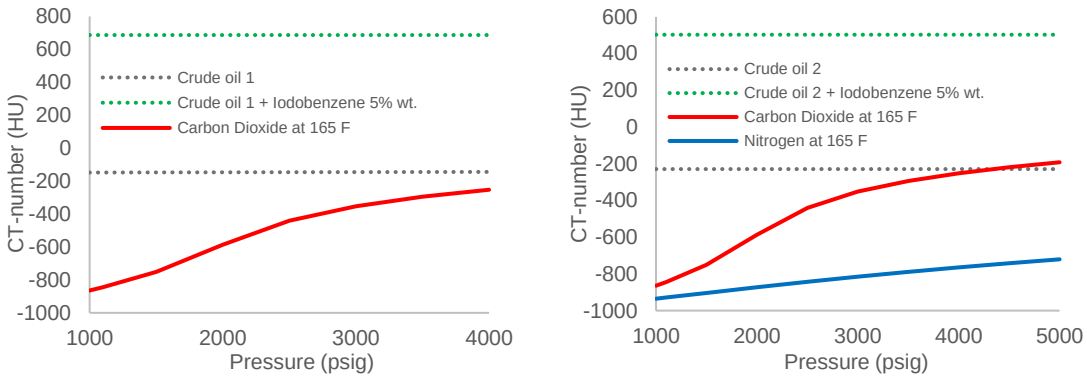


Figure 56 – CT-number as a function of pressure. Left: effect of the addition of 5% wt. iodobenzene in crude oil 1 and CT-number contrast with $CO_2$. Right: effect of the addition of 5% wt. iodobenzene in crude oil 2 and CT-number contrast with $CO_2$ and $N_2$.

The relevance of the use of a dopant is illustrated by Figure 56. We show the CT-number as a function of pressure for carbon dioxide and nitrogen estimated from their density, using air and water as references for

converting to the Hounsfield scale. The same figure shows in grey the CT-number for crude oil 1 and 2 without dopant, and in green the CT-numbers after the addition of the dopant. Oil CT-numbers were measured in the laboratory at room pressure, and their variation with pressure is not significant and it was neglected. The plots clearly show that as pressure increases, the difference between the CT-numbers of carbon dioxide and crude oil is significantly reduced because of the rapid increment in the density of $CO_2$. Nevertheless, it is also illustrated how we maintained a significant CT-number contrast by the addition of the dopant.

**Compositional changes with time**

The oil composition changes with time because of gas injection. The use of CT-scanning imaging during our experimental work gave us the advantage of being able to track such changes in composition. The change in CT-number with time is meaningful, even considering the small overall change in density taking place. Most of the core is comprised by the rock grains, which are not expected to change density nor composition during the experiment. So, we are looking at changes occurring within the pore volume, which for most samples is below 10% of the bulk volume. Such changes, are caused by the variations in composition caused by injecting gas. As lighter components are stripped out of the crude oil, its density, and therefore its CT-number increases. Nevertheless, there is $CO_2$ simultaneously penetrating the pore volume and being dissolved into the crude oil; and this results in a reduction of CT-number.

Figure 57 shows the change in the average CT-number of the entire core sample as a function of time for all the experiments performed with organic rich shale using carbon dioxide as injectant. The CT-number decreases as a function of time as the effect of the $CO_2$ entering the sample and dissolving into the oil generally outweighs the influence of the vaporization of the light oil components from the crude oil into the gas. The degree of reduction in CT-number is better used as a qualitative indication of changes in composition and not as a quantitative magnitude to compare the outcome of different experiments. The

reason for this is that the degree of change in CT-number is affected by the pore volume of the rock and the experimental pressure, which controls the CT-number of the injected gas.

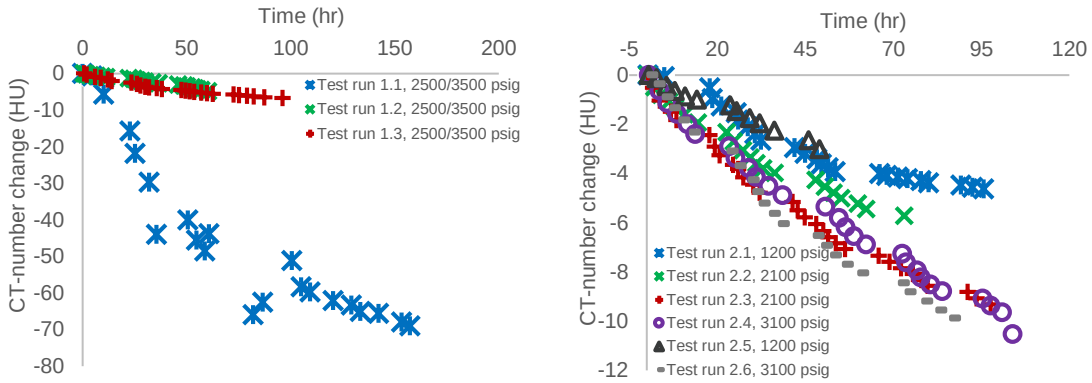


Figure 57 – Change in CT-number as a function of time. Left: first set of experiments using oil and organic rich shale cores from well 1. Right: second set of experiments using the cores and the oil from well 2. Only experiments performed with carbon dioxide in organic rich shale cores are displayed in these plots.

Core plugs with a higher pore volume will have more room to store oil inside them, and therefore, they will have more potential to show changes in CT-number as the oil and the pore space are invaded by $CO_2$. Also, they will have more surface area to store $CO_2$ in a sorbed state. Nonetheless, the change in the oil density depends on the density of the gas injected, which is a function of both the composition of the gas and the pressure of the experimental run. Another important factor is whether the oil has been doped or not. Thus, the change in CT-number is related to the recovery factor, but such relation is not straightforward. The impact of pore volume is well illustrated by Figure 58. Test run 2.8 performed in a Berea sandstone with the same oil and at the same pressure than test run 2.4 presents a much bigger decrease in CT-number. The other plot in Figure 58 shows there is some relation between the change in CT number and the recovery factor, however such relation is somehow scattered because of differences in factors such as pore volume and experimental pressure. It is probable that the CT-number change could be normalized to make more accurate predictions of recovery factors. However, we are not going to make efforts in such direction since we have

already quantified recovery factors by mass balance. Instead, we will focus in the qualitative analysis of the behavior of CT-number.

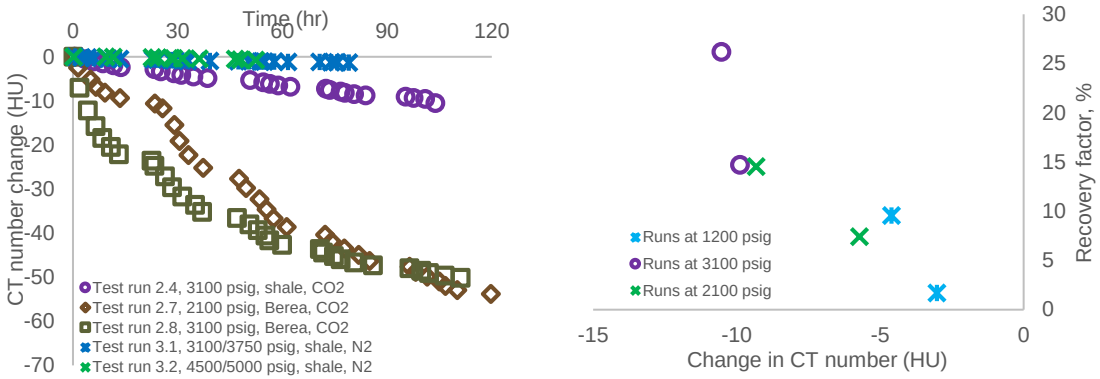


Figure 58 – Left: Comparison of CT-number a as a function of length for experiments performed with $CO_2$ in organic rich shale and Berea, and experiments performed using $N_2$ in organic rich shale. Right: relation between recovery factor and change in CT-number; the points of similar color and different recovery factor correspond to different soaking times. All the experiments are using crude oil from well 2. All organic rich shale cores in these experiments are from well 2.

**Compositional changes in space**

We just addressed the change of the average CT-number of the entire core sample with time. Yet, looking at how these changes happen in different regions inside the core gives a deeper understanding of the recovery mechanisms and how composition changes. Figure 59 presents the total CT-number change as a function of core length during the experiments performed with $CO_2$ and organic rich shale core plugs. The image was created by separating the core in slices of 0.33 mm in thickness along its length, and then subtracting the final CT-number for each slice from the initial CT-number.

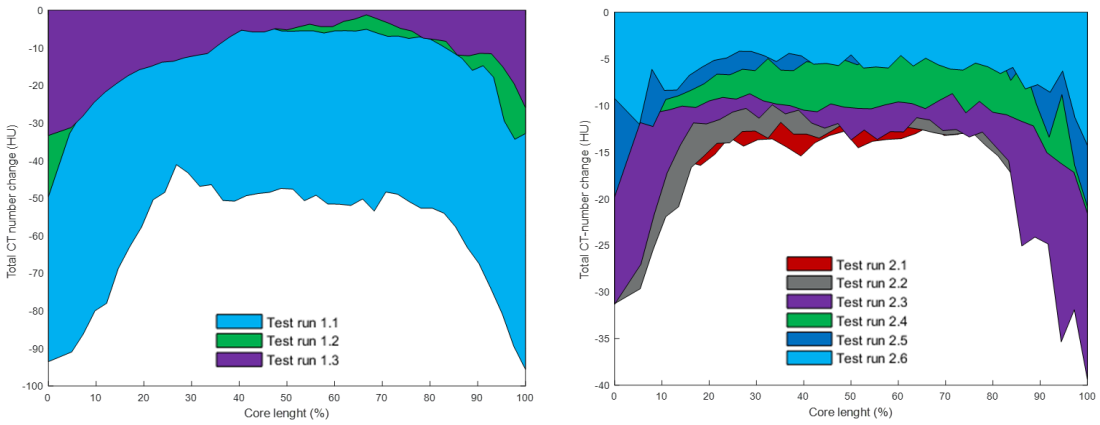


Figure 59 – Total CT-number change as a function of length. This is the CT-number at the end of the experiment minus the CT-number at the beginning as a function of length. Left: first set of experiments, oil and core plugs from well 1. Right: second set of experiments, oil and crude oil from well 2.

Figure 59 reveals the influence the transport properties have in the process. They significantly slow down the movement of $CO_2$ inside the core. The image on the left corresponds to the first set of experiments, using cores and crude oil from well 1. The one on the right, depicts the second set of experiments, using core and crude oil from well 2. We can tell that after several days of $CO_2$ exposure, the gas was not able to reach the center of the core to the same degree than it reached the edges. This implies that the mass transfer between the carbon dioxide and the crude oil is significantly impaired by the poor transport properties. Notice that in test run 1.1, $CO_2$ reached deeper into the core than it did in any other run. This is because test run 1.1 was performed with sample 1, which has the highest porosity and permeability among the samples (Table 10, Figure 21, Figure 39). Also, this test reached the highest pressure. Nevertheless, the permeability of sample 1 was still low enough to cause $CO_2$ to affect the edges of the core more than the center.

The change in CT-number as a function of length and time is presented for test run 2.4 in Figure 60. The image shows how the CT-number is even along the length of the core at the initial time, and then it starts to decrease because of the compositional changes. As time moves forward, the decrease of CT-number becomes more pronounced towards the edges of the core, further confirming the role of the transport properties of the core sample on recovery. This reflects how the poor transport prevents the $CO_2$ from

contacting the oil deeper into the core, as it slows down its advance when compared to a conventional reservoir.

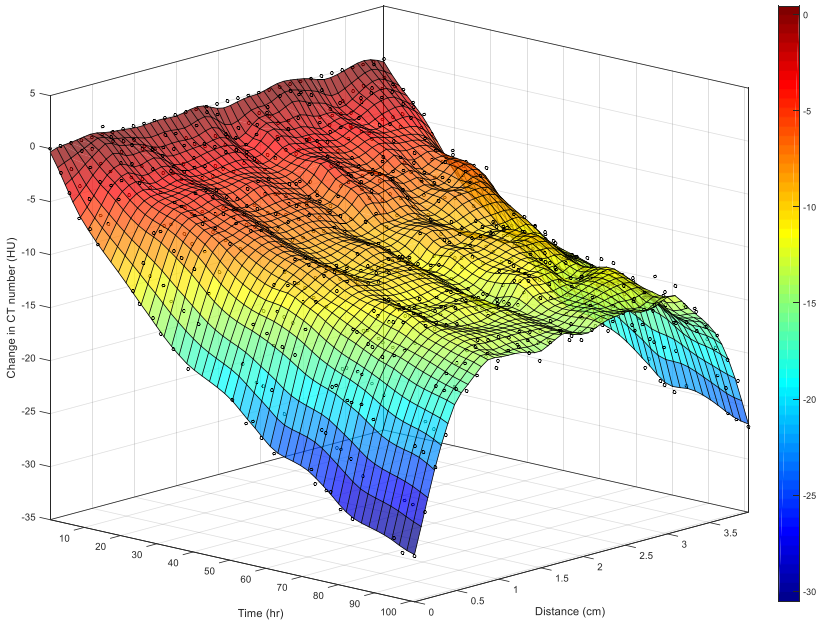


Figure 60 – Change in CT-number as a function of length and time for test run 2.4

The observations made from the ends of the cores can be extended by looking at the radial changes of composition in the middle of the core. To build Figure 61, we dismissed the ends of the core and focused instead on the middle section. This means that from the total length of the sample, we ignored approximately one centimeter on each side. The remaining core was used for the analysis. We did this to observe what happens radially far from the ends of the core. After the middle section was separated, the core was averaged along its length, so the total length of the core was represented by only one slice, or length unit. This was repeated for each time. Figure 61 shows the change in CT-number from the first time step to the last time step in the test run 2.6.

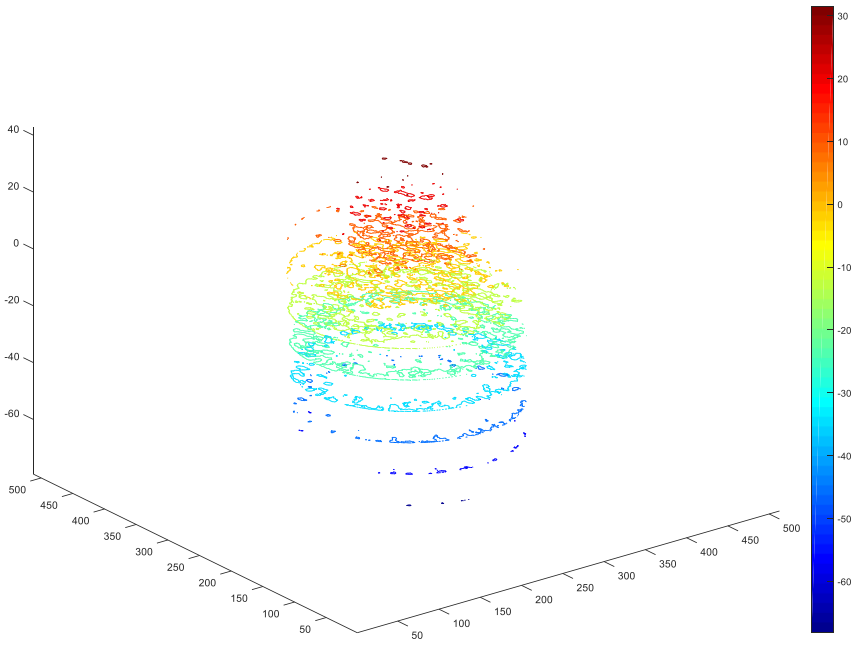


Figure 61 – Total areal change in CT-number for the center of the core during test run 2.6. This run was performed using $CO_2$ and organic rich shale.

Figure 61 also shows a more pronounced reduction on CT-numbers towards the edges, in agreement with Figure 59 and Figure 60. Yet, now we also see that CT-number has the opposite trend towards the center of the core. The increase of CT-number in the center implies that density is increasing. This can be explained by the existence of a peripheral slow-kinetics vaporizing-condensing gas drive. We can divide the core radially, starting from the edge and moving towards the center in three regions. An external region, a central region, and internal region. The external region shows a net decrease in CT-number and density, because the density reduction caused by the dissolution of $CO_2$ into the oil has outweighed the density rise produced by the vaporization of the lighter oil components into gas in the fracture. The central region shows no net change in CT-number. This is because the decrease in density caused by the dissolution of $CO_2$ into the oil is equivalent to the density rise produced by the vaporization of the lighter components of the oil into the gas. And finally, the internal region, which presents a net increase in CT-number because not enough $CO_2$

has dissolved in the oil in this region yet, thus the increase in density caused by the vaporization of lighter components outweighs the reduction of the density produced by the dissolution of $CO_2$ into the oil.

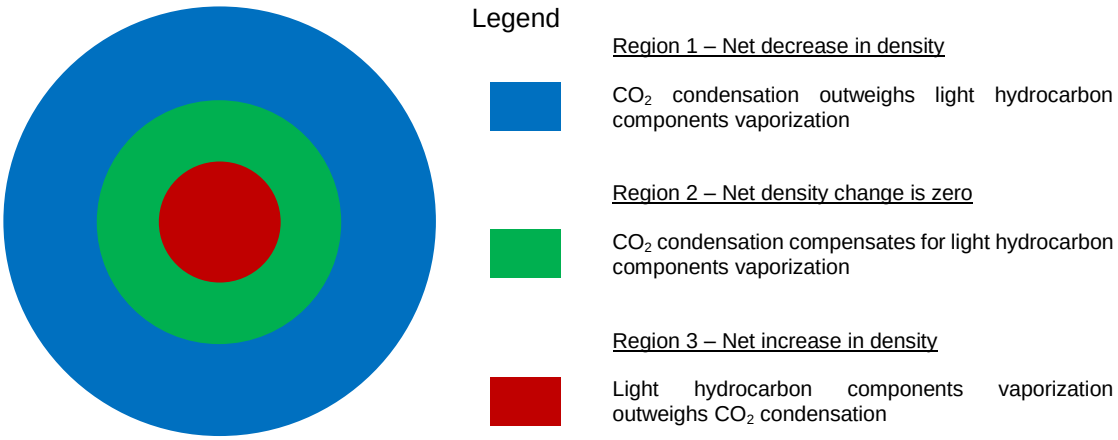


Figure 62 – Schematic representation of the regions observed during a slow-kinetics peripheral vaporizing-condensing gas drive process. The image represents a cross section of a core plug.

To better capture the influence of transport properties in the production mechanism, we can compare Figure 59 with Figure 63. The latter shows the total CT-number change as a function of length for the experiments performed in Berea sandstone of 100 md in permeability. It is possible to see how in the case of the Berea, the $CO_2$ can penetrate the totality of the core length causing a consistent change in CT-number, and therefore density, along the core.

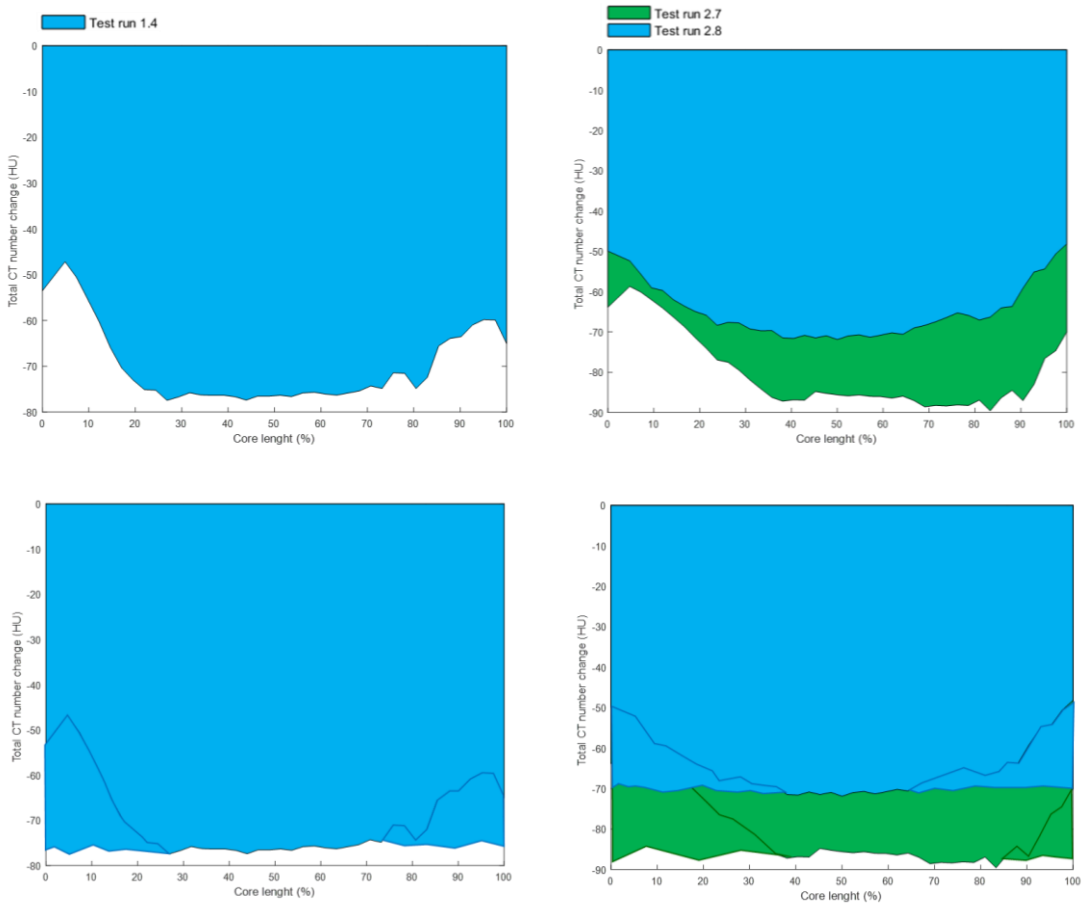


Figure 63 – Total CT-number change as a function of length for the experiments performed using Berea sandstone. Upper left: Test run 1.4 performed using crude oil from well one. Upper right: test runs 2.7 and 2.8 performed using crude oil from well two. Lower left: Test run 1.4 corrected by delay in initial CT-number capture. Lower right: Tests runs 2.7 and 2.8 corrected by delay in the capture of the initial CT-number.

This is true for all the experiments carried out using 100 md Berea sandstone. The images on the top are the result of processing the data captured by the CT-scanner in the same manner as we did in the case of Figure 59. However, they give the impression that the changes in CT-number are higher in the center of the core than they are at the edges. This is not the case. Such effect is an artifact resulting from the experimental procedure. At the start of the experiment, the oil-saturated core plug is inside the core-holder under confining pressure, at reservoir temperature, and under vacuum. Then, $CO_2$ is progressively injected and the pressure is increased until the target experimental pressure is achieved. This process of pressure increment takes approximately 30 minutes. After that, the CT-scanner is warmed up, which adds around 5 more minutes,

and the first scan is performed. Due to the good transport properties of the Berea sandstone, by the time the first scan is performed, the $CO_2$ has already affected the edges of the core, resulting in the observed artifact. To reduce our exposure to X-rays it is not possible to scan while we are inside the scanning room increasing the experimental pressure.

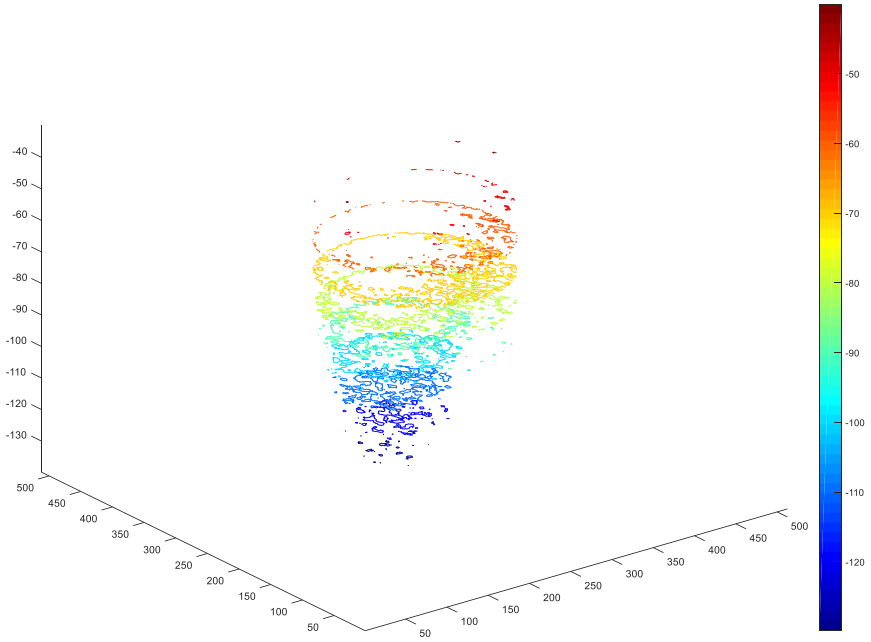


Figure 64 – Total areal change in CT-number for the center of the core during test run 2.8. This run was performed using $CO_2$ and Berea sandstone.

The images in the lower part of Figure 63 show what we would observe if the pressure could be increased instantaneously, and the first scan performed simultaneously. A consistent, homogeneous vaporization-condensation drive. To further support this argument, Figure 64 directly contrast what we see in Figure 61 and Figure 62. Considering again that the edges are affected by the early vaporization not captured by the CT-scanning process, $CO_2$ is able to penetrate and affect the entire pore volume. The zones we defined in

Figure 62 are no longer present. The rapid velocity of penetration of $CO_2$ into the Berea matrix as compared with the observations made in organic rich shale constitutes the defining argument behind the slow-kinetics vaporizing gas drive process.

## THE PERIPHERAL SLOW-KINETICS VAPORIZING GAS DRIVE AS A RECOVERY MECHANISM

The determination of the minimum miscibility pressure using the slim-tubing technique is designed to measure the minimum pressure at which miscibility is accomplished through a multiple-contact process at reservoir temperature (Adel, Tovar, and Schechter 2016). In such case, the gas injected does not develop miscibility with the oil at the first contact, but a mass transfer process takes place between the gas and the crude oil. As a result, a fraction of the light and intermediate components from the crude oil are vaporized into the gas, making the gas richer through a process known as a vaporizing gas drive. In this way, the gas injected will continuously change its composition and will eventually reach a concentration of light and intermediate components that makes it miscible with the oil.

Vaporizing gas drive is regarded as the main mechanism for developing miscibility when a lean gas is injected into a crude oil. However, a condensing gas drive takes place simultaneously. The condensing gas drive implies the dissolution of the injected gas into the crude oil, bringing the crude oil composition closer to that of the injected gas, and therefore, contributing towards the development of miscibility. Which ultimately, implies the existence of only one phase. The condensing and vaporizing gas drive mechanisms, and ternary representations of such, have been previously described by Stalkup (1983) and Lake (2010). We will make use of such representations to explain how the low transport capacity of the organic rich shale is a defining factor on recovery.

The ternary diagram presented in Figure 65 is a vaporizing gas drive process of multiple-contact miscibility. In the diagram, the complex composition of the crude oil and the injection gas are simplified and represented as only three components. The upper vortex represents the injection gas, the bottom left vortex represents

the heavier components of the crude oil, and the bottom left vortex the intermediate components. The light gray lines connect points of similar concentration of such components. The blue line encloses the two phases region, and the dotted lines inside it, are tie lines whose ends represent the composition of the equilibrium phases.

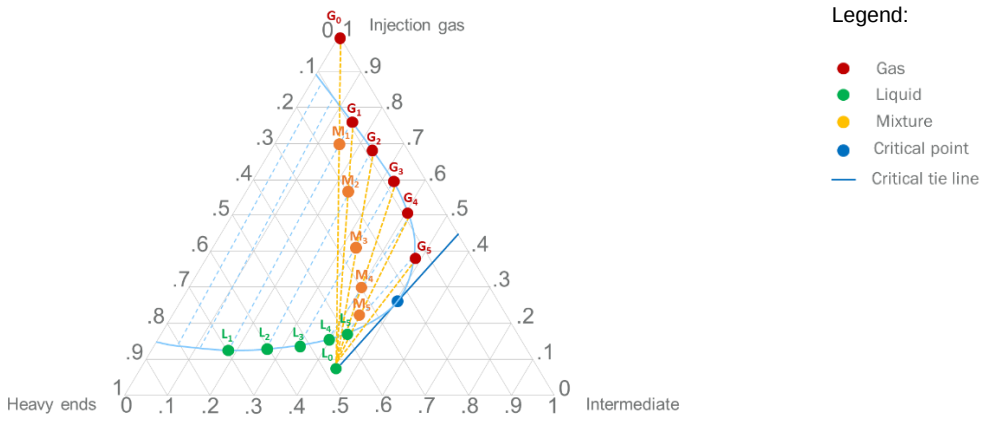


Figure 65 – Ternary diagram showing a multiple contact miscibility process reached by vaporizing gas drive.

When the gas ($G_0$) is injected in the slim tube, it contacts the crude oil ($L_0$). Miscibility does not occur at this first contact, and therefore, two definite phases remain. However, the compositions of both the oil and the gas change. The gas is enriched in intermediate crude oil components, creating a new gas of composition ($G_1$), and simultaneously, some of the injection gas is dissolved into the oil to create a liquid with a new composition ($L_1$). Since the gas mobility is higher than the crude oil mobility, the new gas ($G_1$) can contact fresh oil ($L_0$) resulting in a new gas ($G_2$) and a new liquid ($L_2$). ($G_2$) is richer in hydrocarbon components than ($G_1$) and ($G_0$). This process continues, and after multiple contacts the compositions of the liquid and the gas meet at the critical point, and miscibility is reached.

In a slim tube, the vaporizing gas drive mechanism acts at the interphase between the injection gas and the crude oil to eliminate such interphase, and promote instead the existence of a mixing zone with a

compositional gradient. The upper zone of the slim tube will be saturated with the injection gas, but as we move down along the coil, the concentration of hydrocarbon components will be increasing continuously, until a point is reached at the bottom of the coil where it is saturated with only crude oil. This mixing zone sweeping along the slim tube is what permits the achievements of recovery factors close to 100% by maximizing the displacement efficiency through of the complete elimination of capillary forces in the absence of an interphase.

There are mainly two reasons why we do not reach the high recovery factors observed in a slim-tube experiment. The first deviation from the ideal slim-tube process is caused by the presence of the hydraulic fracture. This effect is highlighted in the experiments performed in Berea sandstone where the recovery factor was under 60% in all cases; even when the experimental pressure was significantly above the MMP (Table 14, Figure 49, Figure 50). The reason for the low recovery factor, is that the miscible front does not sweep through the core. During the slim-tube experiment, and in conventional core-flooding, the gas injected flows through the matrix, forcing the miscible front to sweep the porous media displacing close to the totality of the crude oil because of the low capillary forces. When a hydraulic fracture is added to the system, the gas is no longer forced to flow through the rock matrix. This is still true for the experiments performed in Berea, because even when the permeability of the rock is of 100 md, the permeability of the fracture is estimated to be of several darcies. Therefore, there is no miscible front sweeping through the core, which significantly impairs recovery. Instead, the gas remains in the periphery of the Berea core and the miscible front is developed in a peripheral fashion (Figure 66). Recovery in this case relies solely on the ability of the injected gas to strip out the lighter components of the oil, as governed by Figure 65, and transport them outside the core-holder.

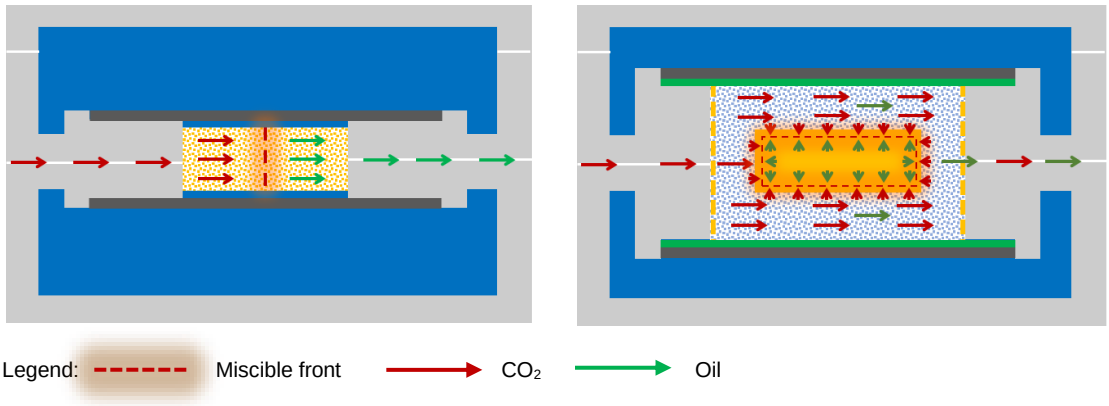


Figure 66 – Comparison of a conventional miscible front and a peripheral vaporizing gas drive process

The second factor that separates us from conventional core-flooding behavior is the poor fluid transport ability of the organic rich shale. We have already shown that the low transport properties significantly slow down the mass transfer between the injected gas and the crude oil using the analysis of CT-scanning data (Figure 61). Figure 67 shows the progression of a huff-and-puff injection process in an organic rich shale reservoir. The ternary diagram on the left corresponds to the first cycle of injection. During the soaking period, multiple contacts of mass transfer will take place and the gas in the fracture becomes richer in light and intermediate hydrocarbon components, changing its composition from ($G_0$) to ($G_3$). Due to the slow kinetics, the content of hydrocarbons of ($G_3$) is lower than what it would be reached during the same period in a high permeability rock such as a Berea. This is because the enrichment of the gas is cut short when production happens. For the second huff-and-puff cycle, represented by the ternary diagram to the right of Figure 67, the composition of the injected gas is similar than the one injected in the previous cycle, but the composition of the crude oil has changed. The oil has become richer in heavier components because of the oil produced during the previous cycle. This implies that in a similar period, if the cycles are of the same length in soaking time, the gas ($G_3$) will have a lower content of light and intermediate hydrocarbon components than in the first cycle, and therefore, less oil will be produced. As more production cycles are performed, ($G_3$) will get leaner and leaner, until no more oil is recovered.

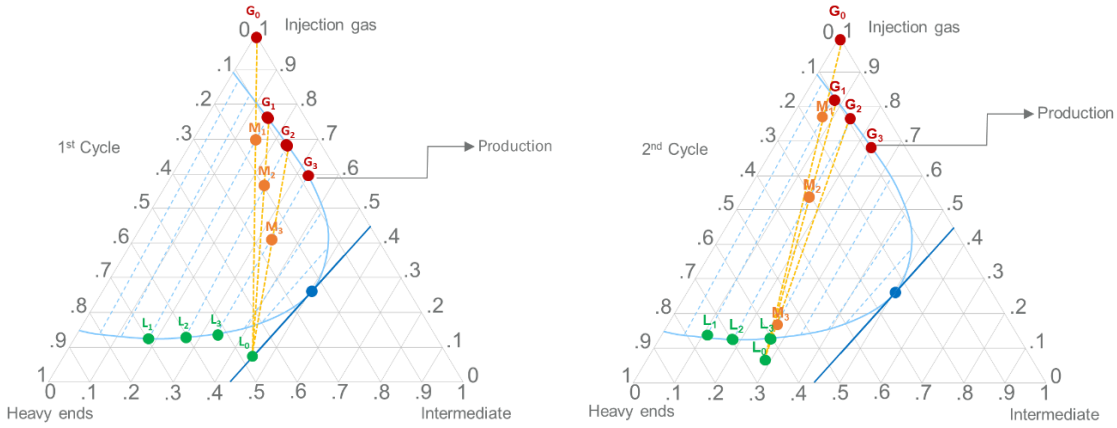


Figure 67 – Ternary representation of the peripheral slow-kinetics vaporizing gas drive in a huff-and-puff gas injection process in organic rich shale.

When continuous injection is implemented, the peripheral slow-kinetics vaporizing gas drive is less effective because the enrichment process is being continuously disrupted. Figure 68 shows a ternary representation of the peripheral slow-kinetics vaporizing gas drive process for the case of a continuous injection. The diagram to the left of Figure 68 shows the injection of a lean gas that vaporizes light and intermediate components from the oil, and changes its composition from ($G_0$) to ($G_1$), however, in contrast to what was presented in Figure 67 for the huff-and-puff process, in this case the gas phase is not able to continue the enrichment process and reach a composition such as ($G_3$). This is because the gas is continuously being produced and replaced by new lean gas, which represents a constant disruption of the enrichment process.

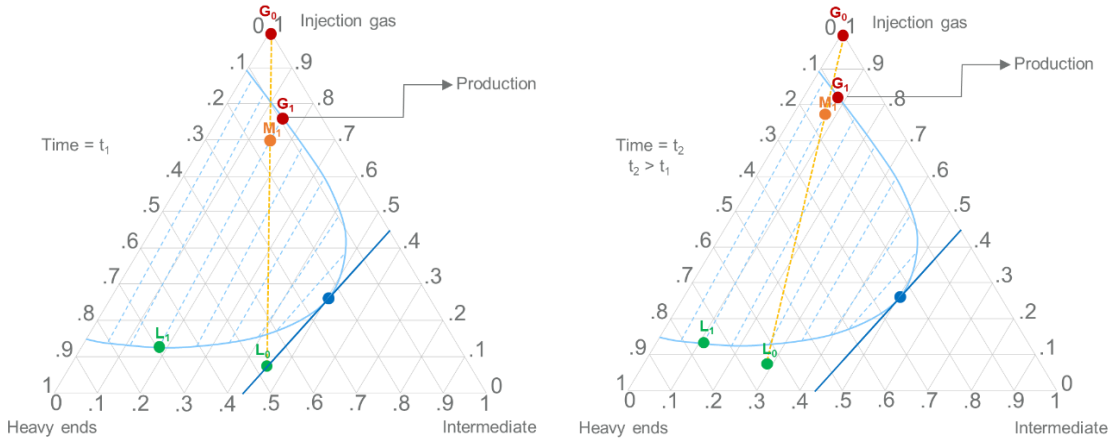


Figure 68 – Ternary representation of the peripheral slow-kinetics vaporizing gas drive in a continuous gas injection process in organic rich shale.

As time goes by during continuous injection, the oil composition will change as lighter and intermediate components are stripped out by the gas. The ternary diagram to the right of Figure 68 represents the continuous injection process later in time. Because of the change in composition of the oil, the concentration of intermediate components in the gas phase decreases over time, until no more oil is produced. The constant disruption of the enrichment process therefore results in less oil production when continuous injection is implemented.

The experimental results showed that increasing injection pressure beyond the slim tube MMP continues to cause the recovery factor to rise. The reason for this is that even when a miscible front will not exist, a higher pressure implies that more hydrocarbon components from the oil can be vaporized at each contact by the injected gas. The effect of pressure over the peripheral slow-kinetics vaporizing gas drive is shown in Figure 69. At higher pressure, the two phases zone region becomes smaller inside the ternary diagram. At a pressure ($p_2$), the resulting gas composition ($G_1$) after the first contact is richer in intermediate components than the resulting gas composition ($G_1$) after the first contact at a lower pressure ($p_1$).

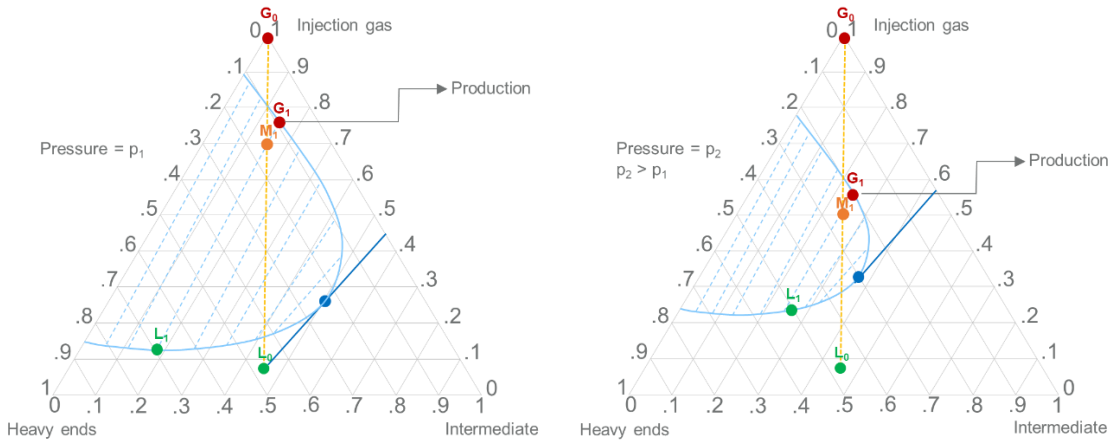


Figure 69 – Effect of increasing injection pressure during gas injection in organic rich shale

## SUMMARY

In this chapter, we have introduced the slow-kinetics peripheral vaporizing-condensing gas drive as the main recovery mechanism during gas injection for EOR in organic rich shale. There are two characteristics setting apart this mechanism, and causing reduction in efficiency, from the vaporizing-condensing gas drive in conventional rocks. The first one is that it is peripheral, and the second one is that it has slow-kinetics. The relevance of the peripheral aspect was highlighted during the experiments performed in Berea sandstone. These experiments resulted in low recovery factors, under 60%, even when the operating pressure was significantly superior than the slim-tube MMP. This is because when we inject through a fracture that has a permeability of at least one order of magnitude above the permeability of the Berea sandstone, the carbon dioxide does not flow through the rock matrix, but only flow through the fracture. Consequently, there is not a miscible front sweeping through the core sample and displacing oil under conditions of no capillary pressure, which is the reason behind the high recovery factors observed in slim-tube experiments and in conventional core-floodings. In our experiments, the mass exchange and the potential development of the miscible front are happening close to the borderline of the core sample, and it remains there, or slowly moves inwards. But does not sweep through the sample. Therefore, oil is not displaced, but vaporized. The volume

of crude oil recovered depends on the fraction of the oil that can be vaporized into the volume of gas in the fracture at the specific conditions of pressure and temperature. Such fraction will later be transported outside the core-holder as a part of the gas phase, where they will condense as the produced gas is flashed at room conditions.

The slow-kinetics aspect of the mechanism, causing the second step down in recovery efficiency, was highlighted by the CT-scanning data. During the experiments with organic rich shale, we observed a compositional gradient within the core that was still there after six days. This indicates the poor transport properties slow down the mass transfer between the injected gas and the crude oil. Inside the core, we observed three regions. An external region where density significantly decreased because $CO_2$ condensation outweighed the vaporization of the intermediate hydrocarbon components. A central region with no change in density, where the vaporization of hydrocarbon components and the condensation of $CO_2$ are equivalent. And an internal region, where density had increased since the vaporization of the hydrocarbon components outweighed the condensation of $CO_2$. Such regions are not present in the experiments conducted in Berea sandstone, where recovery is consistently higher. This is because when good transport enables efficient mass transfer, the volume of crude oil that is vaporized by the $CO_2$ is controlled by the phase behavior at the prevalent conditions of pressure and temperature. In other words, in Berea sandstone $CO_2$ vaporizes all the hydrocarbons that it can until thermodynamic equilibrium is reached. This is not the case for organic rich shale, because the poor transport slows down the process and thermodynamic equilibrium is not reached, meaning that there is thermodynamic potential for hydrocarbon vaporization that remains unused and it translates into lower recovery factors. This condition is of course exacerbated when continuous injection is implemented, explaining why huff-and-puff resulted in better recovery.

Thermodynamics, therefore, have an important role to play in this process. The volume of crude oil that can be vaporized depends on the volume and compositions of both the crude oil and the injection gas, and the conditions of pressure and temperature. And it also depends on the efficiency of the mass transfer process. From these variables, we only control the composition of the injection gas and the injection pressure. We

can maximize recovery by selecting a gas that vaporizes the most hydrocarbon components and operate at the maximum possible pressure. Vaporization of hydrocarbons increases with pressure for the gasses commonly used in EOR processes. The importance of the selection of the gas was made clear by the results of the experiments performed with nitrogen. Nitrogen has a higher slim-tube MMP than $CO_2$ because at any given pressure it can vaporize less hydrocarbon components than $CO_2$. The synergy of such unfavorable phase behavior with the poor mass transfer in the organic rich shale was lethal for the recovery process. Meaning that the poor mass transfer in organic rich shale exacerbates the shortcomings of nitrogen as an injection gas for EOR, and we should expect that it will do so also for methane.

The composition of the oil supports both, the peripheral, and the slow-kinetics aspect of the vaporizing-condensing gas drive mechanisms. The peripheral aspect is supported by the chromatography of the crude oil produced in the experiments performed in Berea sandstone. This oil was richer in intermediate components when compared to the oil injected into the samples. This is because the miscible front does not sweep the sample displacing the oil, but instead acts from the periphery stripping out only the components that can be vaporized into the gas, leaving the heavier components behind. The slow-kinetics is backed by the chromatography results for the oil produced in the experiments performed in organic rich shale. This oil had a lower concentration of heavier ends than the oil produced in the experiments performed in Berea. The poor transport interferes with the mass transfer process affecting mainly the heavier ends that are more difficult to vaporize and with larger molecular sizes that makes transport more difficult.

# CHAPTER VII

# FIELD INTERPRETATION OF LABORATORY RESULTS

This chapter discusses the results of our laboratory experiments from a field scale standpoint. The advantage of laboratory work is that it uses real reservoir fluids and rock; and are performed at the conditions of temperature and pressure existing in the reservoir. This provides a unique opportunity for the observation and understanding of mechanisms, and for the assessment of EOR processes and well treatments that are fundamental to select a proper exploitation technique. Experimental work is also the foundation for the development of models that are incorporated into numerical simulators to provide a mean for the evaluation of exploitation techniques in a field scale. After such models exist, laboratory data is still required to populate those models, and for calibration and validation. Once the models are calibrated to reproduce experimental observations, they can be scaled up for the evaluation of pilot projects or full field developments. In the case of organic rich shale, however, universally accepted models for storage, transport and phase behavior do not exist yet, and therefore there are no commercial numerical simulators that can be used for full field, or even pilot level evaluation. Interestingly, numerous works have been published in literature that use the models and simulators developed for conventional reservoirs to make predictions or to investigate mechanisms in organic rich shale reservoirs. The problem with this, is that we are not in a position to quantify the deviation resulting from the use of reservoir engineering models developed for conventional sandstones and carbonates, in organic rich shale, making the results of such investigation irrelevant. This situation places us in the position of making field development decisions based solely in laboratory data.

The problem with this is the scale of the physical simulations performed in the laboratory. Rock samples of a few inches in length and diameter are used to understand a process taking place in a reservoir that covers several hundreds of acres and with at least tens of feet in thickness. So, in the next sections we analyze and discuss the scale differences to draw realistic field performance expectations from the laboratory results.

VOLUMES AND TIMES

In the laboratory, the volume of the fracture is much bigger with relation to the volume of the reservoir rock than it is in the field. Meaning we will need in the field a longer period to dispense an equivalent amount of $CO_2$ with respect to the volume of reservoir rock or crude oil contained in it.

The total volume of $CO_2$ we injected in the laboratory was given by;

$$CO_2 \text{ vol.}_{lab} = \text{Number of cycles}_{lab} * (\text{Core PV} + \text{Fracture PV}) \qquad \ldots\ldots\ldots\ldots\ldots\ldots\ldots\ldots\ldots.. \quad 54$$

Note that we do not consider rock compressibility, nor the volume of $CO_2$ sorbed, to calculate the volume injected in the experiments using Eq. 54. This is justified because the pore volume of the core plug is significantly smaller than the one in the fracture. We assumed a porosity of 38 % for both the laboratory and the field fracture. The dimensions of the fracture for the field are assumed and they are presented in Table 16.

| | |
|---|---|
| Reservoir thickness (ft) | 400 |
| Fracture spacing (ft) | 200 |
| Proppant porosity (%) | 38 |
| Fracture half-length (ft) | 500 |
| Fracture width (in) | 0.5 |

Table 16 – Field fracture dimensions

In the slow-motion peripheral vaporizing gas drive process, the lighter and intermediate components of the crude oil are stripped out by the carbon dioxide, and then carried outside. This make both, the volume of $CO_2$ dispensed into the system to vaporize oil, and the volume of oil available in the system to be vaporized, important controlling parameters. We have seen that the amount of oil produced is a function of the oil composition and pressure. But if we assume that the experiments are performed with the same oil, at the

same conditions of pressure and temperature of the field. And we also assume that we are using reservoir rock for the experiments, making the porosity similar, we can establish the following relation.

$$\frac{CO_2 vol_{field}}{\text{Bulk res } vol_{field}} = \frac{CO_2 vol_{lab}}{\text{Bulk res } vol_{lab}} \quad \text{.....} \quad 55$$

Using Eq. 55 we estimate the equivalent volume of $CO_2$ we need in the field to reach the recovery factors observed in the laboratory, for the volume of rock that is expected to be exploited with each fracture. Using this volume, and the data from Table 16, we estimate the number of cycles we need in the field to dispense the equivalent volume of $CO_2$.

$$\text{Number of cycles}_{field} = \frac{CO_2 vol_{field}}{\text{Frac } vol_{field}} \quad \text{.....} \quad 56$$

On the other side, the fracture-reservoir rock surface area exert control on soaking time. The more area there is available for mass transfer between the oil and the injected gas, the shorter the soaking time that is required. Based on this we then establish the following relation.

$$\frac{\text{Soaking time}_{field}}{\text{Soaking time}_{lab}} = \frac{\left[\frac{\text{Fracture PV}}{\text{Fracture surface A}}\right]_{field}}{\left[\frac{\text{Fracture PV}}{\text{Fracture surface A}}\right]_{lab}} \quad \text{.....} \quad 57$$

In Eq. 57 we have related the soaking time and the ratio of the volume of gas we can put inside the fracture to the surface area available for mass transfer to charge that gas with hydrocarbons. We use such relation to estimate the soaking time required in the field. Using Eq. 55 - 57, we calculate the number of cycles and the soaking time required for the fracture described in Table 16 using the results from test run 2.4 (Table 13) as a reference for the laboratory data. The results are presented in Table 17.

| | |
|---|---|
| Number of cycles | 87,512 |
| Soaking time (hr) | 0.6 |

Table 17 – Field cycles and soaking times

According to our estimations, we will need to execute 87,512 cycles in the field to supply an equivalent amount of gas to the one we supplied in our experiments. This is because in the field, the volume of gas that we can put inside the fracture is much smaller in relation to the volume of reservoir rock we are exploiting, than in the laboratory. On the other side, however, and because there is a significantly larger surface area available for mass transfer in the field, the soaking time required is much shorter. A 0.6 hours soaking time may not be a realistic value from a field perspective, considering the time it will take to inject the gas and produce it again. If we assume instead that we can do two cycles a day, it would take 120 years to reach ultimate recovery under $CO_2$.

These numbers for the field, however, cannot be taken literally for several reasons. In the first place, our equations assume the variables are linearly related, and we have no field data to back such assumption. Secondly, we are only accounting for the volume of the main fracture. Hydraulic fracturing results in the formation of a network of fractures that varies in complexity, and that also connects to the existing fractures in the reservoir. The existence of such a complex fracture network implies that our calculation underestimates the volume of $CO_2$ that can be put in the ground with each cycle, meaning that we need less huff-and-puff cycles. This reduces the time frame of the process to probably less than 100 years. Another way to decrease the time of the project is to reduce the fracture spacing, which should be weighed against the costs. This last option could imply also re-fracturing if the process is applied in wells that have already been completed and produced for several years under primary depletion.

There are probably additional factors we are not considering that will affect field performance. Some of them may arise only when the field implementation of gas injection for EOR in organic rich shales is

attempted. However, from our evaluation it seems like the chances of reaching field results that resemble the ones obtained in the laboratory are good enough to encourage a field trial.

## GAS UTILIZATION

An important parameter in gas injection is the gas utilization. Utilization refers to the volume of gas that is required to produce a barrel of incremental oil recovery. Gas utilization is relevant since it determines the volume of gas that is required to purchase and recycle, which controls an important share of the operating costs of gas injection processes. Gross utilization and net utilization are two common parameters referred to in gas flooding operations. Gross utilization is to the total volume of gas injected per incremental barrel of crude oil recovered, and net utilization is the volume of gas spent, unrecovered, or stored in the reservoir per incremental barrel of crude oil. Basically, the net utilization excludes the injected gas that is produced and can be separated and re-injected.

As we discussed in Chapter II and Chapter IV, organic rich shale reservoirs not only store gas in the pore space, but also in a sorbed state. The amount of gas that can be stored in a sorbed state depends on the amount and nature of the organic matter within the rock. This raises questions regarding gas utilization. Sorption is a function of pressure and gas can be sorbed and desorbed as pressure increases and decreases, however, these are not instantaneous processes and significant desorption may not occur fast enough to recover the trapped gas. Such gas may be accounted for as net utilization. If the volume of gas that is sorbed is large, net utilization could reach uneconomic levels.

We estimated net utilization from our experimental data. We consider three components in our calculation (Figure 70). The first component is the $CO_2$ that is left in the pore space previously occupied by the oil produced. The second component, is the $CO_2$ that sorbed by the organic matter in the portion of pore space also previously occupied by the oil produced. The third and last component, is the $CO_2$ that dissolved in the oil remaining in the reservoir. We believe this to be a high estimate for utilization because the production

mechanism, the slow-kinetics peripheral vaporizing gas drive, does not imply that oil is being displaced, but stripped out of its light and intermediate components. This means the first and second component in our calculation may be overestimated because the oil will not be displaced from the pore volume and therefore there should be no significant space available for $CO_2$ storage.

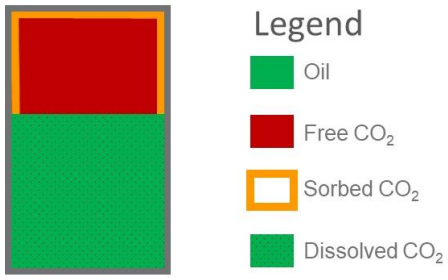

Figure 70 – Schematic representation of the three components of $CO_2$ storage. Free $CO_2$ in the porous space, sorbed $CO_2$ in and on the organic matter and dissolved $CO_2$ in the remaining oil.

The total $CO_2$ stored in the reservoir is given by;

$$CO_2\text{stored}=\left[\frac{\text{Free } CO_2+\text{Dissolved } CO_2+\text{Sorbed } CO_2}{28316.85}\right]\left[\frac{1}{1000}\right] \quad \ldots\ldots\ldots\ldots\ldots\ldots\ldots\ldots\ldots\ldots\ldots \quad 58$$

Assuming the volume of oil recovered corresponds to the fraction of the rock that is made available for gas storage;

$$\text{Free } CO_2=\left[N_p\ FVF_{oil}\right]\left[\frac{\rho_{CO_2\ res}}{\rho_{CO_2\ std}}\right] \quad \ldots\ldots\ldots\ldots\ldots\ldots\ldots\ldots\ldots\ldots\ldots\ldots\ldots\ldots\ldots\ldots\ldots\ldots\ldots\ldots\ldots\ldots... \quad 59$$

The sorbed $CO_2$;

$$\text{Sorbed } CO_2 = G_S \left[\frac{N_p FVF_{oil}}{por\ \rho_{rock\text{-}bulk}}\right]\left[\frac{28316.85}{907184.74}\right] \quad \text{.....} \quad 60$$

Where $G_s$ can be calculated based on the Langmuir (1917) isotherm;

$$G_S = G_{SL}\frac{p}{p+p_L} \quad \text{.....} \quad 61$$

The terms in Eq. 61 were addressed in Chapter IV.

Finally, the following expression can be used to estimate the dissolved $CO_2$

$$\text{Dissolved } CO_2 = \left[\frac{\%CO_2\left(IOIP_{core}\text{-}N_p\right) FVF_{oil}\ \rho_{oil\text{-}res}}{\rho_{CO_2\text{-}std}}\right] \quad \text{.....} \quad 62$$

And the utilization can be calculated;

$$\text{Net utilization} = \frac{CO_2 \text{stored}}{N_p} \quad \text{.....} \quad 63$$

The net utilization calculated with Eq. 63 would be an overall utilization for the process. In field applications in conventional reservoirs, utilization is a dynamic parameter that changes over time and that drives decisions such as the beginning of a water-alternating-gas (WAG) process. Once WAG is implemented, utilization is still used as one of the main surveillance variables that controls operational parameters such as the ratio of water to $CO_2$ injected, and the length of each water and $CO_2$ cycles. Table 18 shows some of the input variables in Eqs. 58 to 63, together with the volume of $CO_2$ that is stored in a free state in the pore volume, sorbed in the rock, and dissolved in the remaining oil.

| Test run | 1.1 | 2.2 | 2.4 |
|---|---|---|---|
| Sample | 1 | 5 | 8 |
| Test pressure (psig) | 2,500/3,500 | 2,100 | 3,100 |
| Test soaking time (hr) | 22 | 0 | 21 |
| Recovery factor (%) | 40 | 7.4 | 26.2 |
| FVFoil | 1.1 | 1.1 | 1.1 |
| Concentration of $CO_{2\ residual\ oil}$, (wt.%) | 0.25 | 0.25 | 0.25 |
| $CO_2$ sorption, $G_S$, (scf/ton) | 110.8 | 30.3 | 99.4 |
| Free $CO_2$ ($cm^3$, std) | 345.7 | 9.7 | 137.9 |
| Sorbed $CO_2$ ($cm^3$, std) | 53.7 | 0.53 | 16.7 |
| Dissolved $CO_2$ ($cm^3$, std) | 130.4 | 42.9 | 93.67 |
| Total stored $CO_2$ ($cm^3$, std) | 529.8 | 53.14 | 248.3 |
| Sorbed $CO_2$ (% of Total) | 10.1 | 1.0 | 6.7 |
| Net Utilization (Mscf/STB) | 3.91 | 9.95 | 4.81 |

Table 18 – Net utilization for test runs 1.1, 2.2 and 2.4. The $CO_2$ concentration in the residual oil and the $FVF_{oil}$ were assumed in this calculation.

The results in Table 18 were calculated for 1.1, 2.2, and 2.4, to contrast test runs with low and high recovery factor. All the input parameters in Eqs. 58 to 63 are available from our experimental results or can be calculated with EOSs, except for the oil formation volume factor ($FVF_{oil}$) and the concentration of $CO_2$ in the residual oil. We have assumed 1.1 for $FVF_{oil}$ because we used dead oil in our experimental work. For the $CO_2$ concentration in the residual oil we have made an assumption of 25%. Net utilization is close to four in the cases of high recovery factor, tests 1.1 and 2.4. For the test 2.2 the net utilization approaches ten.

Higher oil recovery is linked to lower utilization since the volume of produced oil appears in the denominator of Eq. 63. On the other side, a higher oil production leads to more pore volume left to store $CO_2$, both free and sorbed. Test run 1.1 is the one with the lowest utilization. Conversely, this test is also the experiment with the highest volume of $CO_2$ left in the reservoir. But, the high recovery factor of 40% implies that the $CO_2$ was efficiently utilized for crude oil extraction. Utilization is not about the amount of $CO_2$ employed, but the volume used to extract one barrel of oil. So, it is a measure of how efficiently the $CO_2$ is used. This test run was performed with sample 1, which is the one with the highest porosity among all our samples (Table 10). That is the reason why most of the $CO_2$ is stored in a free state in this experiment. This sample also has the highest $CO_2$ sorption capacity

Test run 2.2 has the lowest oil recovery and the largest utilization. Net utilization in this case is close to ten. In this experiment, we left inside the reservoir the lowest volume of $CO_2$ out of the three tests we are comparing in Table 18. However, the low oil recovery drove the utilization high, because the volume of $CO_2$ we left stored did not result in significant oil production, making $CO_2$ use inefficient. In this case, most of the $CO_2$ is stored dissolved in the remaining oil in the reservoir as residual oil saturation is high. Test run 2.4 had a significant recovery factor of 26.2%. This test also had a low net utilization of 4.81. Most of the $CO_2$ that was left in the formation in this case was in a free state and dissolved in the crude oil.

The utilization calculated here, even when over-estimated, may still be lower than the values observed in the field where out-of-zone injection is a common problem, mostly in the case of open hole completions. Also, $CO_2$ is lost to other patterns or to outside of the lease limits. The takeaway from this exercise is that the volume of $CO_2$ stored in the formation in a sorbed state does not significantly increase utilization. For the examples in Table 18 the maximum percentage of the total $CO_2$ stored that is in a sorbed state is roughly 10%, and it happens to be in the test with the highest recovery and the lowest utilization.

We are not making a significant effort to support the assumption of 25% of $CO_2$ content by weight in the residual oil. This is because we are mainly focusing in the $CO_2$ sorption, as this is what sets the organic rich shale reservoirs apart from the conventional ones, where $CO_2$ is also dissolved in the remaining oil during $CO_2$ flooding. However, all calculations were re-ran using 40% instead. The net utilizations for test runs 1.1, 2.2 and 2.4 were 4.49, 14.77 and 5.90 respectively, which are still low utilization values.

## SUMMARY

In this Chapter, we have examined our laboratory results from a field standpoint. In the laboratory, the ratio of the fracture pore volume to the reservoir pore volume is much higher than in the field, this implies that an equivalent volume of $CO_2$ to the one we dispensed in the laboratory in 4 cycles, would take approximately 80,000 cycles in the field. However, in the field, the ratio of the fracture pore volume to the fracture-reservoir

contact surface is much smaller, which means the soaking time will probably be much shorter. We estimated soaking time could be as short as less than one hour, but assumed six hours to be more realistic for field operations. This resulted in an overall timeframe for the process of around 120 years. However, if we consider the volume of the natural fractures, microfractures, and the complexity of the hydraulic fractures this could probably be reduced below 100 years. This number, however, is not to be taken literally, because of the poor theoretical basis of our calculations. But it is an encouraging indication that this process has a reasonable time frame that invites a field trial. Also, the large surface available for mass transfer between the reservoir matrix and the gas stored in the fracture could counterbalance the slow-kinetic aspect of the process resulting in higher oil recovery.

We also calculated utilization. We used an approach that considers the volume of oil produced is then available in the reservoir for $CO_2$ storage. This represents a conservative approach that probably results in an overestimation of the utilization. The reason for this is that oil is not really displaced in this process but stripped of its lighter components, meaning that there should not be significant changes in the pore volume occupied by oil inside the rock matrix. Even under these conditions, we obtain utilization values that should not represent any economic limitation for the process. Of course, it should be noted that utilization depends on the nature and amount of organic matter present in the shale, and therefore will be different for different rock samples.

# CHAPTER VIII

# CONCLUDING REMARKS

We presented the first throughout evaluation of gas injection in organic rich shale reservoirs. This work described the necessary stages for the assessment of enhanced oil recovery processes in organic rich shale, including details of sample cleaning and preparation, the measurement of rock and crude oil properties, the re-saturation of shale core plugs with crude oil, and a new concept for core-flooding that simulates injection through a hydraulic fracture. A configuration that represents better the reality of unconventional resources exploitation. In this chapter, we will highlight the major contributions of our investigation.

In Chapter III, we showed that direct gas injection through organic rich shale matrix is not possible in a reasonable time frame. That triggered the construction of equipment, and the development of an experimental protocol to resemble the injection through a hydraulic fracture. We accomplished this by surrounding an organic rich shale core with glass beads to recreate the proppant. This way, we could easily inject the gas through a high permeability medium that was in direct contact with a matrix of low permeability, closely mimicking field conditions. The development of this novel injection technique is our first significant contribution.

Using that procedure, we performed nine experiments injecting $CO_2$ in preserved organic rich shale cores from the Wolfcamp, the Eagle Ford, the Barnett, and the Bakken. Out of the nine experiments, only three of them recovered substantial volumes of crude oil. We estimated the recovery factor to range between 18 and 62% of the initial oil in the cores. This demonstrated that it is possible to use $CO_2$ to extract the naturally occurring oil in core plugs with extremely poor transport properties, where gas could not be injected directly. Also, by coupling the core-flooding equipment developed in house with a CT-scanner, we demonstrated that CT-scanning technology could track the changes in density resulting from the mass exchange between the $CO_2$ and the crude oil. Those are our second, and third contributions.

The results of the nine experiments in preserved sidewall cores revealed the necessity to know the initial oil in place within the core plugs. This was mainly for two reasons. The first one, is the great uncertainty in the recovery factor calculations caused by the use of preserved core samples of unknown initial oil saturation. The second reason were the unsuccessful tests. The volume of oil recovered in the successful experiments was substantial, considering the possible range for the pore volume of the samples. Also, most of the oil recovery happened in the first two days. Conversely, in the unsuccessful experiments, we did not recover any oil, or we recovered a volume below our measurement resolution of 0.01 $cm^3$. The extreme responses, complete success or complete failure, led us to suspect there was no oil contained in the samples we used for the unsuccessful experiments. The core plugs were obtained from different companies, and they did not provide any accompanying information to inspect which sidewall cores were taken in productive intervals and which ones were not. Thus, having samples with no oil saturation was not only possible, but it was likely. Nevertheless, the three successful experiments were enough to justify further research.

We devoted Chapter IV to gain knowledge of our organic rich shale and crude oil samples. In house, we cleaned and dried the core plugs, CT-imaged them, measure their pore volume with helium, their $CO_2$ sorption capacity, and we re-saturated them with crude oil. We described the equipment we built, the experimental protocols we used, and the data interpretation techniques. The development of a comprehensive procedure for core preparation, enabling the assessment of gas injection for EOR in organic rich shale is our fourth contribution.

After the cores were used for the EOR experiments, we outsourced mercury porosity, stress Swanson permeability to air, pore size distribution, TOC, and mineralogy. This complete set of experiments enabled us to provide an exceptional description of the cores used in this investigation, and to establish many relationships among properties. Some of those relationships, like the linear increase of porosity with silicates content, its linear decrease with carbonate content; and the increase of sorption capacity and porosity with TOC, reaffirmed previous findings from other authors. Yet others, like the linear decrease of porosity and sorption capacity with CT-number, are novel and meaningful, and we claim them as the fifth contribution

of our work. The CT-number of a core plug can be obtained in minutes, making these relationships an important tool for the estimation of porosity, sorption capacity, and TOC, in organic rich shale.

We present in Chapter V the results of nine core-flooding experiments of $CO_2$ injection through a hydraulic fracture in an organic rich shale crude oil reservoir. The difference of these experiments with the ones presented in Chapter III, is that in this case we used the core plugs that were re-saturated in the laboratory. Therefore, we can calculate accurate recovery factors because we know the initial oil volume in each sample. The runs were divided in two sets, the first set of experiments was performed with crude oil and core samples from well 1, whereas the second set employed oil and cores from well 2. The maximum recovery factors were 40% for set 1 and 26.15% for set 2; obtained in six days and 4.2 days, respectively. Moreover, the highest rate of recovery was observed during the first 24 hours. This is remarkably rapid, considering the poor transport properties of the samples, which required four to five months, on average, to be re-saturated with crude oil; even at the high pressure of 10,000 psig. These results demonstrated gas injection is an attractive technique that can achieve significant oil recovery from organic rich shale reservoirs in a realistic time frame. This was our sixth contribution.

Also in Chapter V, we studied the effect of pressure and soaking time; and concluded that recovery factor increases as either of these parameters increase. Rising the pressure by 1,000 psig, increased recovery factor in 44 to 338%, depending on soaking time and crude oil composition. Similarly, going from continuous flooding to huff-and-puff, with soaking time of 21 and 22 hours increased recovery factor from 78.1 to 464.2%, depending on operating pressure and crude oil composition. We also studied the influence of MMP on recovery and discovered a major departure from the conventional wisdom. Increasing pressure beyond the MMP continues to increase recovery factor in organic rich shale reservoirs. These results shed light on the field operation of gas injection with EOR purposes in organic rich shales, and they are our seventh contribution.

Chapter VI focused in expanding our understanding on the recovery mechanisms taking place. We accomplished that goal by analyzing oil composition, CT-scanning data, and the results of additional core-flooding experiments. The additional runs were performed using the same technique for the physical simulation of gas injection through a hydraulic fracture presented in Chapters III and V. However, we now study the effect of rock permeability by performing experiments in Berea sandstone with 100 md in absolute permeability, and the effect of gas composition by injecting nitrogen in re-saturated organic rich shale reservoir core plugs. We proposed the peripheral slow-kinetics vaporizing gas drive as the main recovery mechanism. The peripheral and the slow-kinetics features of this vaporizing gas drive differentiate it from the conventional vaporizing gas drive observed in conventional reservoir rocks, or slim tube experiments. We used ternary diagrams to explain those differences, which result in reductions in the efficiency of the recovery process.

The peripheral condition is imposed by the fact that we cannot inject directly through the core, but through a fracture. The relevance of this was demonstrated by the experiments performed in Berea sandstone, where even above MMP, recovery factor was always under 60%. This is because the development of miscibility at the displacement front due to a multiple contacts process is what enables the high recovery observed in conventional reservoirs. In our experiments, the mass exchange that triggers the miscible front is happening in the borderline of the sample, but it is not sweeping through it. Therefore, oil is not displaced, but vaporized. This means that MMP is not controlling the process. The volume of oil recovered now depends on the amount of oil that can be vaporized into the volume of gas in the fracture, at the given conditions of pressure and temperature. The higher the pressure, the higher the vaporization, and the recovery.

The second aspect of the novel recovery mechanism is it slow-kinetics. This was made evident by the examination of the CT-scanning data. In Berea sandstone, the injected gas affects uniformly the totality of the matrix, leading to a uniform oil composition within the core. In organic rich shale, this does not happen. We observed the existence of three regions of different compositions within the matrix even after six days after the injection was started. An external region where the density of the oil had decreased because $CO_2$

condensation outweighed the vaporization of hydrocarbon components. A central region with no change in density, where the vaporization of hydrocarbon components and the condensation of $CO_2$ are equivalent, and an internal region, where density had increased since the vaporization of the hydrocarbon components outweighed the condensation of $CO_2$. These regions are a consequence of the low transport properties of the organic rich shale, which impairs the mass transfer process. Therefore, the recovery in organic rich shale would be lower than the observed in high permeability media, because in the latter, the gas can vaporize all hydrocarbon components until it is saturated at the prevailing thermodynamic conditions, whereas in shale it cannot.

To maximize recovery from organic rich shale, we shall select a gas that can vaporize the maximum amount of hydrocarbons, inject it at the maximum possible pressure; and allow enough time for the mass exchange to take place. The importance of the gas selection was emphasized by our experiments with nitrogen. The lower potential of nitrogen to vaporize hydrocarbons is exacerbated by the peripheral and slow-kinetics features of the vaporizing gas drive, resulting in no hydrocarbon recovery from shale, even at 5,000 psig. This means that gases like nitrogen and methane are less adequate, and we prefer the use of carbon dioxide or ethane in organic rich shale. The understanding of the recovery mechanism taking place is our eighth contribution.

Chapter VII presents a comparison between laboratory and field conditions that recognizes the scaling problems intrinsic to laboratory experiments. In our case, the ratio of fracture to matrix volume is much higher than what is achievable in the field; this implies that more huff-and-puff cycles would be needed on the field to dispense an equivalent volume of $CO_2$ per volume of rock matrix. Conversely, the ratio of fracture-matrix surface area, to fracture volume, is much higher in the field than it is in the laboratory. This translates into a much bigger area available for mass transport, meaning that we should expect soaking time to be significantly shorter in the field. This can also counter balance the negative effects of the slow-kinetics, resulting in higher recovery. The presence of fractures and micro-fractures in the field that were not considered in our calculations make the number of required cycles shorter. We estimate the oil recovery

process by gas injection in organic rich shales could span several decades to reach ultimate recovery, but it will likely take less than a century. In this time, we could ultimately achieve recovery factors in the orders of what was observed in the laboratory. Additionally, we made utilization calculations. The capacity of the organic rich shale to adsorb $CO_2$ is of interest because a higher volume of $CO_2$ left in the reservoir translates into higher costs. Our results show that the sorbed $CO_2$ only accounts for 1 to 10% of the $CO_2$ left in the reservoir at the relevant pressure conditions, which is consistent with the results presented in Chapter IV. The comparison of the laboratory scale results with the field scale, and the estimations made for utilization, encourage the pursue of pilot projects for gas injection in organic rich shale reservoirs for EOR purposes, and they are our ninth and last contribution.

REFERENCES


Adel, Imad A. 2016. A reliable and rapid technique for the laboratory determination of the minimum miscibility pressure for $CO_2$–light crude oil systems using the slim tube method. Masters of Science Thesis, Texas A&M University, College Station, TX, USA.

Adel, Imad A, Francisco D Tovar, David S Schechter. 2016. Fast-slim tube: A reliable and rapid technique for the laboratory determination of MMP in $CO_2$–light crude oil systems. Proc., SPE Improved Oil Recovery Conference, Tulsa, Oklahoma, USA.

Adesida, Adelola G, Ibrahim Y Akkutlu, Daniel E Resasco et al. 2011. Characterization of Barnett shale kerogen pore size distribution using DFT analysis and grand canonical Monte Carlo simulations. Proc., SPE Annual Technical Conference and Exhibition, Denver, Colorado, USA.

Akkutlu, Ibrahim Y, Ebrahim Fathi. 2012. Multiscale gas transport in shales with local kerogen heterogeneities (in English). *SPE Journal* **17** (04): 1,002-1,011.

Ambrose, Raymond J, Robert C Hartman, Ibrahim Y Akkutlu. 2011. Multi-component sorbed phase considerations for shale gas-in-place calculations. Proc., SPE Production and Operations Symposium, Oklahoma City, Oklahoma, USA.

Ambrose, Raymond J, Robert C Hartman, Mery Diaz-Campos et al. 2012. Shale gas-in-place calculations Part I: New pore-scale considerations (in English). *SPE Journal* **17** (01): 219-229.

API 40, Recommended practices for core analysis. 1998. Washington, DC, USA: American Petroleum Institute.

Bai, Baojun, Malek Elgmati, Hao Zhang et al. 2013. Rock characterization of Fayetteville shale gas plays (in English). *Fuel* **105**: 645-652.

Balmaseda, J, E Reguera, A Gomez et al. 2003. On the microporous nature of transition metal nitroprussides (in English). *The Journal of Physical Chemistry B* **107** (41): 11360-11369.

Bohrer, M, S Fried, L Helms et al. 2008. State of North Dakota Bakken resource study project (in English). *North Dakota Department of Mineral Resources* **23**.

BP. 2016. BP Energy Outlook 2016. London, England, British Petroleum.

Bustin, R Marc, Amanda M Bustin, Albert Cui et al. 2008. Impact of shale properties on pore structure and storage characteristics. Proc., SPE Shale Gas Production Conference, Fort Worth, Texas, USA.

Chalmers, Gareth R, Robert M Bustin. 2007. The organic matter distribution and methane capacity of the Lower Cretaceous strata of Northeastern British Columbia, Canada (in English). *International Journal of Coal Geology* **70** (1): 223-239.

Chalmers, Gareth R, Robert M Bustin. 2008. Lower Cretaceous gas shales in northeastern British Columbia, Part I: geological controls on methane sorption capacity (in English). *Bulletin of Canadian petroleum geology* **56** (1): 1-21.

Chalmers, Gareth R, Robert M Bustin, Ian M Power. 2012. Characterization of gas shale pore systems by porosimetry, pycnometry, surface area, and field emission scanning electron

microscopy/transmission electron microscopy image analyses: Examples from the Barnett, Woodford, Haynesville, Marcellus, and Doig units (in English). *AAPG bulletin* **96** (6): 1099-1119.

Chalmers, Gareth R, Daniel J Ross, Robert M Bustin. 2012. Geological controls on matrix permeability of Devonian Gas Shales in the Horn River and Liard basins, northeastern British Columbia, Canada (in English). *International Journal of Coal Geology* **103**: 120-131.

Chareonsuppanimit, Pongtorn, Sayeed A Mohammad, Robert L Robinson Jr et al. 2012. High-pressure adsorption of gases on shales: Measurements and modeling (in English). *International Journal of Coal Geology* **95**: 34-46.

Charlaix, Elisabeth, Matteo Ciccotti. 2009. Capillary condensation in confined media (in English). *arXiv preprint arXiv:0910.4626*.

Civan, Faruk, Chandra S Rai, Carl H Sondergeld. 2011. Shale-gas permeability and diffusivity inferred by improved formulation of relevant retention and transport mechanisms (in English). *Transport in Porous Media* **86** (3): 925-944.

Clark, Aaron J. 2009. Determination of recovery factor in the bakken formation, mountrail county, ND. Proc., SPE Annual Technical Conference and Exhibition, New Orleans, Louisiana, USA.

Clarkson, Christopher R, N Solano, Robert M Bustin et al. 2013. Pore structure characterization of North American shale gas reservoirs using USANS/SANS, gas adsorption, and mercury intrusion (in English). *Fuel* **103**: 606-616.

Comisky, Joseph T, Michael Santiago, Bruce McCollom et al. Sample size effects on the application of mercury injection capillary pressure for determining the storage capacity of tight gas and oil shales. *Calgary, Alberta, Canada*: Society of Petroleum Engineers.

Cui, Xiaojun, Amanda M Bustin, Robert M Bustin. 2009. Measurements of gas permeability and diffusivity of tight reservoir rocks: different approaches and their applications (in English). *Geofluids* **9** (3): 208-223.

Curtis, Mark E, Raymond J Ambrose, Carl H Sondergeld. 2010. Structural characterization of gas shales on the micro-and nano-scales. Proc., Canadian Unconventional Resources and International Petroleum Conference, Calgary, Alberta, Canada.

Dean, E, D Stark. 1920. A convenient method for the determination of water in petroleum and other organic emulsions (in English). *Journal of Industrial & Engineering Chemistry* **12** (5): 486-490.

Dechongkit, Piya, Manika Prasad. 2011. Recovery factor and reserves estimation in the Bakken petroleum system (analysis of the Antelope Sanish and Parshall fields). Proc., Canadian Unconventional Resources Conference, Calgary, Alberta, Canada.

Delaihdem, Dieudonne K. 2013. Decline curve analysis and enhanced shale oil recovery based on Eagle Ford Shale data. Masters of Science Thesis, University of Alaska Fairbanks, Fairbannks, Alaska, USA.

Diaz-Perez, A, I Cortés-Monroy, J Roegiers. 2007. The role of water/clay interaction in the shale characterization (in English). *Journal of Petroleum Science and Engineering* **58** (1): 83-98.

Dong, Cuiyu, Todd Hoffman. 2013. Modeling gas injection into shale oil reservoirs in the sanish field, North Dakota. Proc., Unconventional Resources Technology Conference, Denver, Colorado, USA, 1824-1833.

Dubinin, M. 1960. The potential theory of adsorption of gases and vapors for adsorbents with energetically nonuniform surfaces (in English). *Chemical Reviews* **60** (2): 235-241.

EIA. 2013. Technically recoverable shale oil and shale gas resources: An assessment of 137 shale formations in 41 countries outside the United States, US Department of Energy, Washington, DC, USA.

EIA. 2016. International energy outlook 2016 with projections to 2040, U.S. Department of Energy, Washington DC, USA.

Gamadi, T, J Sheng, M Soliman et al. 2014. An experimental study of cyclic $CO_2$ injection to improve shale oil recovery. Proc., SPE Improved Oil Recovery Symposium, Tulsa, Oklahoma, USA.

Gaswirth, S. 2017. Assessment of continuous oil resources in the Wolfcamp shale of the Midland Basin, Permian Basin Province, Texas, 2016., U.S. Geological Survey, Reston, Virginia, USA.

Grabar, Katherine C, Kenneth R Brown, Christine D Keating et al. 1997. Nanoscale characterization of gold colloid monolayers: a comparison of four techniques (in English). *Analytical chemistry* **69** (3): 471-477.

Handwerger, David A, Dean M Willberg, Markus Pagels et al. 2012. Reconciling retort versus Dean Stark measurements on tight shales. Proc., SPE Annual Technical Conference and Exhibition, San Antonio, Texas, USA.

Heller, Robert, Mark Zoback. 2014. Adsorption of methane and carbon dioxide on gas shale and pure mineral samples (in English). *Journal of Unconventional Oil and Gas Resources* **8**: 14-24.

Hoffman, Todd. 2012. Comparison of various gases for enhanced recovery from shale oil reservoirs. Proc., SPE Improved Oil Recovery Symposium, Tulsa, Oklahoma, USA.

Hoffman, Todd, Shehbaz Shoaib. 2014. $CO_2$ flooding to increase recovery for unconventional liquids-rich reservoirs (in English). *Journal of Energy Resources Technology* **136** (2): 022801.

Hughes, J 2013. Energy: A reality check on the shale revolution (in English). *Nature* **494** (7437): 307-308.

Humayun, Raashina, David L Tomasko. 2000. High-resolution adsorption isotherms of supercritical carbon dioxide on activated carbon (in English). *AIChE Journal* **46** (10): 2065-2075.

IEA. 2016. World energy outlook 2016, International Energy Agency, Paris, France.

Jin, Lu, James Sorensen, Steven Hawthorne et al. 2016. Improving oil recovery by use of carbon dioxide in the Bakken unconventional system: A laboratory investigation (in English). *SPE Reservoir Evaluation & Engineering*.

Jin, Zhehui, Abbas Firoozabadi. 2016. Thermodynamic modeling of phase behavior in shale media (in English). *SPE Journal* **21** (01): 190 - 207. SPE-176015-PA.

Kale, Sagar V, Chandra S Rai, Carl H Sondergeld. 2010. Petrophysical characterization of Barnett shale. Proc., SPE Unconventional Gas Conference, Pittsburgh, Pennsylvania, USA.

Kang, Seung M, Ebrahim Fathi, Ray J Ambrose et al. 2011. Carbon dioxide storage capacity of organic-rich shales (in English). *Spe Journal* **16** (4): 842-855. SPE-134583-PA.

Krooss, B, S Schloemer, R Ehrlich. 1998. Experimental investigation of molecular transport and fluid flow in unfaulted and faulted pelitic rocks (in English). *Geological Society, London, Special Publications* **147** (1): 135-146.

Kuuskraa, Vello, Matt Wallace. 2014. $CO_2$-EOR set for growth as new $CO_2$ supplies emerge (in English). *Oil & Gas Journal* **112** (5): 92-92.

Lake, Larry W. 2010. *Enhanced oil recovery*. Richardson, TX, USA, Society of Petroleum Engineers (Reprint).

Langmuir, Irving. 1917. The constitution and fundamental properties of solids and liquids (in English). *Journal of the Franklin Institute* **183** (1): 102-105.

Liu, G, J Sorensen, J Braunberger et al. 2014. $CO_2$-based enhanced oil recovery from unconventional reservoirs: A case study of the Bakken formation. Proc., SPE Unconventional Resources Conference, Woodlands, Texas, USA.

Loucks, Robert G, Robert M Reed, Stephen C Ruppel et al. 2009. Morphology, genesis, and distribution of nanometer-scale pores in siliceous mudstones of the Mississippian Barnett Shale (in English). *Journal of sedimentary research* **79** (12): 848-861.

Luffel, D, F Guidry. 1992. New core analysis methods for measuring reservoir rock properties of Devonian shale (in English). *Journal of Petroleum Technology* **44** (11): 1,184-1,190.

Maugeri, Leonardo. 2013. *The shale oil boom: a US phenomenon*. Cambridge, Massachusetts, USA: Harvard Kennedy School (Reprint).

Mavor, M, L Owen, T Pratt. 1990. Measurement and evaluation of coal sorption isotherm data. Proc., SPE Annual Technical Conference and Exhibition, New Orleans, Louisiana, USA.

Ming, Li, Gu Anzhong, Lu Xuesheng et al. 2003. Determination of the adsorbate density from supercritical gas adsorption equilibrium data (in English). *Carbon* **41** (3): 585-588.

Mohammad, Sayeed, James Fitzgerald, Robert L Robinson Jr et al. 2009. Experimental uncertainties in volumetric methods for measuring equilibrium adsorption (in English). *Energy & Fuels* **23** (5): 2810-2820.

Mohanty, Kishore, Cheng Chen, Matthew Balhoff. 2013. Effect of reservoir heterogeneity on improved shale oil recovery by $CO_2$ huff-n-puff. Proc., SPE Unconventional Resources Conference, The Woodlands, TX, USA.

Mullen, Jacky. 2010. Petrophysical characterization of the Eagle Ford Shale in south Texas. Proc., Canadian Unconventional Resources and International Petroleum Conference, Calgary, Alberta, Canada.

Nuttall, Brandon C, Cortland F Eble, James A Drahovzal et al. 2005. Analysis of Devonian black shales in Kentucky for potential carbon dioxide sequestration and enhanced natural gas production (in English). *Kentucky Geological Survey Report DE-FC26-02NT41442*.

Rangarajan, Bharath, Carl T Lira, Ramkumar Subramanian. 1995. Simplified local density model for adsorption over large pressure ranges (in English). *AIChE Journal* **41** (4): 838-845.

Roque-Malherbe, R, O Uwakweh, C Lozano et al. 2011. Structural effects and interactions of carbon dioxide molecules adsorbed on Ni, Zn, and Cd nitroprussides (in English). *The Journal of Physical Chemistry C* **115** (31): 15555-15569.

Ross, Daniel J, Robert M Bustin. 2009. The importance of shale composition and pore structure upon gas storage potential of shale gas reservoirs (in English). *Marine and Petroleum Geology* **26** (6): 916-927.

Santos, Jose M, Ibrahim Y Akkutlu. 2013. Laboratory measurement of sorption isotherm under confining stress with pore-volume effects (in English). *SPE Journal* **18** (05): 924-931.

Sasaki, Hirokazu, Takeyoshi Matsuda, Takeharu Kato et al. 2004. Specimen preparation for high-resolution transmission electron microscopy using focused ion beam and Ar ion milling (in English). *Journal of electron microscopy* **53** (5): 497-500.

Schmoker, James W. 1979. Determination of organic content of Appalachian Devonian shales from formation-density logs: Geologic notes (in English). *AAPG Bulletin* **63** (9): 1504-1509.

Shoaib, Shehbaz, Todd Hoffman. 2009. $CO_2$ flooding the Elm Coulee field. Proc., SPE Rocky Mountain Petroleum Technology Conference, Denver, Colorado, USA.

Sigal, Richard F, Ibrahim Y Akkutlu, Seung M Kang et al. 2013. The Laboratory Measurement of the Gas-Storage Capacity of Organic Shales (in English). *Petrophysics* **54** (3): 224-235.

Skinner, James T., Francisco D. Tovar, David S. Schechter. 2015. Computed tomography for petrophysical characterization of highly heterogeneous reservoir rock. Proc., SPE Latin American and Caribbean Petroleum Engineering Conference, Quito, Ecuador.

Sondergeld, Carl H, Raymond J Ambrose, Chandra S Rai et al. 2010. Micro-structural studies of gas shales. Proc., SPE Unconventional Gas Conference, Pittsburgh, Pennsylvania, USA.

Sondergeld, Carl H, Kent E Newsham, Joseph T Comisky et al. 2010. Petrophysical considerations in evaluating and producing shale gas resources. Proc., SPE Unconventional Gas Conference, Pittsburgh, Pennsylvania, USA.

Sorensen, James A, Steven B Hawthorne, John A Harju et al. 2013. Hydrocarbon mobilization mechanisms from upper middle and lower Bakken reservoir rocks exposed to $CO_2$. Proc., SPE Unconventional Resources Conference Canada, Calgary, Alberta, Canada.

Stalkup, Fred I., Jr. 1983. Status of miscible displacement (in English). *Journal of Petroleum Technology* **35** (04).

Stimpson, Brian C, Maria A Barrufet. 2016. Effects of confined space on production from tight reservoirs. Proc., SPE Annual Technical Conference and Exhibition, Dubai, UAE.

Sudibandriyo, Mahmud, Zhejun Pan, James E Fitzgerald et al. 2003. Adsorption of methane, nitrogen, carbon dioxide, and their binary mixtures on dry activated carbon at 318.2 K and pressures up to 13.6 MPa (in English). *Langmuir* **19** (13): 5323-5331.

Sun, Jianlei, Amy Zou, David Schechter. 2016. Experimental and numerical studies of $CO_2$ EOR in unconventional liquid reservoirs with complex fracture networks. Proc., SPE Improved Oil Recovery Conference, Tulsa, Oklahoma, USA.

Teklu, Tadesse W, Najeeb Alharthy, Hossein Kazemi et al. 2014. Phase behavior and minimum miscibility pressure in nanopores (in English). *SPE Reservoir Evaluation & Engineering* **17** (03): 396-403. SPE-168865-PA.

Thommes, Matthias, Katsumi Kaneko, Alexander V Neimark et al. 2015. Physisorption of gases, with special reference to the evaluation of surface area and pore size distribution (IUPAC Technical Report) (in English). *Pure and Applied Chemistry* **87** (9-10): 1051-1069.

Tovar, Francisco D. 2014. Experimental investigation on the use of water soluble polyacrylamides as thickeners during $CO_2$ WAG EOR. Masters of Science Thesis, Texas A&M University, College Station, Texas, USA.

Tovar, Francisco D, Maria A Barrufet, David S Schechter. 2015. Experimental investigation of polymer assisted WAG for mobility control in the highly heterogeneous north burbank unit in oklahoma, using anthropogenic $CO_2$. Proc., SPE Latin American and Caribbean Petroleum Engineering Conference, Quito, Ecuador.

Tovar, Francisco Deomar, Oyvind Eide, Arne Graue et al. 2014. Experimental investigation of enhanced recovery in unconventional liquid reservoirs using $CO_2$: A look ahead to the future of unconventional EOR. Proc., SPE Unconventional Resources Conference, The Woodlands, Texas, USA.

Vermesse, J, D Vidal, P Malbrunot. 1996. Gas adsorption on zeolites at high pressure (in English). *Langmuir* **12** (17): 4190-4196.

Weniger, Philipp, Wolfgang Kalkreuth, Andreas Busch et al. 2010. High-pressure methane and carbon dioxide sorption on coal and shale samples from the Paraná Basin, Brazil (in English). *International Journal of Coal Geology* **84** (3): 190-205.

Yu, Wei, Emad W Al-Shalabi, Kamy Sepehrnoori. 2014. A sensitivity study of potential $CO_2$ injection for enhanced gas recovery in Barnett shale reservoirs. Proc., SPE Unconventional Resources Conference, Woodlands, Texas, USA.

Yu, Wei, Hamid Lashgari, Kamy Sepehrnoori. 2014. Simulation study of $CO_2$ huff-n-puff process in Bakken tight oil reservoirs. Proc., SPE Western North American and Rocky Mountain Joint Meeting, Denver, Colorado, USA.

Ziel, R, A Haus, A Tulke. 2008. Quantification of the pore size distribution (porosity profiles) in microfiltration membranes by SEM, TEM and computer image analysis (in English). *Journal of membrane science* **323** (2): 241-246.